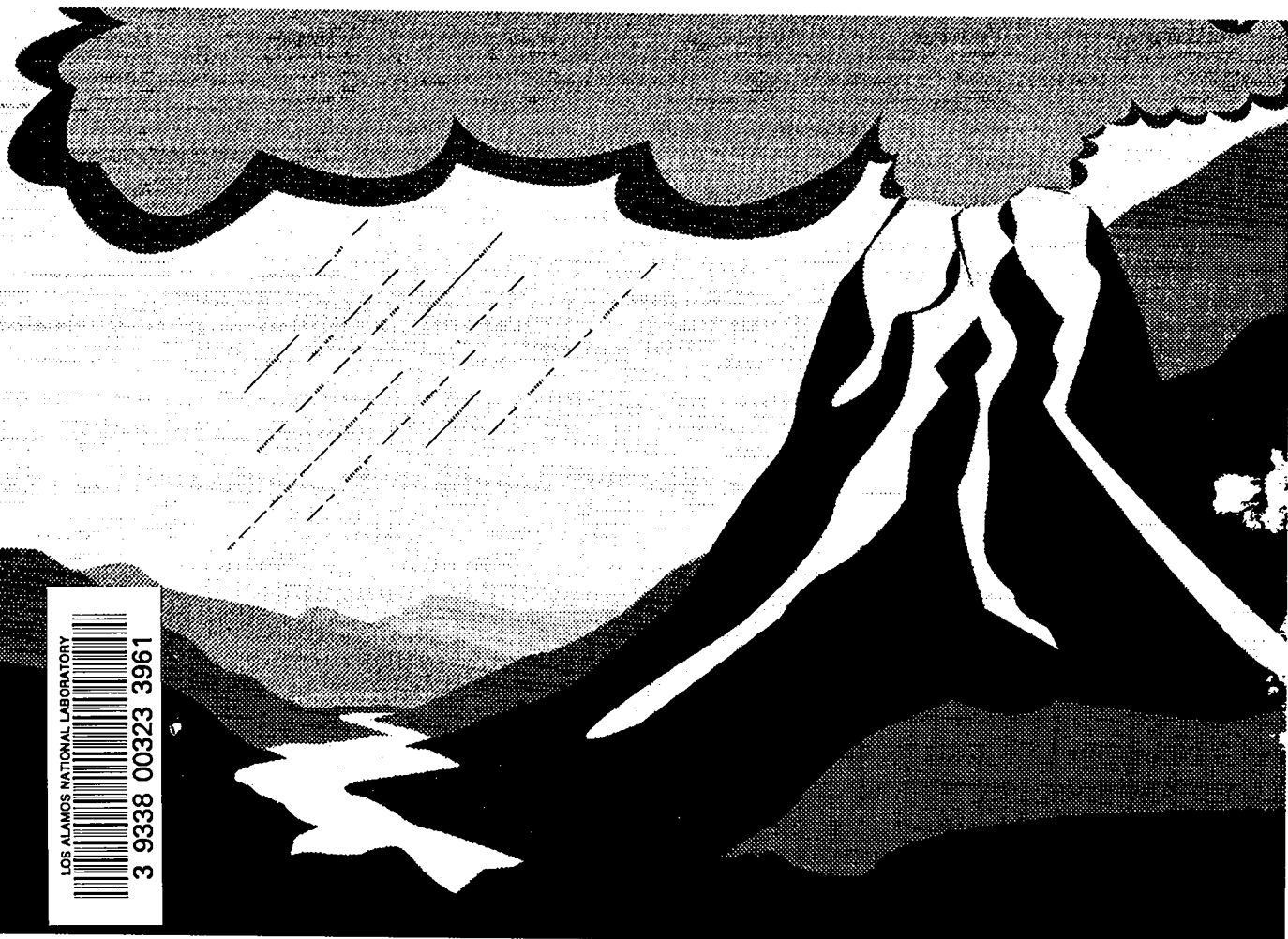


LA-11441-T  
Thesis

e.3

**REPRODUCTION  
COPY**

*Field and Theoretical Aspects of  
Explosive Volcanic Transport Processes*



LOS ALAMOS NATIONAL LABORATORY  
3 9338 00323 3961

**Los Alamos**

Los Alamos National Laboratory is operated by the University of California for the United States Department of Energy under contract W-7405-ENG-36.

*This thesis was accepted by the Department of Geological Sciences, University of California, Santa Barbara, California, in partial fulfillment of the requirements for the degree of Doctor of Philosophy in Geology. It is the independent work of the author and has not been edited by the IS-11 Writing and Editing staff.*

*This work was supported by the Los Alamos National Laboratory and the National Science Foundation.*

*An Affirmative Action/Equal Opportunity Employer*

*This report was prepared as an account of work sponsored by an agency of the United States Government. Neither the United States Government nor any agency thereof, nor any of their employees, makes any warranty, express or implied, or assumes any legal liability or responsibility for the accuracy, completeness, or usefulness of any information, apparatus, product, or process disclosed, or represents that its use would not infringe privately owned rights. Reference herein to any specific commercial product, process, or service by trade name, trademark, manufacturer, or otherwise, does not necessarily constitute or imply its endorsement, recommendation, or favoring by the United States Government or any agency thereof. The views and opinions of authors expressed herein do not necessarily state or reflect those of the United States Government or any agency thereof.*

*Field and Theoretical Aspects of  
Explosive Volcanic Transport Processes*

*Gregory Allen Valentine*



## TABLE OF CONTENTS

INTRODUCTION . . . . .	1
CHAPTER 1: LAYER 1 DEPOSITS OF THE PEACH SPRINGS TUFF IGNIMBRITE . . . . .	5
Introduction . . . . .	5
Geologic Setting . . . . .	8
Facies and Terminology . . . . .	12
Stratigraphy . . . . .	18
Kingman Area . . . . .	18
Layer 1a . . . . .	19
Fine ash layer (FA1) . . . . .	29
Layer 1b . . . . .	29
Layer 1c . . . . .	34
Regional Variations . . . . .	35
Laboratory Data . . . . .	38
Granulometry . . . . .	38
Component Analysis . . . . .	39
Interpretation: Initial Phases of the Peach Springs Tuff Eruption . . . . .	48
Lower Fine Ash Layer (FA0) . . . . .	53
Layer 1a . . . . .	53
Fine Ash Layer (FA1) . . . . .	59
Layer 1b . . . . .	60
Layer 1c . . . . .	61
Lateral Extent of the Pyroclastic Surges . . . . .	61
Discussion . . . . .	62
CHAPTER 2: STRATIFIED FLOW IN PYROCLASTIC SURGES . . . . .	65
Introduction . . . . .	65
Stratified Flow Parameters . . . . .	67
Conditions for Turbulent Transport . . . . .	79
Surge Bed Forms . . . . .	87
Wavelength Variations . . . . .	88
Migration Direction . . . . .	90
Pyroclastic Surge Facies . . . . .	91
Proximal to Distal Facies Changes . . . . .	91
Facies Variations Due to Topography . . . . .	93
The Low-Aspect-Ratio Ignimbrite Problem . . . . .	99
Summary . . . . .	106
Appendix 2A: Definition of Notation for Chapter 2 . . . . .	109

CHAPTER 3: NUMERICAL MODELS OF PLINIAN ERUPTION COLUMNS AND PYROCLASTIC FLOWS . . . .	112
Introduction . . . . .	112
Previous Modeling . . . . .	113
Theoretical Approach . . . . .	116
Governing Equations . . . . .	116
Dimensionless Parameters . . . . .	127
General Features of the Numerical Experiments . . . . .	131
Eruption Column Collapse . . . . .	140
Evolution of Modeled Eruption Columns . . . . .	143
Non-collapsing (plinian) . . . . .	143
Collapsing column (fountain) . . . . .	152
Implications for Pyroclastic-Flow Transport and Ignimbrite Facies . . . . .	155
Pyroclastic Flows . . . . .	155
Pyroclastic flows produced by brief discharge . . . . .	162
Pyroclastic flows produced by coarse- grained eruption . . . . .	163
Pyroclastic flows produced by low $T_m$ - $R_m$ - $K_p$ eruption . . . . .	164
Ground Surge . . . . .	165
Ash Cloud . . . . .	167
Proximal Co-Ignimbrite Breccias and the Deflation Zone . . . . .	169
Previous work . . . . .	169
Modeling Approach and Results . . . . .	171
Conclusions . . . . .	177
Appendix 3A: Definition of Notation for Chapter 3 . . . . .	183
Appendix 3B: Material Properties and Values of Physical Parameters Used in Numerical Experiments. . . . .	186
Appendix 3C: Exit Conditions of Model Eruptions . . . . .	187
Appendix 3D: Numerical Formulation and Accuracy . . . . .	189
Appendix 3E: Scaling of Viscous Forces and Heat Conduction . . . . .	197
Scaling of Viscous Forces . . . . .	197
Scaling of Intraphase Heat Conduction . . . . .	199
REFERENCES . . . . .	201

## LIST OF FIGURES AND TABLES

	Page
Figure 1-1: Regional distribution of Peach Springs Tuff and possible correlative units.	7
Figure 1-2: Map of Peach Springs Tuff in the study area.	11
Figure 1-3: Generalized volcanic stratigraphy at Kingman.	15
Figure 1-4: Exposure of open-valley facies Peach Springs Tuff near Kingman.	17
Figure 1-5: Stratigraphic columns of Peach Springs Tuff open-valley and edge facies.	21
Figure 1-6: Stratigraphy of layer 1 and correlation within study area.	23
Figure 1-7: Photographs of layer 1 deposits near Kingman.	
(a) Layers 1a and 1b	25
(b) layer 1b	26
(c) layer 1c	27
Figure 1-8: Wavy bed form types found in layer 1 deposits.	31
Figure 1-9: Undulation bed forms in layer 1a.	33
Figure 1-10: Granulometric data from layer 1 near Kingman.	41
Figure 1-11: Scanning electron microphotographs of shards.	45
Figure 1-12: Component analysis of layer 1 near Kingman.	47
Figure 1-13: Relative importance of magmatic and hydroclastic fragmentation in layer 1.	51
Figure 1-14: Interpreted events at beginning of Peach Springs Tuff eruption.	55
Figure 2-1: Particle concentration profiles in turbulent pyroclastic surges.	73
Figure 2-2: Brunt-Vaisala frequency profiles in pyroclastic surges.	77
Figure 2-3: Particle Rouse numbers for the Mount St. Helens blast.	85

Figure 2-4:	Blocking in a density-stratified pyroclastic surge.	97
Figure 2-5:	Turbulent transport model for deposition of low-aspect-ratio ignimbrites.	105
Figure 3-1:	Computational domain for numerical models.	121
Figure 3-2:	Terminology for features of Plinian eruptions.	135
Figure 3-3:	Numerical eruption producing a Plinian eruption column.	137
Figure 3-4:	Numerical eruption producing a pyroclastic fountain and pyroclastic flows.	139
Figure 3-5:	Criteria for collapse of eruption columns based upon three dimensionless parameters.	145
Figure 3-6:	Detailed structure of overpressured eruption column (same model as Figure 3-3).	151
Figure 3-7:	Particle concentration - velocity plot for brief discharge eruption.	157
Figure 3-8:	Particle concentration - velocity plot for coarse-grained eruption.	159
Figure 3-9:	Particle concentration - velocity plot for low energy eruption.	161
Figure 3-10:	Particle concentration - velocity plot for eruptions with varying particle size.	175
Figure 3-11:	Particle concentration along the ground as a function of distance from vent for eruptions with varying particle size.	179
<hr/>		
Table 1-1:	Regional characteristics of layer 1 of the Peach Springs Tuff.	36
Table 2-1:	Characteristics of the Taupo ignimbrite and Mount St. Helens blast deposit.	101

## ACKNOWLEDGEMENTS

Several people have provided insight and help along the way during my graduate studies and preparation of this dissertation, but two researchers have had the most profound influence on my work. The first of these is Richard V. Fisher, my main advisor, and the other is Kenneth H. Wohletz. The influence of these two goes deeper than the usual "mechanical" aspects of the student-tutor relationship. Their most important influence has been by setting the example of confidence in one's contributions and of open-mindedness. These aspects play a role in research at least as important as methodology and ability to communicate; they take away much of the anxiety of scientific competition and allow the researcher to truly enjoy science. Professor Fisher has been supporting of all of my work, both intellectually and in terms of funding. Indeed, if he had not pushed for my acceptance into the graduate program at Santa Barbara I probably would not have been able to pursue this degree. He supported me in questioning many of the current dogmas of pyroclastic geology, and by having me as a field assistant allowed me to learn about descriptive geology from one of the foremost field volcanologists. Dr. Wohletz provided me with the environment and tools to do some of the most sophisticated volcanological modeling that has been carried out to date. He assisted me with interpretation of my field work, and has kept my perspective in line during some of the inevitable tense times that

graduate students experience as impending graduation also seems like impending unemployment. Both of these men have treated me as an equal and have allowed me to go where I please with my work, and, more importantly, have become my good friends.

I also thank Fraser Goff and Steve Self for introducing me to volcanology when I was still an undergraduate. Steve McLean and Scott Hickman of the Mechanical Engineering Department at Santa Barbara are responsible for teaching fluid dynamics to me. Cathy Busby-Spera and Frank Spera have provided suggestions along the way and carefully read this dissertation. Grant Heiken helped with scanning electron microscope work and gave assistance with preparing Chapter 1. Rod Whitaker and Frank Harlow have provided insight into physical problems of high-speed fluid dynamics. Susan Kieffer and Brad Sturtevant visited my field area and provided insight into fluid-dynamical interpretations of pyroclastic flows. David Buesch has been a good friend and co-worker on the studies of the Peach Springs Tuff that are partially reported in Chapter 1. We shared so many ideas in the field that, as he once said, it is difficult to remember from whom the ideas originated.

My wife Mary and (during the last year) son Jeremy have been sources of loving support throughout my graduate work. Without Mary my perspective on the relationship between life and career would have been horribly out of balance. During times of faltering confidence she has kept me on my feet. Unwinding at the end of a

hard day's work has been greatly facilitated by chasing Jeremy around the house (my knees will always have carpet burns).

The work presented in Chapter 1 was partially, and that in Chapter 3 was completely, supported by Institutional Supported Research and Development funds at Los Alamos National Laboratory (Department of Energy). Additional sources of funding for the work in Chapters 1 and 2 were provided by the Geological Society of America, Sigma Xi, UCSB Graduate Division, UCSB Academic Senate (Patent Funds), the UCSB Department of Geological Sciences, and National Science Foundation grant EAR-16582 to Fisher. Chapters 1 and 3 comprise Los Alamos Unclassified Reports LA-UR 88-1047 and LA-UR 88-1314, respectively.



## VITA

- 18 April 1962 -- Born -- Alva, Oklahoma
- 1980-1984 -- New Mexico Institute of Mining and Technology  
B.S. - Geological Engineering and Geology
- 1984 -- Graduate Research Assistant  
Geology/Geochemistry Group, Los Alamos National Laboratory
- 1984-1986 -- Research Assistant  
Department of Geological Sciences, University of  
California, Santa Barbara
- 1986-1987 -- Teaching Assistant  
Department of Geological Sciences, University of  
California, Santa Barbara
- 1987-1988 -- Staff Research Assistant  
Geoanalysis Group, Los Alamos National Laboratory

## PUBLICATIONS

- Valentine GA (1987) Stratified flow in pyroclastic surges. Bulletin of Volcanology 49: 616-630
- Valentine GA, Fisher RV (1986) Origin of layer 1 deposits in ignimbrites. Geology 14: 146-148
- Buesch DC, Valentine GA (1986) Peach Springs Tuff and volcanic stratigraphy of the southern Cerbat Mountains, Kingman, Arizona. In Nielson JE, Glazner AL (eds) Cenozoic stratigraphy, structure, and mineralization in the Mojave Desert. Geological Society of America Guidebook and Volume, Los Angeles, pp 7-14
- Bower NW, Valentine GA (1986) Critical comparison of sample preparation methods for major and trace element determinations using x-ray fluorescence. X-Ray Spectrometry 15: 73-78
- Valentine G (1983) Procedures for analysis of silicate rocks and minerals at Los Alamos National Laboratory by x-ray fluorescence. Los Alamos National Laboratory Report LA-9663-MS

## PRESENTATIONS

- Valentine GA (1988) Physics of caldera eruptions. Invited seminar, Department of Earth Sciences, New Mexico State University, Las Cruces, New Mexico

- Valentine GA (1988) Bed forms in layer 1 of the Peach Springs Tuff: Transport processes during the blast phase of the eruption. Spring Geological Society of American Meeting, Cordilleran Section, Las Vegas
- Valentine GA, Wohletz KH (1988) Significance of exit pressure in plinian eruptions. EOS Transactions, American Geophysical Union 68: 1535, San Francisco
- Valentine GA (1987) Layer 1 deposits in the Peach Springs Tuff, Arizona: Initial stages of a large-volume eruption. International Union of Geodesy and Geophysics, Vancouver, Canada
- Fisher RV, Valentine GA (1987) Fractal deposits from turbulent transport: Mount St. Helens. International Union of Geodesy and Geophysics, Vancouver, Canada
- Valentine GA (1986) Turbulent boundary layers in pyroclastic flows: A possible origin of layer 1 in ignimbrites. International Volcanological Congress, New Zealand
- Fisher RV, Valentine GA (1986) Pyroclastic flows, surges, and fluidization. International Volcanological Congress, New Zealand.
- Buesch DC, Valentine GA (1986) Peach Springs Tuff and volcanic stratigraphy of the southern Cerbat Mountains, Kingman, Arizona. Spring Geological Society of America Meeting, Cordilleran Section, Los Angeles

#### FIELDS OF STUDY

Major Field: Volcanology

Studies in Theoretical Volcanology:

Numerical Models of Plinian Eruption Columns and Pyroclastic Flows. Dr. Kenneth H. Wohletz.

Stratified Flow In Pyroclastic Surges.

Studies in Application of Nonlinear Dynamics:

Fractal Facies and Sedimentology of the Mount St. Helens Blast. Prof. Richard V. Fisher.

Studies in Field Volcanology:

Volcanology of the Peach Springs Tuff, Arizona. Prof. Richard V. Fisher and David C. Buesch.

Volcanology of the 18 May 1980 Mount St. Helens Blast. Prof. Richard V. Fisher.

## ABSTRACT

### Field and Theoretical Aspects of Explosive Volcanic Transport Processes

by

Gregory Allen Valentine

Three separate but related studies, each utilizing a different approach to study aspects of explosive volcanism, are presented. Chapter 1 presents results of a study of deposits at the base of the large-volume Peach Springs Tuff ignimbrite (referred to as layer 1). The layer 1 deposits are interpreted to record initial blasting and pyroclastic surge events at the beginning of the eruption. Changes in bedding structures with increasing flow distance are related to the decreasing sediment load of the surges and possibly to shocks in the surges. Component analyses support a hydrovolcanic origin for some of the blasting and subsequent pyroclastic surges. The stratigraphic sequence indicates that powerful hydrovolcanic blasting rapidly widened the vent, thus bypassing a Plinian phase and causing rapid evolution to a pyroclastic-flow producing column collapse (fountaining).

In Chapter 2 stratified flow theory is applied to pyroclastic surges. Particle transport is assumed to be by turbulent suspension. The discussion centers on the Rouse, Froude, and Richardson numbers, and the Brunt-Vaisala frequency. Commonly observed variations in bed-form wavelength and surge facies are

functions of variations of the above parameters with distance from vent. Blocking in stratified flows plays a role in producing thick, massive deposits in topographic lows.

Chapter 3 presents results of simulations Plinian eruption columns based upon numerical solution of the time-dependent, two-phase, compressible Navier-Stokes equations. Consideration of dimensionless groups defines conditions leading to column collapse. Collapsing fountains form pyroclastic flows that consist of low-concentration fronts, relatively thick heads, vortex development along the top surfaces, and rising clouds of buoyant ash. The presence of coarse-grained proximal deposits primarily reflects tephra sorting within the eruption column before collapse. Modeling indicates that flow within a few kilometers of a vent will be at its highest particle concentration relative to other parts of the flow field.

Field and Theoretical Aspects of Explosive Volcanic  
Transport Processes

by

Gregory Allen Valentine

INTRODUCTION

Recent years have witnessed rapid advances in our knowledge of transport processes associated with explosive volcanic eruptions. The advantages of combining field and experimental (both laboratory and numerical) approaches have been widely recognized. Deposits of explosive eruptions represent the end product of large-scale, natural "experiments" with poorly constrained initial and boundary conditions. When studying a deposit, the goal is to constrain the initial and boundary conditions in terms of the known outcome (the deposit). On the other hand, numerical and laboratory experiments have very precisely known initial and boundary conditions, allowing interpretation of transport phenomena in terms of the known conditions. By studying both approaches simultaneously, using insights gained from each approach to improve the physical foundation of the other, it is hoped that an eventual common ground will be reached and that a physically rigorous understanding of explosive eruptions, rooted in observations of natural systems, can be attained.

There are many perspectives that make the study of explosive volcanism worthwhile, and it is appropriate to briefly mention these. The first perspective is that of magma transport theory. Explosive eruptions mark the final stage of transport processes that probably begin within the earth's mantle. These processes then affect the crust and result in accumulation of magma reservoirs at relatively shallow depths. Magmas within reservoirs undergo complex dynamical processes during their residence within the crust, and the geologic record preserves these processes in the form of cooled plutonic bodies and as rapid sampling events from eruptions. The significance of petrologic and geochemical variations in pyroclastic deposits for interpretation of magmatic processes has received much attention. Full interpretation of these variations will depend upon our understanding of the fluid dynamics of eruption and deposition of magma as well as subsurface processes. This is one of the goals of this thesis, although the surface has only begun to be scratched.

A second perspective is that of basic fluid dynamics. Explosive eruptions fall into a very complex class of fluid flows. The flows are often turbulent. They are compressible and can range from far subsonic to supersonic. The flows are multiphase, with several gas and solid species in varying concentrations and varying states (e.g., water can be present as a gas and as a liquid). Because of the multiphase nature of the flows, they are affected by density stratification. Finally, the flows can have an extreme range of rheological behaviors. The study of these eruptions

promises to advance the knowledge of complex fluid dynamics in important ways.

Three other important aspects of explosive eruptions include: (1) their role in the coupling between the solid earth and the atmosphere, (2) their association with geothermal and mineral resources, (3) volcanic hazards evaluation.

This thesis reports upon three independent but related studies that pertain to explosive volcanic transport processes. Chapter 1 describes field studies on the Peach Springs Tuff ignimbrite in western Arizona that have been carried out in conjunction with related studies by David C. Buesch (U.C. Santa Barbara). The field study centers upon the distribution, stratigraphy, and origin of pyroclastic surge deposits at the base of the ignimbrite, and naturally raises some questions about the transport and deposition of pyroclastic surges. Chapter 2 addresses many of these questions in light of stratified flow theory and turbulent transport. While the questions were initially raised during the Peach Springs Tuff study, the results of Chapter 2 are applicable to pyroclastic surges in general.

One aspect that was recognized early in the Peach Springs Tuff study is the applicability of blast phenomena for understanding the beginning phases of an eruption. It is thought that initial blasting and unsteady flow eventually gives way to steady flow that can produce a high-standing eruption column (leading to a fallout deposit) or a collapsing eruption column (leading to pyroclastic

flows). Although the Peach Springs Tuff appears to record the initial blasting phase of the eruption and a sustained period of pyroclastic flow, it displays no evidence of ever having gone through a fallout-producing phase. This raised the question: What determines the large-scale behavior of an eruption during steady discharge? Chapter 3 addresses this broad question from the standpoint of numerical experiments, and also deals with pyroclastic flow facies.

Each chapter stands alone, but it is best to consider the chapters together as a step toward the goal of having a "unified" picture of explosive volcanic processes. Appendices are given at the ends of Chapters 2 and 3, instead of together at the end of the thesis, so that each chapter can be read separately.

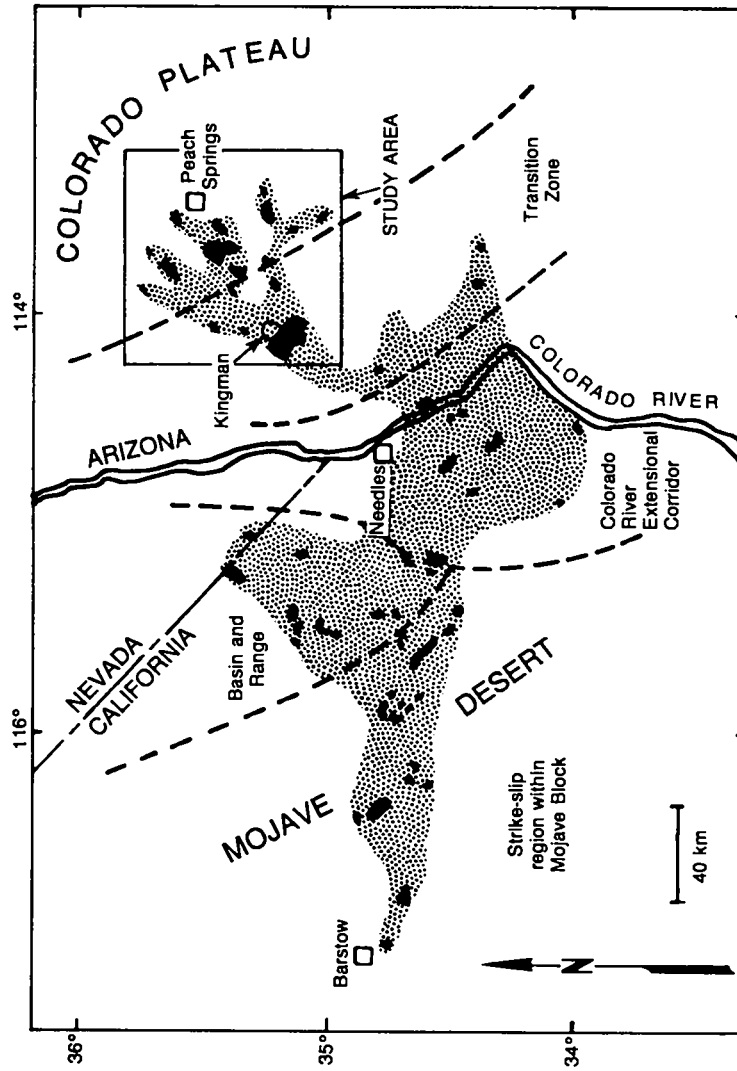
## CHAPTER 1: LAYER 1 DEPOSITS OF THE PEACH SPRINGS TUFF IGNIMBRITE

### INTRODUCTION

This chapter focuses upon vertical and lateral variations of the basal deposits of the Miocene Peach Springs Tuff, a large-volume, rhyolitic, welded ignimbrite that crops out in western Arizona and southeastern California, USA (Figure 1-1). The purpose is to provide a physical framework for theoretical studies (Chapters 2, 3) and to understand how a large-volume ( $\geq 100 \text{ km}^3$ , Smith 1979) ignimbrite eruption evolves from initiation to sustained pyroclastic-flow forming discharge.

The Peach Springs Tuff (PST) was originally described by Young (1966) and Young and Brennan (1974), who mapped PST on the western margin of the Colorado Plateau in Arizona and correlated it with outcrops to the west in the Kingman area (Figure 1-1). Recent work in the Mojave Desert by Glazner et al. (1986) indicates that ignimbrite deposits in isolated mountain ranges as far west as Barstow, California, may correlate with Peach Springs Tuff described by Young and Brennan (1974). The areal distribution shown in Figure 1-1 was proposed by Glazner et al. (1986) on the basis of similarity of petrographic characteristics, stratigraphic position, mineral phase chemistry, and paleomagnetic pole directions. Additional correlation work based upon heavy mineral suites by Gusa et al. (1987) supports the areal distribution shown in Figure 1-1. Radiometric age dates of possible PST correlative rocks are

Figure 1-1: Regional distribution of Peach Springs Tuff and possible correlative units (modified from Glazner et al. 1986). Present-day exposures are shown by the solid pattern, minimum original extent (assuming all exposures are Peach Springs Tuff) is shown with stippled pattern. Dashed lines are tectonic province boundaries, compiled from Dokka (1983, 1986), Howard and John (1987), and Young and Brennan (1974). The present study area has been focused on in order to develop a type section and to constrain facies patterns, since this is the area where PST was originally described and where correlation is not a problem.



problematic and the scatter in ages (16-20 Ma) is not currently understood. The most likely age is about 18 million years (Glazner et al. 1986). The volume of the ignimbrite is poorly constrained but must have been several hundreds of cubic kilometers (Glazner et al. 1986). A source for the tuff has not yet been determined, and it is probably at least partially masked by post-eruption tectonism and sedimentation.

My research has been carried out in concert with other efforts directed at studying the source location problem and testing previous regional correlations. Although uncertainties in the source location and age of the tuff limit a full understanding of the eruption, its excellent exposure from top to bottom over large distances provides an excellent opportunity to study large-volume ignimbrite processes.

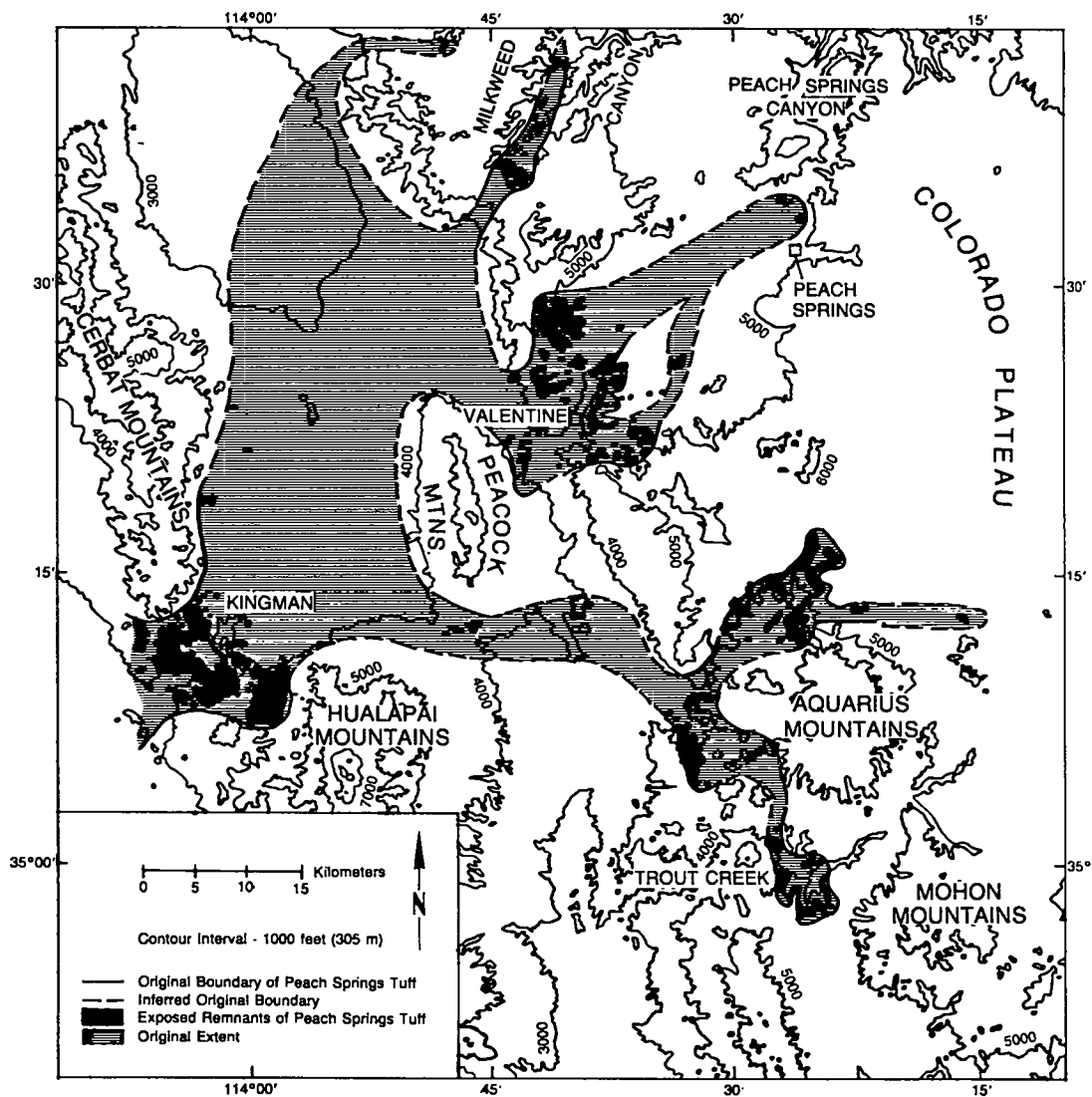
#### GEOLOGIC SETTING

The Peach Springs Tuff and its proposed correlative exposures extend from southeastern California into northwestern Arizona, covering an area of about 35,000 km<sup>2</sup> and overlapping several tectonic environments (Figure 1-1). The eastern part of the PST extent is on the tectonically stable Colorado Plateau. The western margin of the Colorado Plateau is bounded by a zone of normal faulting called the Transition Zone (Young and Brennan 1974). To the west of the Transition Zone, rocks become highly faulted and rotated within the Colorado River Extensional Corridor (Howard and

John 1987). They are only slightly tilted in the southern end of the Basin and Range Province. Farthest west, in the Mojave Desert, the PST occurs in a dominantly strike-slip region (Dokka 1983, 1986). I limit discussion here to deposits in the Transition Zone and the Colorado Plateau, where structural complications and correlation problems are minimal, and exposure is most continuous.

Within the study area (Figures 1-1 and 1-2) flow direction indicators, welding variations, and thickness distribution indicate an overall flow direction from west to east, as was also suggested by Young and Brennan (1974). The original extent of the ignimbrite in the study area (Figure 1-2) indicates that the pyroclastic surges and flows of the Peach Springs Tuff moved through a large paleovalley between the Cerbat and Hualapai Mountains (hereafter referred to as the Kingman paleovalley), then fanned out over a gently east-sloping terrain characterized by broad valleys of low relief (Young and Brennan, 1974). The valley-filling nature of the ignimbrite is clearly shown in Figure 1-2, with each "finger" of ignimbrite representing a paleovalley. While most of the mountain ranges shown in Figure 1-2 appear to have been present at eruption time, the large amount of relief at the margin of the Colorado Plateau was absent. The original extent within the study region covered an area of about 1800 km<sup>2</sup> with a minimum volume of 40 km<sup>3</sup>, of which the layer 1 deposits comprise about one percent. The Kingman area, in the western part of the study area, contains the thickest and most proximal exposures of the study area. The

Figure 1-2: Detailed map of Peach Springs Tuff and minimum original extent in the study area using U.S. Geological Survey 1:200,000 topographic sheets as base maps. Distribution is compiled from Young (1966), Goff et al. (1983), and my own work. Overall flow direction was from west to east. The most proximal part of the study area (near Kingman) is at least 30 km from the unknown source of the ignimbrite.



stratigraphic succession used in this report was developed in the Kingman outcrop area, which will be used for reference.

At the time of the Peach Springs Tuff eruption, the paleovalleys were typically bounded by granitic and metamorphic basement highs and, locally, Cenozoic volcanic rocks filled the valleys. The Kingman paleovalley floor contained hills of granitic basement rocks, along with basaltic cinder cones and lava flows. These were covered by a section of silicic fallout tuffs from a distant unknown source, an ignimbrite, and horizons of epiclastic sandstone and soil interbedded with reworked tephra. The Peach Springs Tuff lies on top of all these, and is separated from the older tuffs by a 1-2 m thick soil horizon. Volcanic stratigraphy of the Kingman paleovalley is shown in Figure 1-3.

Although the exact source vent for the PST has not been located, the nearest possible source is 30 km west of Kingman in the Black Mountains (Young and Brennan 1974), where a possible caldera has been identified (Thorson 1971). Work in progress suggests that another possible source area is about 90 km west of Kingman. However, because neither of these has yet been confirmed, I use 30 km west of Kingman as the most conservative estimate of distance from vent.

#### FACIES AND TERMINOLOGY

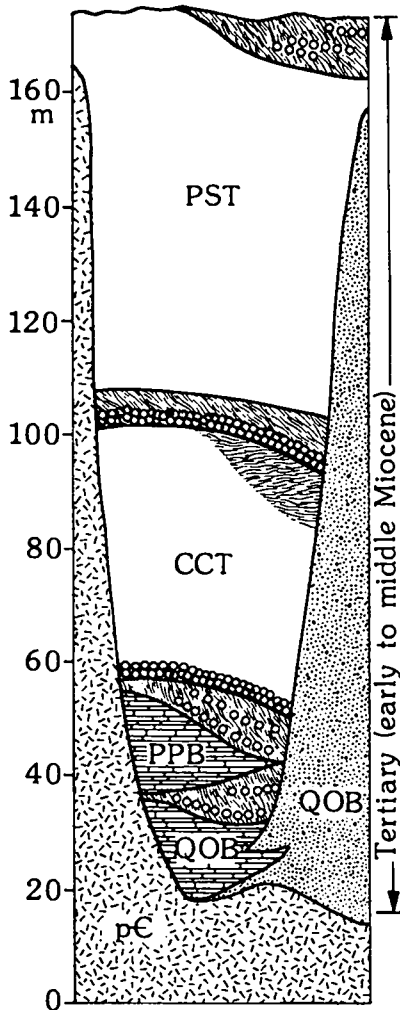
The Peach Springs Tuff ignimbrite is stratigraphically divided into layers 1 and 2, following the nomenclatural scheme of Sparks et

al. (1973). A typical outcrop displaying the two main layers is shown in Figure 1-4. Most of the layer 1 deposits represent a series of pyroclastic surges that immediately preceded the main layer 2-producing pyroclastic flow. Layer 2 appears to be a single pyroclastic-flow unit (Sparks et al. 1973) up to 90 m thick in the Kingman area that forms a simple cooling unit (Smith 1960). It thins gradually eastward in the study area to 5-10 m thickness at the distal eastern margins.

Lateral variations in layers 1 and 2 of the ignimbrite are divided into two facies types similar to those recognized by Freundt and Schmincke (1986). The first type of variation is termed "regional," and refers to changes due to proximal-to-distal flow processes. The second type is termed "local" variation, and refers to changes due to topography. Local variations are superimposed upon regional variations. Local variations are further subdivided into "open-valley" and "edge" facies. Open-valley facies occurs where the ignimbrite was deposited in broad, relatively smooth-bottomed valleys, and is the dominant facies type both areally and volumetrically. Edge facies occurs where the tuff thins against topographic highs on the order of 100 m and at valley edges.

Layers 1 and 2 both display significant differences between open-valley and edge facies locations (Figure 1-5). In this chapter only open-valley layer 1 deposits are discussed because they seem to represent separate eruptive phases from layer 2. Locally exposed relicts of open-valley layer 1 at edge facies locations suggest that

Figure 1-3: Generalized stratigraphy of volcanic rocks in the Kingman, Arizona, area (modified from Buesch and Valentine 1986). For detailed stratigraphic column of Peach Springs Tuff see Figure 1-5.



Interbedded epiclastic tuffaceous sandstone and fallout tuff. Two possible ignimbrites.

PST-Peach Springs Tuff. Light grey to mauve colored densely welded ignimbrite containing sanidine, quartz, and plagioclase as major phenocrysts. Ranges in thickness from 8m along paleovalley margins and over paleotopographic highs to 90m in axial portions of paleovalleys. Locally forms two cliff-forming units.

Pumiceous fallout tuff overlain by epiclastic volcanic sandstone.

CCT-Cook Canyon Tuff. Grey, sintered to partially welded ignimbrite containing plagioclase and biotite as major phenocrysts and mixed mafic/silicic pumice fragments. Everywhere underlain by pumiceous fallout tuff, locally top is reworked to epiclastic sandstone.

PPB-Pyroxene-plagioclase basalt lava flows.

Locally interbedded epiclastic volcanic sandstone and pumiceous fallout tuff.

QOB-Quartz-bearing olivine basalt forming lava flows up to 6m thick and cinder cones up to 150m high. Locally contains basement xenoliths.

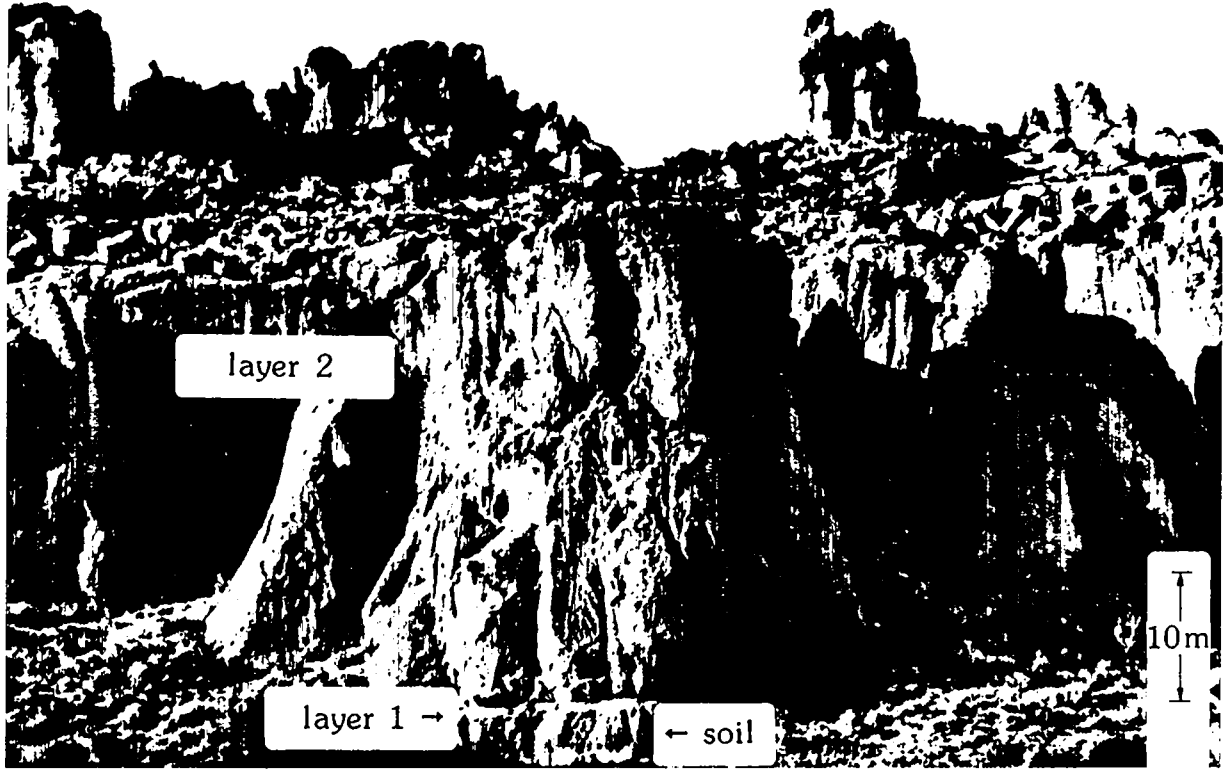
pC-Precambrian basement rocks consisting of quartz monzonite, locally porphyritic and locally foliated, with leuco- and melanocratic gneiss. Forms >150m paleorelief topography.

□ Ignimbrite  
 Silicic fallout tuff  
 Epiclastic sandstone

 Lava flows  
 Scoria/cinder-cone deposits  
 Basement rocks

Figure 1-4: Exposure of open-valley-facies PST in the Kingman area.

Layer 1 deposits form a white layer near the base of the outcrop, and are overlain by relatively massive layer 2 deposits.



open-valley layer 1 deposits originally mantled the landscape, at least within the large paleovalleys. However, the subsequent pyroclastic flow was highly erosive at edge locations and in most cases completely removed the previous layer 1 deposits, replacing them with edge facies layer 1 deposits. Edge facies layer 1 deposits are very similar to ground layer deposits of the Taupo ignimbrite described by Walker et al. (1981a) (Figure 1-5) and are interpreted to have formed from processes at the head of the pyroclastic flow (Wilson and Walker 1982) or within the main body of the pyroclastic flow (Freundt and Schmincke 1985; Valentine and Fisher 1986), reflecting changes in pyroclastic flow behavior due to topography.

No precursor Plinian fallout deposits have been found at the base of the Peach Springs Tuff, either in the present study area or in the Mojave Desert region. It is possible that this is due to lack of proximal exposures, but the absence of Plinian fallout over such a wide area leads me to believe that a sustained, high-standing eruption column did not play a significant role in the eruption.

## STRATIGRAPHY

### Kingman Area

Generalized stratigraphy of layer 1 deposits (open-valley facies) in the Kingman area is illustrated in the left-hand stratigraphic column in Figure 1-6 and photographically in Figure

1-7. Layer 1 is subdivided into three layers, 1a, 1b, and 1c, each of which is physically distinct.

Layer 1a

Layer 1a near Kingman is 40-80 cm thick, most commonly close to 60 cm, and is laterally continuous. It is composed mainly of pumiceous material, giving it an overall white color. In most places, the lower half of layer 1a (herein referred to as 1a<sub>1</sub>) consists of coarse ash to fine lapilli (Figure 1-10a) in very-thin parallel beds (all bed-thickness nomenclature follows Ingram 1954), each bed being 1-3 cm thick. The internal structure of very-thin beds in 1a<sub>1</sub> are of three basic types: normally graded, normally graded with internal laminae, and symmetrically (reverse to normal) graded. The basal contact of layer 1a<sub>1</sub> is typically planar, and displays evidence of being slightly erosive (e.g., chips of underlying paleosol within lowermost very-thin beds). Bedding is commonly parallel to the substrate in the lowest few very-thin beds, with small undulations becoming progressively amplified upward in the section, both in wavelength and amplitude. Some cross bedding occurs within the undulations, but in the Kingman area the beds are more commonly parallel. In bed forms that do display cross bedding, both upstream and downstream migration of crests occur. Undulations within the continuous beds are produced by subtle upward-repeating pinching or swelling and typically have rounded crests. These features are here referred to as "undulation bed forms," and are shown diagrammatically in Figure 1-8 along with typical cross bedded

Figure 1-5: Stratigraphic columns of Peach Springs Tuff in the Kingman area for open-valley and edge facies. Features shown for layer 2 are those due to cooling and weathering effects. Sedimentological details of the lower 2 m of the sequence are shown for both facies types. Open-valley layer 1 deposits are bedded and cross bedded and consist of coarse ash to small lapilli; they are the focus of this report. Layer 1e (edge facies) occurs only in a few locations. It is a laterally discontinuous, massive bed of mixed lithic (derived from the substrate) and pumice lapilli that is very similar to ground layer deposits described by Walker et al. (1981a).

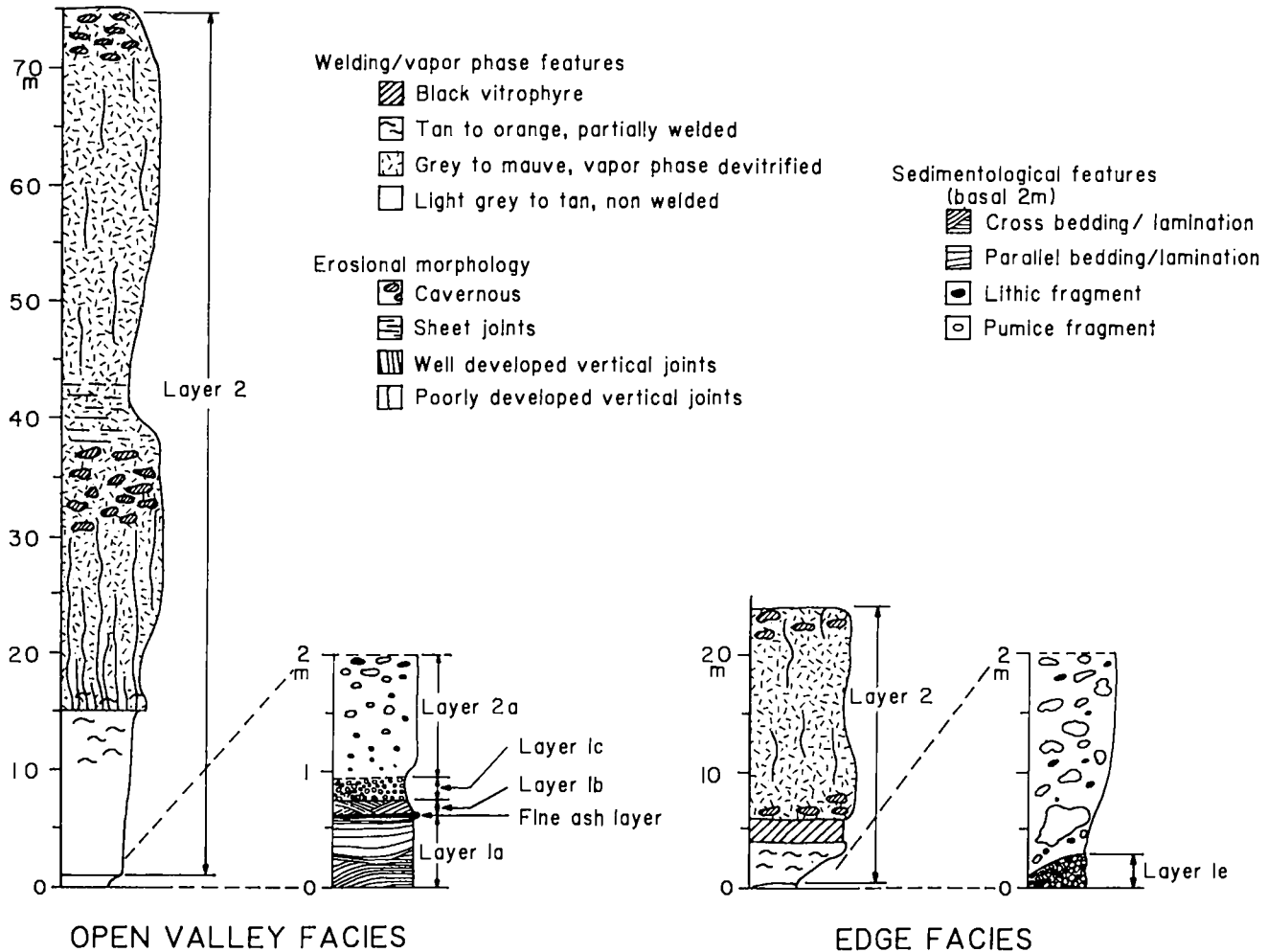


Figure 1-6: Stratigraphy of open-valley layer 1 deposits and regional correlation within study area. Locations of various stratigraphic columns can be found in Figure 1-2. Minimum distance from source is indicated for each column.

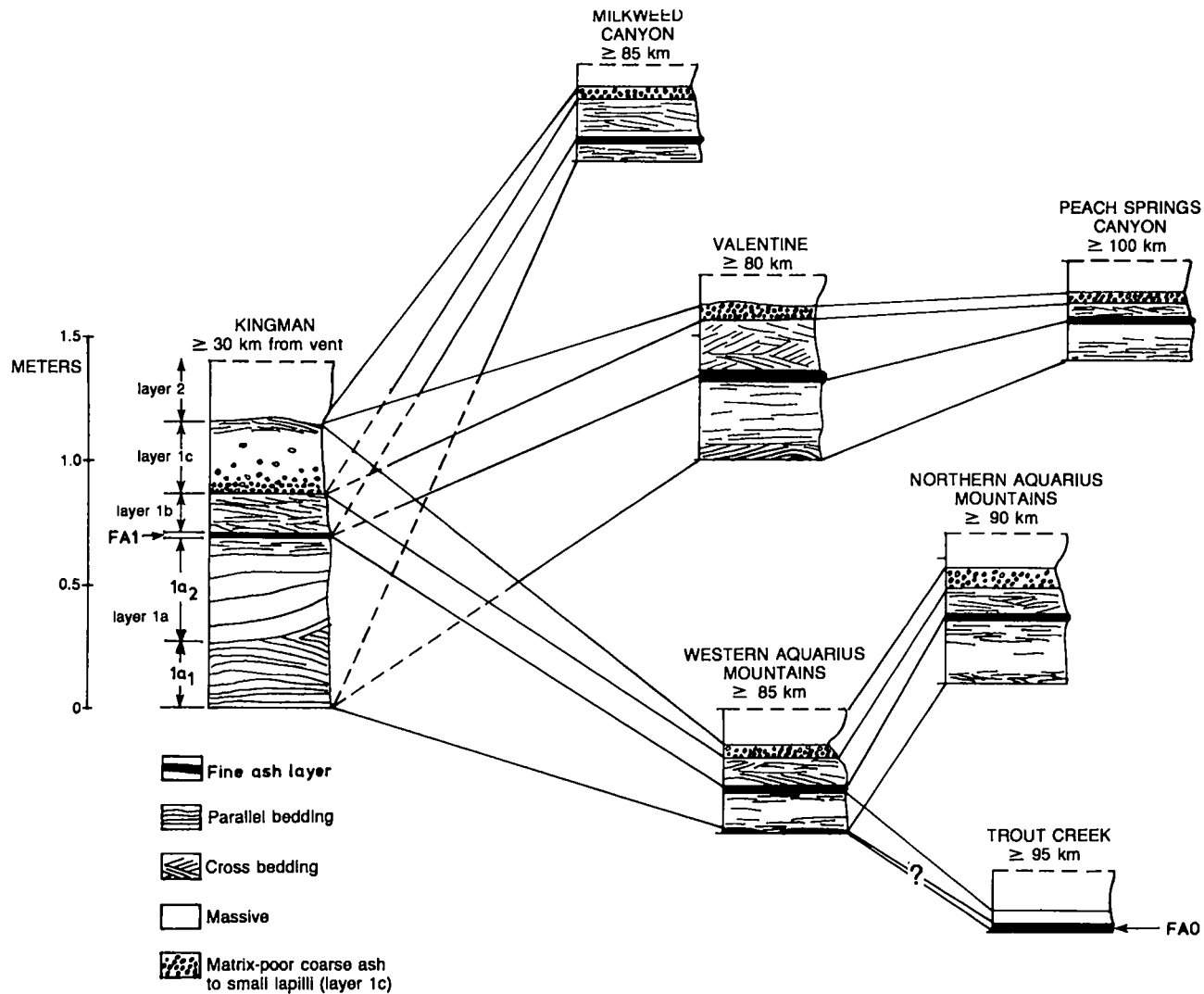


Figure 1-7: Photographs of exposures of layer 1 deposits in the Kingman area. (a) Layers 1a and 1b, separated by the fine ash layer (white layer just below bottom of measuring tape). Layer 1a is mainly planar-bedded here, and its upper half is coarser both in grain size and bedding than the lower half. Note flame structures in the fine ash layer on the left side of the photograph. Layer 1b is only a few centimeters thick in this exposure, and is represented by the laminated material immediately above the fine ash layer. Layer 1c is absent here, so that 1b is overlain by the inversely graded base of layer 2. (b) Detail of layer 1b. (c) Layer 1c with massive, coarser-grained base and fine-grained, bedded top.







features referred to as dunes and ripples, depending upon dimensions. Examples of undulation bed forms in the Peach Springs Tuff are shown in Figure 1-9. Unlike "sinusoidal ripple lamination" (Jopling and Walker 1968) these undulations are commonly isolated, or adjacent to other undulations with quite different dimensions. Wavelengths of these features are typically 0.5-2.0 m.

The top half of layer 1a (1a<sub>2</sub>) is coarser, with a higher concentration of lapilli compared to 1a<sub>1</sub> (Figure 1-10a). Bedding is thicker than in 1a<sub>1</sub>, ranging from 4-8 cm in thickness (thin beds of Ingram 1954). These thin beds are generally massive, but some are reversely graded within their lower 1 cm. The transition from very-thin bedding in 1a<sub>1</sub> to thin bedding in 1a<sub>2</sub> is commonly marked by an erosional surface, with the upper thin beds cutting into the lower very-thin beds. This erosional surface does not seem to represent a time break in deposition, due to a lack of associated fallout or locally reworked deposits. This transition is also characterized by coarsening of the deposit. In some instances, the undulation bed forms that were progressively amplified upward in 1a<sub>1</sub> continue to be amplified in 1a<sub>2</sub>. In other cases, bed forms within 1a<sub>2</sub> bear no obvious relationship to those in 1a<sub>1</sub>. The uppermost part of layer 1a<sub>2</sub> is characterized by 5-8 cm thick normally graded bed containing internal laminae and cross-laminae at its top.

Maximum lithic (ML) and pumice (MP) diameters in layer 1a range from 1.6-0.3 cm and 3.8-0.7 cm, respectively; at all layer 1a exposures MP and ML are found in the upper part of the layer (1a<sub>2</sub>).

Larger values of ML and MP tend to occur in the western part of the Kingman area. Two anomalously large values of ML (5.6 and 2.7 cm) on the leeward sides of a pre-existing cinder cone and a granitic basement high were measured, the fragments in these cases being locally derived from the associated topographic high. There is a gap in exposure between Kingman and the Colorado Plateau of about 30 km (Figure 1-2). To the east of this gap in exposure, layer 1a is mainly coarse ash and thus is too fine-grained for ML and MP measurements. Isopleths of maximum clast diameter were not constructed due to lack of continuous lateral exposure, but it is clear that the layer 1a deposits become finer grained eastward.

#### Fine Ash Layer (FA1)

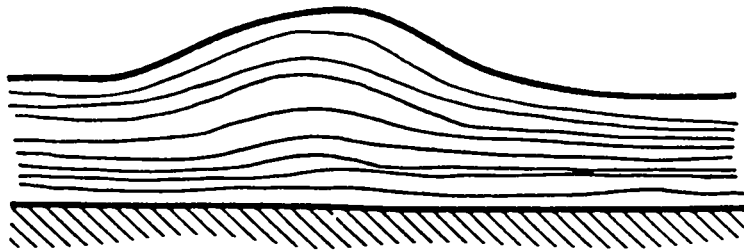
Layer 1a is capped by a 1-2 cm thick layer of white fine ash (FA1) which forms a key horizon for regional correlation of stratigraphy. In the Kingman area the upper few millimeters of this fine ash layer contain dispersed coarse-ash sized crystals and lithic fragments. In many places FA1 forms flame structures a few centimeters in height (Figure 1-7a). These flame structures may bend in many directions at a given outcrop and seem to represent deformation due to loading by the later-erupted, layer 2-producing pyroclastic flow. Layer 1b, directly above the fine ash layer, is both cross-cut and deformed by the flames.

#### Layer 1b

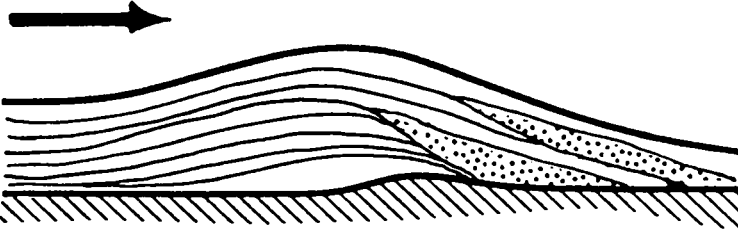
Layer 1b overlies layer 1a and the fine ash layer (Figures 1-6 and 1-7b). It is a laterally discontinuous layer up to 15 cm thick,

Figure 1-8: Wavy bed form types common in layer 1 of the Peach Springs Tuff. (a) Undulation bed form, (b) low-angle dune/ripple with coarser lee-side lenses, and (c) dune/ripple with foreset bedding (b and c modified from Wohletz and Sheridan 1979). In layer 1a undulation bed forms, which bear no obvious relationship to substrate roughness, are common in the Kingman area. Westward these are replaced by bed forms shown in (b) and (c), which commonly are associated with substrate roughness. In layer 1b the cross bedded forms (b,c) are common throughout the extent.

(a)



(b)



(c)

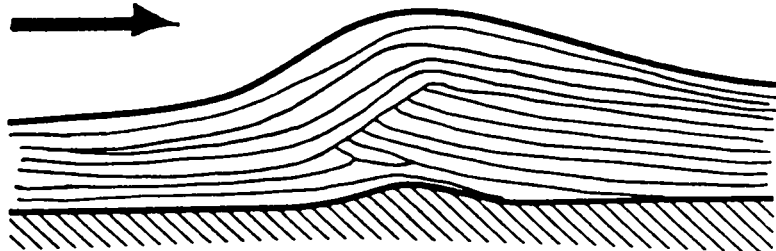


Figure 1-9: Photograph of undulation bed forms above a planar basal contact of the layer in the Kingman area.



but most commonly is between 5 and 10 cm in thickness. In the Kingman area lateral discontinuity was caused by erosion by the overlying pyroclastic flow in some cases, but in others the layer was apparently deposited as lenses that extend 5-10 m laterally. Layer 1b consists mostly of coarse ash (Figure 1-10b) in laminae to very-thin beds of 2 cm maximum thickness. Individual laminae are commonly normally graded and grey to purple in color reflecting a high concentration of lithic fragments. A few white laminae with high pumice concentration also occur.

Layer 1b in the Kingman area is typically cross bedded in low-angle, subtle dune forms. Layering is accentuated by lithic and crystal-rich zones that occur as small pod-shaped bodies, representing lee-side lenses of the low angle dune forms. Wavelengths range between about 5 and 30 cm. As in layer 1a, the 1b dune forms show both downstream and upstream migration of crests.

#### Layer 1c

Layer 1c in the Kingman area is generally massive, and ranges in thickness from 5-35 cm. It consists mainly of pumice and is white to tan in color. The layer is typically normally graded with grain sizes ranging from coarse ash to small lapilli (Figure 1-10c). The base of the layer has a relatively high lapilli content compared to upper parts, and is mainly clast supported. The coarse ash content increases upward until isolated lapilli are set in a coarse ash matrix. In a few places the full layer 1c is preserved (Figure 1-7c) but in most exposures all but the lowest few centimeters have

been eroded away during transport of the overlying pyroclastic flow. Where the full thickness of the layer is preserved, the top 10 cm is cross laminated coarse ash. The top surface of layer 1c is shaped into dunes of 2-8 m wavelength and 20-30 cm amplitude, with a sharp contact with the overlying layer 2. In most places incorporation of 1c into the pyroclastic flow has resulted in only the massive lower part of the layer being preserved, with a gradational (over 2-5 cm) contact with layer 2.

Average maximum lithic and pumice fragment diameters in layer 1c range from 1.8-0.6 and 1.7-0.7, cm, respectively, at Kingman. At one location, two large lithic fragments (22 and 27 cm) were observed in the middle of layer 1c with no associated impact sag structures, indicating that they were emplaced by flowage.

#### Regional Variations

The layer 1 deposits have been correlated over distances of 70 km eastward from Kingman. Figure 1-6 shows the regional correlation of stratigraphy for various outcrop areas shown on Figure 1-2. Characteristics of layer 1 at each major outcrop area are summarized in Table 1-1.

Layer 1a gradually thins and becomes finer grained with increasing distance from source. While features I refer to as undulation bed forms (wavy with parallel beds) are common in the Kingman area, to the east these are replaced by cross bedded forms that, in most cases, are developed above irregularities on the substrate. As discussed above, at Kingman the transition from fine-

Table 1-1: Regional Layer 1 Characteristics.

EXPOSURE AREAS							
LAYER	CHARACTERISTICS	KINGMAN	VALENTINE	PEACH SPRINGS AND MILKWEED CANYONS	NORTHERN AQUARIUS MOUNTAINS	WESTERN AQUARIUS MOUNTAINS	TROUT CREEK
Layer 1a	<p>Thickness Color Grain Size Composition Bed Forms</p> <p>Lateral Continuity</p>	<p>40-80 cm White Coarse ash fine lapilli Mainly pumiceous Very thin to thin beds in plane parallel form or displaying undulating bed form (see text for detail). Cross bedding relatively rare. 0.5 m <math>\lambda</math> x 2 m <math>A</math>. At 30 cm</p> <p>Continuous</p>	<p>15-40 cm White Coarse ash Pumiceous Plane parallel laminated where substrate is smooth. Cross laminated dunes and ripples (<math>\lambda</math> &lt; 50 cm, <math>A</math> &lt; 5 cm) occur above substrate roughness. Lipsueam crest migration rare. Lenses are 0.2-0.8 cm thick.</p> <p>Continuous</p>	<p>3-15 cm White Coarse ash Pumiceous Fairly laminated and bedded, mostly plane parallel with rare cross bedding.</p> <p>Continuous</p>	<p>20-25 cm White Coarse ash Pumiceous Lower 5 cm is planar to low angle cross bedded, individual beds &lt; 0.5 cm thick. Middle 10 cm is massive. Upper 5-10 cm is planar to cross bedded, very thin beds.</p> <p>Continuous</p>	<p>15-20 cm White Coarse ash Pumiceous Lower 5 cm is planar to low angle cross-bedded, individual beds &lt; 0.5 cm thick. Middle 10 cm is massive. Upper 5 cm is planar to cross-bedded, very thin beds.</p> <p>Continuous</p>	<p>5 cm White Coarse ash Pumiceous Massive</p> <p>Continuous</p>
Layer 1b	<p>Thickness Color Grain Size Composition Bed Forms</p> <p>Lateral Continuity</p>	<p>0-15 cm Grey to purple, some white beds Coarse ash Mainly lithic material Low angle cross laminated and bedded. Individual beds or lenses are less than 2 cm thick. Two side lenses occur associated with dunes. 5 m &lt; <math>\lambda</math>, &lt; 30 cm, <math>A</math> &lt; 5 cm</p> <p>Lenses with 5-10 m wavelength</p>	<p>0-30 cm Light grey Coarse ash Pumiceous with 10-20% lithic fragments Plane parallel laminated to cross laminated dunes and ripples (<math>\lambda</math> &lt; 50 cm, <math>A</math> &lt; 5 cm). Upstream crest migration rare. Lenses are 0.1-0.8 cm thick.</p> <p>Lenses with 2-15 m wavelength</p>	<p>0-15 cm Light grey Coarse ash Pumiceous with &lt; 10% lithic fragments Fairly laminated, mostly plane parallel with rare cross lamination.</p> <p>Lenticular</p>	<p>0-12 cm Light grey Coarse ash Pumiceous with 10-20% lithic fragments Laminated to very thinly bedded, abundant low-angle cross bedding.</p> <p>Lenses with 5-8 m wavelength</p>	<p>0-12 cm Light grey Coarse ash Pumiceous with 10-20% lithic.</p> <p>Lenses with 5-8 m wavelength</p>	<p>Not Present</p>
Layer 1c	<p>Thickness Color Grain Size Composition Bed Forms</p> <p>Lateral Continuity</p>	<p>5-35 cm White to tan Coarse ash - fine lapilli Mainly pumiceous Massive, normally graded lower parts. Upper 10 cm, where preserved, is cross laminated coarse ash with 2 m &lt; <math>A</math> &lt; 8 m and 20 cm &lt; <math>A</math> &lt; 30 cm.</p> <p>Continuous</p>	<p>0-15 cm White to light grey Coarse ash - fine lapilli Pumiceous with &lt; 10% lithic fragments Massive in most exposures. In thickest exposures the upper 2-3 cm is cross laminated coarse ash.</p> <p>Lenses with 2-15 m wavelength, thickness between layer 1b lenses</p>	<p>0-4 cm Light grey Coarse ash Pumiceous with &lt; 10% lithic fragments Massive with rare cross lamination.</p> <p>Lenticular</p>	<p>0-8 cm White to light grey Coarse ash Pumiceous with &lt; 20% lithic fragments Massive with rare cross lamination.</p> <p>Lenses with 5-8 m wavelength, thickest between layer 1b lenses</p>	<p>0-8 cm White to light grey Coarse ash Pumiceous with &lt; 20% lithic fragments</p> <p>Lenses with 5-8 m wavelength, thickest between layer 1b lenses</p>	<p>Not Present</p>
Fine Ash Layer	<p>Stratigraphic position Thickness Post-depositional features</p>	<p>Between layers 1a and 1b (FA1) 1-2 cm Flame structures</p>	<p>Between layers 1a and 1b (FA1) 2-5 cm Rare dipole loading structures extending upward into layer 1b</p>	<p>Between layers 1a and 1b (FA1) 2-3 cm Desiccation cracks in exposure of top surface</p>	<p>Between layers 1a and 1b (FA1) 2-3 cm None observed</p>	<p>Beneath layer 1a (FA0) Between 1a and 1b (FA1) FA0=1-2 cm, FA1=2-3 cm FA0 is discontinuous due to cracks and loading FA1 - none observed</p>	<p>Beneath layer 1a (FA0) only 2 cm Discontinuous due to cracks and loading</p>

grained at the base (1a<sub>1</sub>) to coarser-grained in the middle (1a<sub>2</sub>) is sharp and erosional, above which 1a<sub>2</sub> gradually grades upward into the finer top. In more distal locations the distinction between 1a<sub>1</sub> and 1a<sub>2</sub> is not as well defined, but is generally reflected by the occurrence of faint bedding structures at the bottom and top of layer 1a, with a massive middle. Upstream migration of bed forms is less common in eastern locations than in the Kingman area.

Regional variations of layer 1b contrast with those of layer 1a in three main aspects. First, layer 1b thickness decreases more gradually with increasing distance from source (in some places 1b thickness seems independent of flow distance). Second, it displays well defined low-angle cross bedding of very-thin beds to laminae throughout its extent. Third, the grain size of layer 1b remains fairly constant everywhere, consisting almost entirely of coarse ash at any given outcrop. Layer 1b retains its laterally discontinuous and lenticular character throughout the study area. The layer displays a decrease in lithic fragment and crystal content and resulting increase in pumice content along flow direction.

Eastward, layer 1c tends to become lenticular and fills in troughs between layer 1b lenses. The layer also becomes thinner overall to the east and its grain size decreases.

## LABORATORY DATA

### Granulometry

Grain size data are limited because the layer 1 deposits are indurated in many areas. Many samples taken from the Kingman area, however, were relatively unconsolidated so that sieve analysis could be performed after disaggregation. Because of incomplete disaggregation in some samples, and artificial fragmentation in others, I do not feel that the data are of sufficient quality for detailed consideration of such granulometric parameters as sorting coefficients and skewness. Instead, I show the sieve results in terms of weight percentages of lapilli ( $> 2$  mm), coarse ash (2 mm to 1/16 mm), and fine ash ( $< 1/16$  mm) in ternary plots (Figure 1-10) for layers 1a, 1b, and 1c. The samples shown were collected at 14 stratigraphic sections in the Kingman area. Fragments larger than lapilli size are rare in the deposits. The fine ash layer FA1 is indurated at all observed exposures, therefore no sieve data was obtained for the layer.

Layer 1a (Figure 1-10a) contains very little fine ash ( $< 3\%$  for all samples). Samples from the basal part (1a<sub>1</sub>) contain 88% to 99.5% coarse ash and less than 10% lapilli. Layer 1a<sub>2</sub>, on the other hand, ranges up to 31% lapilli, with the fraction of lapilli decreasing upward in the section. Layer 1b (Figure 1-10b) consists of greater than 94% coarse ash, with no more than 3% fine ash and 5% lapilli. Layer 1c (Figure 1-10c) contains less than 4% fine ash,

but ranges from 4-45% lapilli, with coarser samples tending to occur in the lower parts of the layer.

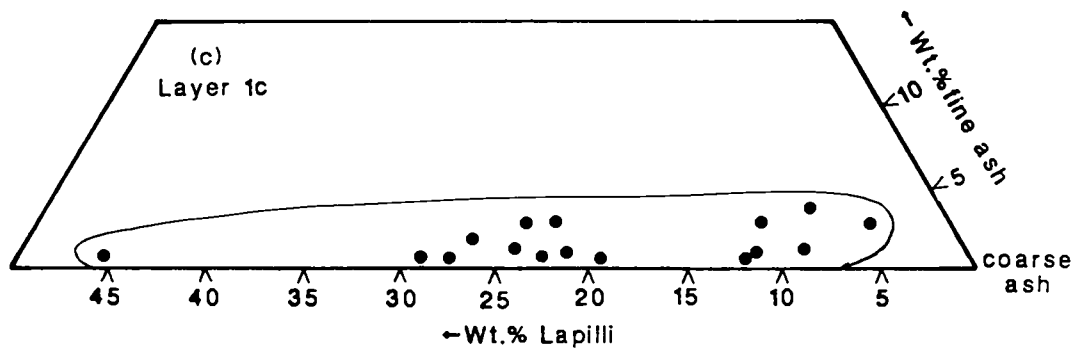
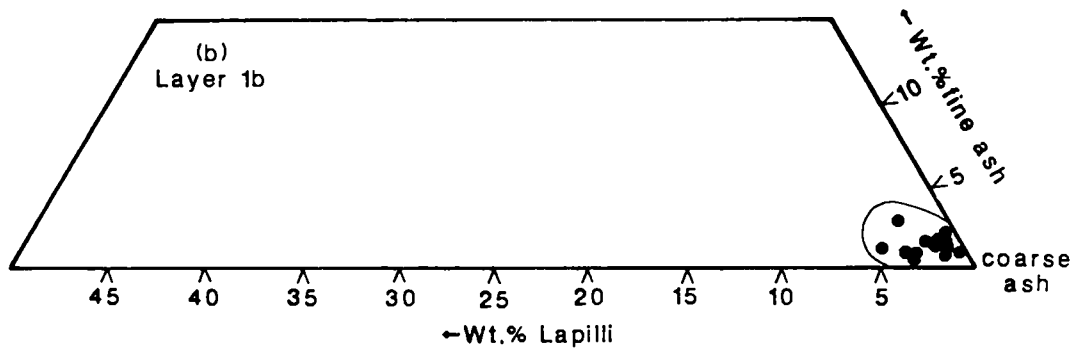
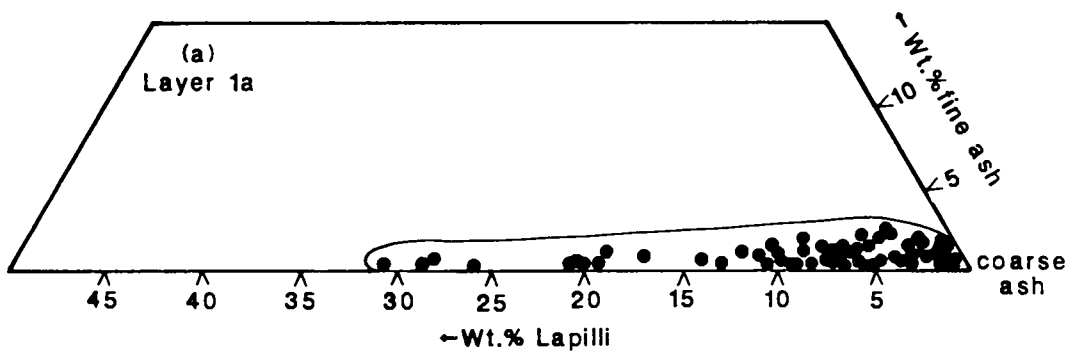
Eastward from Kingman the layer 1 deposits move toward the coarse-ash vertex so that better sorted grain size distribution occurs, reflecting improved sorting of the deposit with increasing distance from vent. This is based on visual examination and sieve data from two locations on the Colorado Plateau.

#### Component Analysis

The 0.25 mm grain-size fractions of samples from the Kingman area were point counted using an optical microscope. Components were divided into four categories: crystals, lithic fragments, shards produced by magmatic fragmentation, and shards produced by hydroclastic (magma-water interaction) processes. Criteria for distinguishing between shard types are discussed below. 109 samples were analyzed, with 500-600 grains counted on each sample. It is thought that this approach allows one to study relative variations in the composition of material produced at the vent(s). An analogous study of a basaltic eruption which addresses stages of magma degassing and magma-water interaction is that of Houghton and Schmincke (1986).

The 0.25 mm size fraction was chosen for analysis because all of the clast types occur at that size. For example, larger size fractions may not contain any hydroclastic shards, while smaller fractions may not contain many crystals.

Figure 1-10: Granulometric data from layer 1 in the Kingman area in terms of weight percent lapilli, coarse ash, and fine ash. (a) Data for layer 1a, with all samples containing greater than 10% lapilli corresponding to the coarser top half of the layer (1a<sub>2</sub>). (b) Layer 1b. (c) Layer 1c. In layer 1c, coarser samples tend to occur at the base of the layer.



Mode of shard fragmentation (magmatic or hydroclastic) was determined by the morphology and vesicularity of fragments (Wohletz 1983; Fisher and Schmincke 1984, Table 5-3; Heiken and Wohletz 1985). Highly vesicular shards are interpreted to have been produced by magmatic fragmentation. Blocky, non-vesicular, and poorly vesicular shards with curvilinear surfaces crosscutting vesicles are interpreted to have been produced by hydroclastic processes. Scanning electron microphotographs of representative magmatic and hydroclastic shards in the PST are shown in Figure 1-11. Bubble wall shards, which are common in other silicic hydrovolcanic deposits (e.g., Heiken and Wohletz 1985, pp. 116-117), can be produced by both magmatic and hydroclastic processes but were assumed to be magmatic in this study.

Data from the component analyses are displayed in ternary plots with vertices given by percentages of hydroclastic shards, magmatic shards, and lithic fragments (Figure 1-12). The left-hand side of these ternary plots, connecting the hydroclastic-shard and magmatic-shard vertices, represents a purely juvenile composition. The lithic-fragment vertex represents a purely accidental composition. Crystal content is not shown on the plots, since it is assumed that the ratio of crystals liberated from magma by magmatic fragmentation to those liberated by hydroclastic fragmentation is approximately equal to the ratio of magmatic shards to hydroclastic shards (ignoring the minor xenocrystic component). Crystals consist mainly of feldspars, biotite, and hornblende, and sparse quartz. Although

identification of rock types is difficult at 0.25 mm, it appears that lithic fragments are mainly volcanic.

Results for layer 1a are shown in Figure 1-12a. The plot shows that juvenile particles produced by magmatic fragmentation dominated the beginning of the eruptive event. The transition to coarser material upward (layer 1a<sub>2</sub>) is reflected by a sudden increase in concentration of hydroclastic shards and accidental lithic fragments. The top of layer 1a records a gradual return to juvenile clasts produced by magmatic fragmentation.

Layer 1b (Figure 1-12b) has a relatively high content of hydroclastic shards. It also is bimodal in terms of content of juvenile material. Most of the samples are quite high in lithic fragment content (35-60%), which produces the dominantly grey coloring of the deposit in the field. However, a few samples of locally exposed white beds retain the same range of hydroclastic shard concentration as the grey layers, but are mainly juvenile with only 6-12% lithic fragments. Thus layer 1b reflects a strong hydroclastic blasting event, where most of the material is accidental and is shattered down to coarse-ash size with occasional juvenile-component-rich pulses during the event.

Layer 1c samples, plotted in Figure 1-12c, also have a relatively high hydroclastic component. They are, however, mainly juvenile material.

Layer 2, the main pyroclastic flow deposit, examined in thin section, contains sparse hydroclastic shards. These may have been

Figure 1-11: Scanning electron microphotographs of shards from layer 1 (0.25 mm sieve fraction). Scale bar is 100 microns (0.1 mm). (a) Typical highly vesicular shard produced by magmatic fragmentation processes. (b) Poorly vesicular shard produced by hydroclastic processes. Note curvilinear surface cross cutting a vesicle and conchoidal fracture surface in (b).

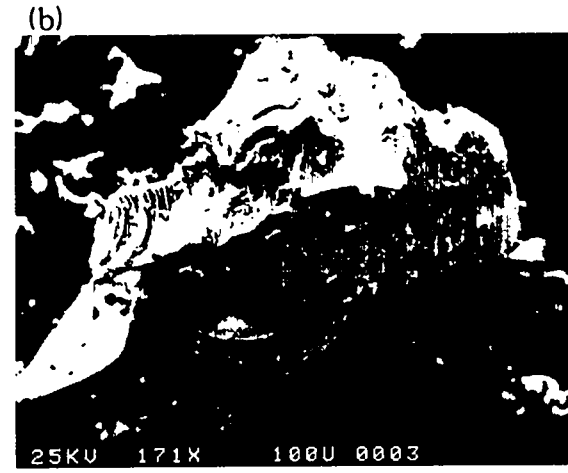
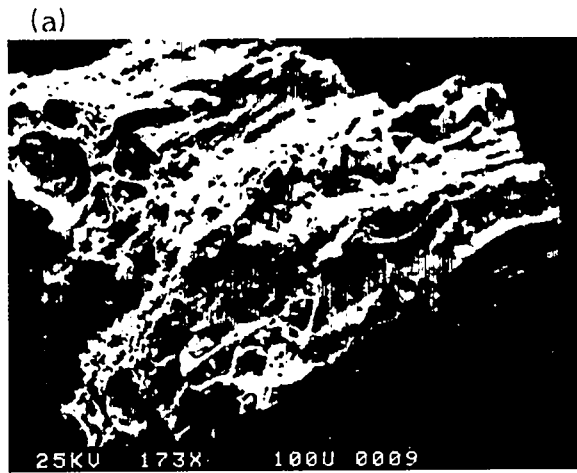
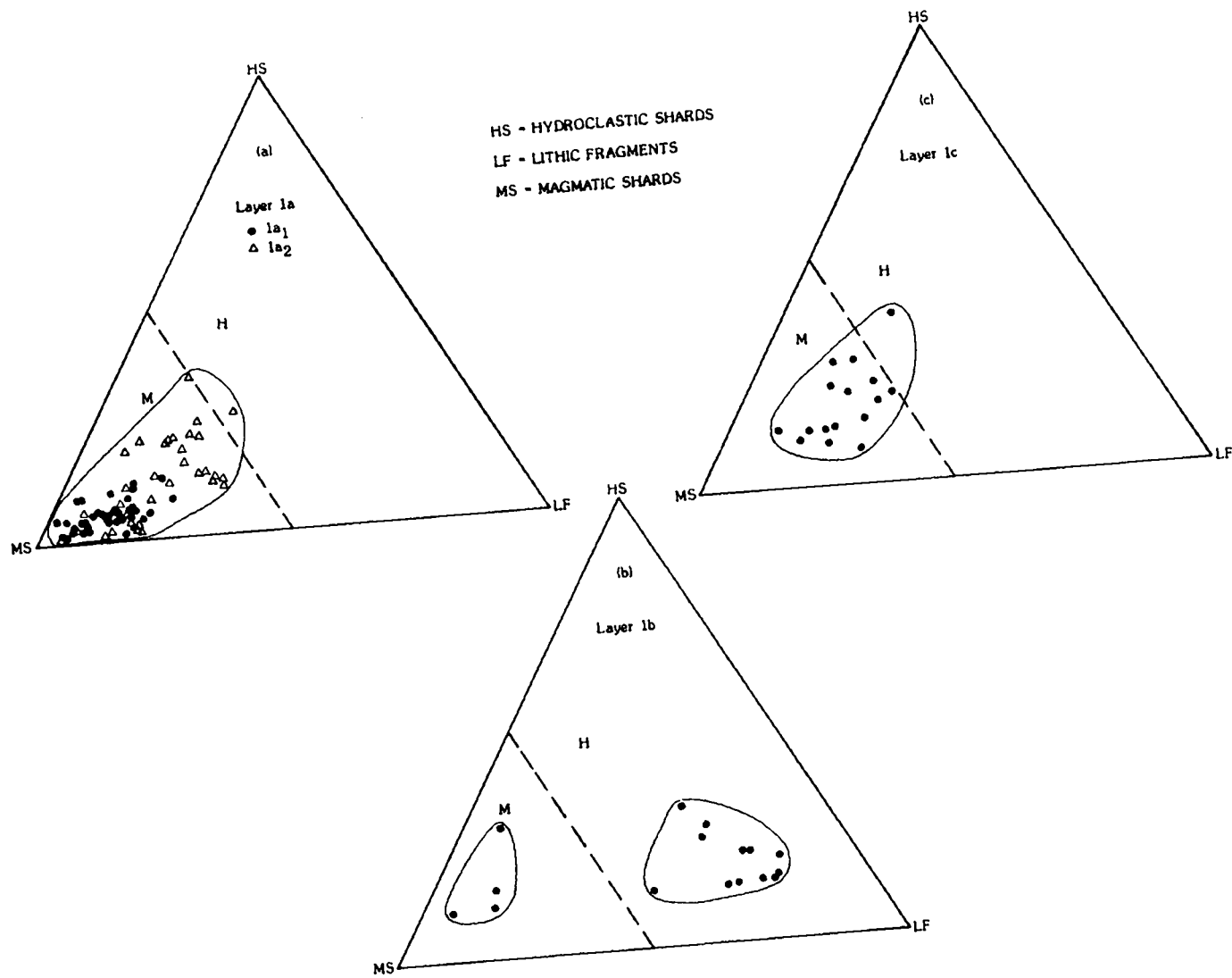


Figure 1-12: Ternary diagrams of percentage of hydroclastic shards, magmatic shards, and lithic fragments in the 0.25 mm sieve fraction. Samples that plot close to the left-hand side of the diagrams (connecting hydroclastic and magmatic vertices) have a dominantly juvenile composition, while samples near the lithic-fragment vertex are dominantly accidental in composition. The dashed line corresponds to 50% magmatic shards, and separates the diagrams into two fields representing dominantly magmatic fragmentation (M) and hydroclastic fragmentation (H), assuming that a high lithic content indicates hydrovolcanic activity. (a) Data for layer 1a (with subdivisions 1a<sub>1</sub> and 1a<sub>2</sub>). Points plotting near the M-H boundary are from the lower part of 1a<sub>2</sub>. (b) Data for layer 1b, showing bimodal composition which mainly reflects bimodal lithic content. (c) Layer 1c.



incorporated from the underlying layer 1 deposits. It appears that fragmentation during the "steady" pyroclastic flow phase was mostly or entirely due to magmatic processes. Figure 1-13 qualitatively shows the relative variations in contributions of hydroclastic and magmatic fragmentation recorded at various levels in the layer 1 sequence.

INTERPRETATION: INITIAL PHASES OF THE PEACH SPRINGS TUFF ERUPTION

Field characteristics of layer 1 deposits in the Peach Springs Tuff indicate that they were deposited by pyroclastic surges. Layer 1 almost everywhere displays wavy bedding (with or without cross bedding). In the eastern exposures, cross bedding is commonly associated with visible substrate roughness elements such as rocks jutting above the paleosol, and is especially well developed on the east-facing (lee) sides of these roughness elements. Reverse to normally graded beds also suggest lateral movement of clasts in a thin traction carpet. These features are typical of pyroclastic surge deposits and indicate lateral transport instead of deposition by fallout (Moore 1967; Fisher and Waters 1970; Waters and Fisher 1971; Schmincke et al. 1973; Crowe and Fisher 1973; Sparks and Walker 1973; Wohletz and Sheridan 1979; Walker 1984; Sigurdsson et al. 1987). Origin as pyroclastic flows is not supported because layer 1 is well-sorted relative to layer 2 and because it is not significantly ponded in topographic lows (Wright et al. 1980).

The low-angle nature of cross bedding and absence of accretionary lapilli in the layer 1 deposits suggests that they were

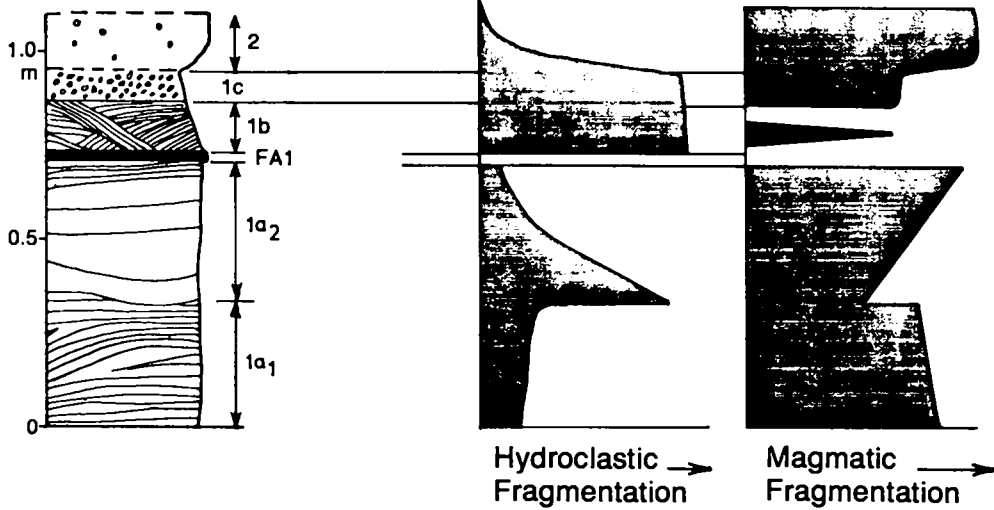
emplaced by "dry" pyroclastic surges (Heiken and Wohletz 1985).

The fine ash layer found beneath layer 1a in the southeast (FA0) and that found between layers 1a and 1b (FA1), are both interpreted as fallout layers because they are generally massive on a small scale and are relatively well-sorted. FA1 may represent fallout of fine material winnowed from the layer 1a pyroclastic surge and is regarded as a "co-surge" fallout. This interpretation is supported by its lateral continuity and by the fact that it does not thin away from the vent. In a gross sense FA1 is similar to the ash layer that occurs on top of the 18 May 1980 blast deposit at Mount St. Helens (Fisher et al. 1987). Based on the chronology of that eruption (Criswell 1987) I estimate that the minimum time for accumulation of FA1 was on the order of one hour.

Several ideas on the origin of pyroclastic surge deposits at the base of ignimbrites (i.e. ground surges; Sparks et al. 1973) have been suggested, and all but one of these models can be ruled out for open-valley layer 1 deposits for two main reasons: (1) accumulation of the fine ash layer records a time break on the order of an hour between periods of lateral transport, and (2) shard types in layer 1 differ from those in layer 2. These two observations rule out any model based on processes directly associated with the moving pyroclastic flow, such as explosive jetting (Wilson and Walker 1982) and turbulent boundary layers (Valentine and Fisher 1986). Although less strongly, the layer 1 compositional data do

Figure 1-13: Diagrammatic representation of the relative importance of magmatic and hydroclastic fragmentation processes during the eruption as recorded by the deposits. Layer 1a<sub>1</sub> records an initial phase of dominantly magmatic fragmentation. 1a<sub>2</sub> represents a brief pulse of hydroclastic fragmentation followed by a return to magmatic fragmentation. FA1 records a break in eruptive activity, which is followed by highly hydroclastic layer 1b. Layer 1b records some brief pulses of magmatic fragmentation as indicated by its bimodal composition (Figure 1-12b). Layer 1c records a return to magmatic fragmentation that eventually leads to the main layer-2 forming phase of the eruption.

LAYER 1 STRATIGRAPHY  $\xrightarrow{\text{reflects}}$  FRAGMENTATION / EXPLOSION PROCESSES



not support an origin of the surges by initial collapse of the eruption column (Fisher 1979).

The most likely origin for these surge deposits is from initial blast phases of the ignimbrite eruption. The significance of blast phenomena in explosive volcanism has recently been emphasized by Kieffer (1981), who found that observations of the initial phase of the 18 May 1980 eruption of Mount St. Helens could be explained in terms of overpressured jet dynamics. More recently, Wohletz et al. (1984) numerically simulated the initial stages of large-volume eruptions, where a dike of volatile-rich magma is catastrophically exposed to atmospheric pressure. The result of this process is a phase of highly unsteady flow, with expansion (rarefaction) waves propagating down the conduit and shock waves propagating into the atmosphere and along the ground. During this phase of an eruption, pyroclastic surges within a few tens of kilometers of the vent are driven largely by shocks and are characterized by pulsing, unsteady flow. This "blast phase" is followed eventually by relatively steady discharge, which is thought to produce pyroclastic flows. The blasting phase of an eruption may have any number of pauses that last for periods of up to weeks or months, thus solving the problem of the time break for fine ash fallout. Blasting may be caused by either purely magmatic or hydromagmatic processes (or any combination of the two) and thus may produce different shard types than later phases of the eruption, so that the compositional differences between layer 1 and layer 2 can be explained.

By combining field data, component analysis, numerical modeling, and ideas on magma-water interaction (Wohletz 1986) a sequence of eruption and emplacement events corresponding to the layer 1 deposits can be inferred. It is important to keep in mind that, because of the lack of knowledge about the source of the PST, the interpretations below may be only part of a much more complex sequence of events.

#### Lower Fine Ash Layer (FA0)

The lower fine ash layer, which occurs only in the southeastern part of the study area, probably represents the distal fallout from a weak precursor blast event. This event may have been associated with initial stages of magma ascent in a dike (Figure 1-14a), the geometry of which is unconstrained. The fact that FA0 is only found in the southeast part of the area is probably a result of a northwest-to-southeast wind at the time of the event.

#### Layer 1a

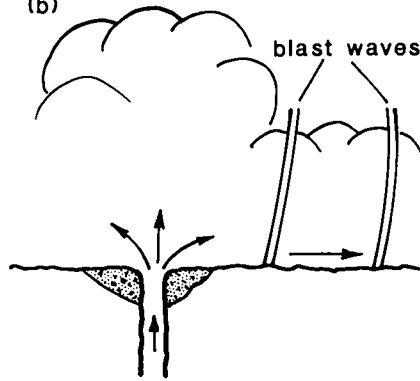
When the dike was relatively close to the surface, its overburden burst open, allowing rapid decompression of the magma and blasting phenomena such as those modeled by Wohletz et al. (1984) (Figure 1-14b). Vesiculation produced shards with characteristics of magmatic fragmentation, and the erupted material was mainly juvenile. Layer 1a surges moved across the landscape to produce the most widespread and continuous of the surge deposits. Many of the features of layer 1a parallel trends of the 1982 El Chichon surge deposits described by Sigurdsson et al. (1987). The reverse-to-

Figure 1-14: Interpreted events at the beginning of the Peach Springs Tuff eruption that produced the observed layer 1 sequence. Initially magma (shaded) moved to the surface, probably as a dike (a). The overburden of the dike eventually failed, leading to rapid decompression and vesiculation, and resulting blasting phenomena to produce layer 1a (b). As the blasting progressed, the vent walls (dotted pattern) failed and collapsed (c), plugging the vent and producing a period of relative quiescence during which the fine-ash layer FA1 was deposited. During this period of quiescence, magma interacted with ground water, eventually leading to lithic-rich, hydrovolcanic blasts and deposition of layer 1b (d). As the vent was cleared, erupting material became dominantly juvenile in composition during the final phase of blasting (e), which led directly to the long period of steady discharge that produced layer 2 (f). Detailed discussion in text.

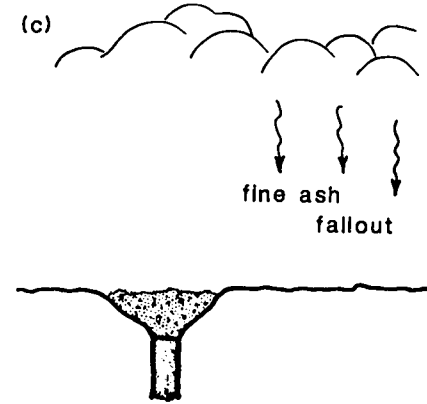
(a)



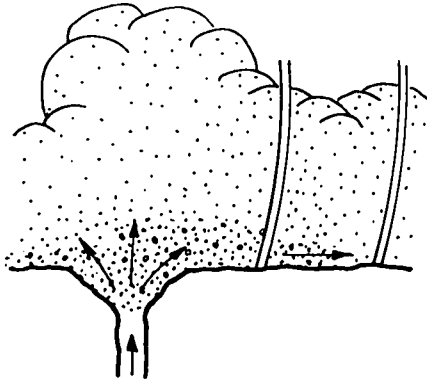
(b)



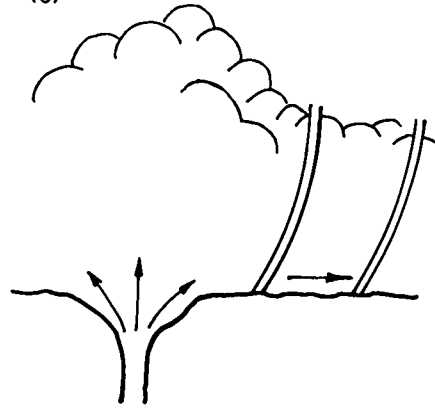
(c)



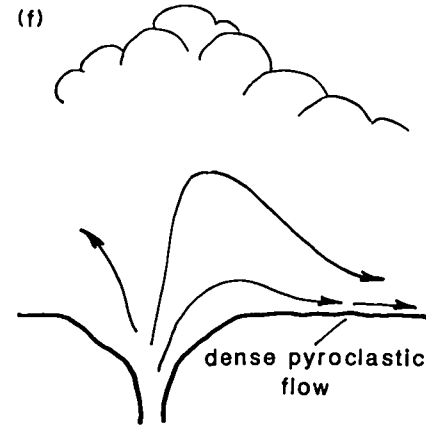
(d)



(e)



(f)



normal grading of the overall layer reflects an increase in flow power with time, in this case rather abruptly as demonstrated by the erosional surface between  $1a_1$  and  $1a_2$  with its lack of fallout or locally-reworked tephra deposits. The increase of flow power corresponds to an increase in magma-water interaction (Figure 1-13). This was followed by a decrease in magma-water interaction as the layer 1a surge event waned. With increasing flow distance the internal stratification of layer 1a is progressively less well defined. This appears to result from improved sorting with flow distance -- as the tephra becomes almost entirely coarse ash there is less textural distinction between beds. In addition, this trend may result from a gradual transition from sandwave to massive facies (Wohletz and Sheridan 1979) due to stratified flow effects (Chapter 2; Valentine 1987). The change from upstream to downstream migration of bed forms may reflect a gradually decreasing Froude number (defined for continuously stratified flow as in Chapter 2) with distance. Internal structures of individual beds, such as symmetric and normal grading, can be explained in terms of high-concentration bed loads where particle size sorting is relatively poor (compared to eolian sands, for example) and where grain-dispersive processes occur. This has been discussed in detail by Sigurdsson et al. (1987) in their study of pyroclastic surges from the 1982 El Chichon eruption.

An interesting feature of layer 1a is the proximal-to-distal change in bed form character from "undulation bed forms" (Figures 1-

8 and 1-9) to more angular, cross-stratified bed forms (Figure 1-8). A possible explanation of this results from extending the ideas of Sigurdsson et al. (1987) and experimental studies discussed by Jopling and Walker (1968). Sigurdsson et al. (1987) discuss how a low concentration bed load (consisting of more-or-less individually saltating grains) moves up the stoss side of a bed form, accumulating grains at the top until avalanching occurs down the lee side. This process, combined with periods of erosion (Jopling and Walker 1968), produces the familiar cross bedded dune. The same process may happen in an antidune, except there avalanching can occur down the stoss side. However, if there is a high rate of material supply from the suspended load to the bed load, the avalanching process can be effectively overwhelmed. In this case a high concentration bed load moves in a continuous manner over bed forms, and this is preserved in the resulting deposits. When a continuous bed load freezes (its yield strength surpasses the shear stress) under such conditions, experiments show that it is rapidly buried by material coming out of suspension, thus preventing stoss- or lee-side erosion (Jopling and Walker (1968). Yield strength of the bed load is strongly influenced by its sorting -- poorer sorting results in higher yield strength. Thus, the change in bed form character with distance that is observed in the Peach Springs Tuff may be explained in terms of decreasing concentration of the suspended load and improved sorting of material supplied to the bed load with increasing flow distance.

Another question related to bed forms is: What causes the initial perturbation in the bed that results in waviness? In the exposures to the east of Kingman, it appears that most bed forms occur in response to substrate irregularities such as rocks jutting above the paleosoil, as discussed in the descriptions. In the Kingman area, however, this is typically not the case. Instead, initial beds are horizontal and planar. At some point above the substrate, say two or three beds up, a slight thickening or thinning occurs in a bed. Each bed above this progressively amplifies the perturbation. So it is apparent that something happened during the surge event that caused perturbations in otherwise constant-thickness, planar beds.

Three possible mechanisms for bed perturbation can be envisioned. The first is the result of a random (turbulent) fluctuation in velocity that causes a slight amount of deposition or erosion from the bed. Second, the perturbation may be the result of Kelvin-Helmholtz (shearing) instability between the bed load "fluid" and the overlying surge (this type of instability is responsible for wind-induced waves on the surface of a body of water). The third possibility is that the perturbations are induced by the passage of pressure waves or shocks through the surge. When a shock is passed over a granular deposit, bed particles experience a lift force due to the change in velocity across the shock (Hwang 1986). The bed immediately behind the shock has been observed in experiments to take on a wave-like configuration (Borisov et al. 1967), possibly

influenced by internal waves that occur in the density-stratified surge (Chapter 2; Valentine 1987). If the PST layer 1 deposits are indeed the result of blast phenomena, then shocks are expected to occur in the surges (Wohletz et al. 1984). The observation that these bed perturbations (occurring within the surge deposit) are found mainly in the Kingman area, but not to the east, may reflect gradual dissipation of shocks with increasing flow distance. I know of no way to prove this idea from field measurements at the present time, but a shock-induced origin is a viable possibility.

It is worth noting that similar bed-form initiation features (small perturbations in otherwise planar beds) have been observed in pyroclastic surge deposits around maar volcanoes (e.g. Fisher and Waters 1970; Crowe and Fisher 1973; Schmincke et al. 1973) and possibly in proximal veneer deposits of the Taupo ignimbrite (Wilson 1985). Especially in the case of maar volcanoes it is expected that numerous shocks will be produced by magma-water interaction. The occurrence of these features in such environments may indicate that shock-induced bed forms are a common phenomenon.

#### Fine Ash Layer (FA1)

Apparently the vent walls became unstable and eventually collapsed, temporarily clogging the vent (Figure 1-14c). This brought the layer 1a-producing event to an end and allowed time for deposition of FA1, the "co-surge" fallout deposit. FA1 may initially have been damp, as evidenced by dessication cracks and plastic deformation into flames and diapir-like structures. In the

Kingman area, dispersed coarse-ash sized crystals and lithic fragments in the top few millimeters of FA1 may represent a resumption of explosive activity that led to deposition of layer 1b.

Layer 1b

During the inferred lull in explosive activity recorded by FA1, magma was able to interact with meteoric water. This may have been enhanced if the vent-clogging material, which probably had a high permeability, contained appreciable ground water. In addition these conditions may have allowed degassing of some of the magma by flow of volatiles through porous walls and vent-clogging material (Eichelberger et al. 1986), enhancing the low vesicularity of layer 1b shards. Eventually, magma-water interaction led to violent hydrovolcanic blasting (Figure 1-14d), shattering the vent-clogging material to ash size and producing hydroclastic shards. For short intervals during this phase the eruption was dominated by juvenile material to produce a few white beds, but for the most part lithic-rich pyroclastic surges moved outward to deposit layer 1b. The 1b-producing surge is interpreted to have carried a relatively sparse pyroclastic load. This load was deposited through a thin bed load in very low profile dune forms (resulting in the layer's lenticular character). The bed load was of relatively low concentration and was relatively well-sorted, allowing avalanching over the flanks of ripples and low-angle dunes to produce cross bedding. However, despite the small sediment load of the surge, it was powerful enough

to flow distances of at least 100 km with no dramatic changes in thickness of its deposits.

#### Layer 1c

As the vent was cleared, juvenile material replaced accidental material for a brief phase of continued hydrovolcanic blasting and deposition of layer 1c (Figure 1-14e). In the most proximal part of the study area, 1c has a coarser bottom that grades upward into a finer-grained, cross bedded top, resembling in a general way the deposit of the 18 May 1980 Mount St. Helens blast (Hoblitt et al. 1981; Waite 1981; Fisher et al. 1987) and the S-1 surge deposit from the 1982 El Chichon eruption (Sigurdsson et al. 1987). The layer 1c surge is interpreted to have been very similar to that associated with layer 1a, although the 1c surge seems to have been a short-lived event relative to 1a. For example, the 1a surge probably resulted from numerous blasts at the vent, while the 1c surge may have resulted from one discrete blast.

#### Lateral Extent of the Pyroclastic Surges

A striking feature of the Peach Springs Tuff layer 1 deposits is their lateral extent. The pyroclastic surges that produced these deposits traveled a minimum of 100 km from source, and it is appropriate to consider possible (qualitative) explanations for this large flow distance. If these pyroclastic surges were indeed produced by blasting phenomena, a driving mechanism that may be of considerable importance is that of shock waves produced by blasting phenomena. The numerical modeling of Wohletz et al. (1984) suggests

that shock waves may dominate the flow for several tens of kilometers away from the vent during the blast phase of an eruption. Shock waves may serve to keep a surge turbulent as well as to provide momentum. Also, beyond the Kingman paleovalley the surges moved across a relatively smooth (low drag) terrain that sloped downward to the east.

Another possible contributing factor to the large flow extent may be atmospheric wind, which has been observed to influence historical pyroclastic surges (e.g. Waters and Fisher 1971). If there was a strong wind blowing to the east, it may have been able to take over particle transport when the surge's primary drive was lost. This is not favored because atmospheric wind would be expected to continue blowing after it had lost its pyroclastic load, which would not allow for deposition of the co-surge fine ash layer between layers 1a and 1b. Nevertheless, a contribution from atmospheric wind cannot be completely ruled out.

#### DISCUSSION

The open-valley layer 1 deposits of the Peach Springs Tuff record a complex blast phase, with variable interaction between the rising magma and ground- or surface-water. The strength of the blast phase, especially the part that led to layer 1b, may be partly responsible for the lack of a Plinian deposit at the base of the ignimbrite.

Four variables interact during an eruption to determine whether the eruption column will collapse or continue to high altitudes to produce a fallout deposit. Three of these -- vent radius, exsolved gas content, and exit velocity -- are discussed in detail by Sparks et al. (1978). The fourth, exit pressure, is discussed in Chapter 3 and by Valentine and Wohletz (1987). Low values of exsolved gas content, exit velocity, and exit pressure, and large vent radius tend to produce eruption columns that collapse. In the case of the Peach Springs Tuff eruption, where no Plinian fallout deposit has been observed, it is thought that vent radius and its effect upon exit pressure played the major role. Instead of the eruption beginning with a small vent (producing a Plinian eruption column) and subsequently evolving toward a wider vent for pyroclastic flows, the powerful blasting that is recorded in the layer 1 deposits rapidly produced a very wide vent (primarily during the phase that produced layer 1b). A wide vent will correspond to relatively low exit pressure, as discussed by Kieffer (1982). Thus the Peach Springs Tuff eruption bypassed a Plinian phase.

The importance of hydrovolcanic processes in other intermediate- to large-volume silicic eruptions has been discussed by Self and Sparks (1978), Self (1983), and McPhie (1986). I suggest that processes similar to those that occurred during the Peach Springs Tuff eruption may be important in many large-volume ignimbrite eruptions, which commonly lack significant fallout deposits (Lipman 1986). One would especially expect important

hydrovolcanic input in eruptions from nested or coalesced calderas, such as have occurred in the San Juan Mountains volcanic field of Colorado, U.S.A. (Steven and Lipman 1976; Lipman et al. 1973). In such cases, eruptions commonly occur through closed basins formed by earlier caldera collapse events. These closed basins may accumulate significant quantities of water both below the surface and in caldera lakes, which would aid in hydrovolcanic blasting.

## CHAPTER 2: STRATIFIED FLOW IN PYROCLASTIC SURGES

### INTRODUCTION

Pyroclastic surges are considered to be low-particle-concentration, high velocity flows that move in a dominantly turbulent mode (Wright et al. 1980). They leave relatively thin, bedded and cross bedded to massive deposits (Fisher and Waters 1970; Wohletz and Sheridan 1979; Walker 1984). Surges may originate by eruption column collapse, lava dome collapse, lateral blast (Hoblitt et al. 1981; Waite 1981; Fisher et al. 1987), blast wave phenomena (Wohletz et al. 1984), or as ash clouds generated by dense pyroclastic flows (Fisher 1979). Attention in recent years has been directed toward acquiring a more quantitative understanding of surge mechanisms; important works in this area include those of Wohletz and Sheridan (1979), Kieffer (1981), and Wohletz et al. (1984). Aspects of compressible flow are extremely important in modeling pyroclastic surges, and have been addressed in Kieffer (1981) and Wohletz et al. (1984). This chapter addresses application of stratified flow theory to surges, where the word "stratified" implies a density gradient from bottom to top of a surge, reflecting the solids concentration gradient.

The terms "surge" and "flow" as they are currently used in volcanology literature are ambiguous, since they are both really flows (see Wright et al. 1980). Pyroclastic surges are commonly defined as gas-particle mixtures where particle concentration is low

and rheology is approximately Newtonian, except in the bed-load region, where local particle transport may be by saltation and thin granular flow (Savage 1984; Campbell and Brennan 1985). Particle transport is dominated by turbulence in this definition of surges. Pyroclastic flows, on the other hand, are defined as high-concentration flows with characteristics approaching those of debris flows (Sparks 1976; Valentine and Fisher 1986). In addition, fluidization processes probably play a role in dense pyroclastic flows (Sparks 1976, 1978; Wilson 1980, 1984), while fluidization is relatively unimportant for low concentration surges. Another important distinction between pyroclastic flow and surge was recently proposed by Fisher (1986), who suggested that regional transport of particles and local deposition in the two types of systems have fundamentally different relationships. He suggested that the deposit of a pyroclastic flow and the flow itself are essentially the same. That is, the deposit represents the frozen flow, which corresponds with en masse deposition of pyroclastic flows that has been suggested by previous authors (Sparks 1976; Valentine and Fisher 1986). In contrast with this, pyroclastic surges have separate transport and depositional systems. The transport system of a surge is dominated by turbulence, while the depositional system depends upon local conditions and the amount of material supplied to it from the transport system. Thus, while a surge may leave local massive deposits that have characteristics of pyroclastic flow deposits, the material forming the deposits was

transported most of the distance from the vent by turbulent suspension. In this chapter I will retain the current usage of the terms "pyroclastic surge" and "pyroclastic flow" as defined in this paragraph, including the distinction made by Fisher (1986). "Surge" is often used by itself and means pyroclastic surge. "Flow," however, simply refers to fluid motions in general unless it is preceded by "pyroclastic."

This chapter centers on the effects of density stratification in flows dominated by turbulent transport of the pyroclastic material. The order of the chapter is as follows. After introducing important parameters of stratified flow theory, a possible relationship between internal gravity waves and surge bed form mechanics is proposed. Facies variations are then related to the stratified flow approach. This is followed by a discussion of the effects of density stratification on the interaction of pyroclastic surges with topography.

#### STRATIFIED FLOW PARAMETERS

The approach used here is the classical mixing length method for turbulent flow. Efficiency of particle transport at a given level in a turbulent flow depends on the scale of eddies, which affects the sediment diffusivity coefficient, at that level. Eddy and sediment diffusion profiles used for streams and flumes are assumed to be sufficient for application to pyroclastic systems. Although pyroclastic surges are probably compressible flows in most

cases, the use of steady, incompressible flow profiles is justified for the following reasons.

- (1) The main flow property in the relations discussed below is the mixing length, which describes the length scale over which momentum transfer occurs in a turbulent flow (Bird et al. 1960, p. 160). In compressible gas flows, the vertical (away from boundary) rate of increase of mixing length is affected by an increased temperature at the boundary due to viscous dissipation. This increased temperature reduces gas density at the boundary, which in turn results in a thickening of the boundary layer and decreasing friction coefficient (Liepmann and Roshko 1957, pp. 338-340; Schlichting 1979, pp. 715-723). In pyroclastic surges, the presence of particles results in the flows being nearly isothermal (see discussion by Kieffer 1981). Because of this, boundary effects that occur in single phase gas flows can be ignored.
- (2) Compressible flow of pyroclastic surges results in an acceleration component due to expansion or compression. If this acceleration is smooth (i.e. the flow is gradually varied), the steady flow relations should hold locally, although the sediment diffusion and concentration profiles at each section along the flow will be different. The relations do not hold at the location of a shock wave or hydraulic jump, where conditions are rapidly varied.

The empirical nature of the eddy diffusivity/mixing length method should be stressed: it does not describe the actual physics of the processes.

The sediment diffusion profiles used here have diffusion greatest in the core of the flows, decreasing to zero at the bottom and top (see discussion by Dingman 1984, pp. 166-173). This produces a nonlinear particle concentration gradient. In the core of a flow, where mixing is most efficient,  $d\rho/dy$  ( $\rho$  = density,  $y$  = vertical axis with origin at the base of the flow) will be at its lowest value. The gradient becomes stronger as the flow boundaries are approached because diffusion by eddy action is suppressed there. Symbols and their definitions are given in Appendix 2A.

Concentration profiles for turbulent transport systems are governed by the Rouse number, which is a ratio of particle settling velocities to the scale of turbulence. For flows with a single particle size, or when determining the ability of any flow to carry a specific particle size, the Rouse number is given by (see Middleton and Southard 1978, pp. 6.37-41)

$$Pn_i = \frac{w_i}{ku_*} \quad (2-1)$$

where  $Pn_i$ , the particle Rouse number, corresponds to particles with settling velocity  $w_i$  in a flow with shear velocity  $u_*$ . Von Karman's constant,  $k$ , is defined by  $k = L/y$ ,  $L$  being the mixing length. The commonly accepted value of  $k$  is 0.4. In actuality, the density

stratification inherent in turbulent suspensions influences the value of von Karman's constant, which in turn affects the density gradient. These complex interactions are just beginning to be understood (see, for example Delvigne, 1986), but for this chapter the constant value given above is adopted.

For a pyroclastic surge, which may have a wide range of particle sizes and settling velocities, a more comprehensive form of the Rouse number is

$$P_n = \frac{1}{S_{avg}} \sum_i S_i \frac{w_i}{ku_*} \quad (2-2)$$

Here,  $S_{avg}$  is the average volume concentration of all solids in the flow,  $S_i$  is the average volume concentration of particles in settling velocity class  $w_i$ .  $P_n$  is then the average of all particle Rouse numbers, each weighted according to its volume concentration, and is termed the "distribution" Rouse number.

To determine the density profile of a surge, begin with the following form of the concentration equation (Ghosh et al. 1986) which gives particle concentration ( $S$ ) as a function of height:

$$\frac{1}{S} \frac{dS}{d\eta} = -P_n \left( \frac{1}{\eta(1-\eta)} \right) \quad (2-3)$$

where  $\eta = y/d$  is the dimensionless height taking  $d$  as the total

flow thickness (see Figure 2-1). Integrating (2-3) to find the concentration profile we get

$$\frac{S}{S_0} = \left[ \frac{\eta_0}{1-\eta_0} \frac{1-\eta}{\eta} \right]^{Pn} \quad (2-4)$$

In this equation, zero subscript refers to conditions at a reference level in the flow. Equation (2-4) is plotted in Figure 2-1. For the density of the flow (mixture), the contribution of the gas phase is neglected so that

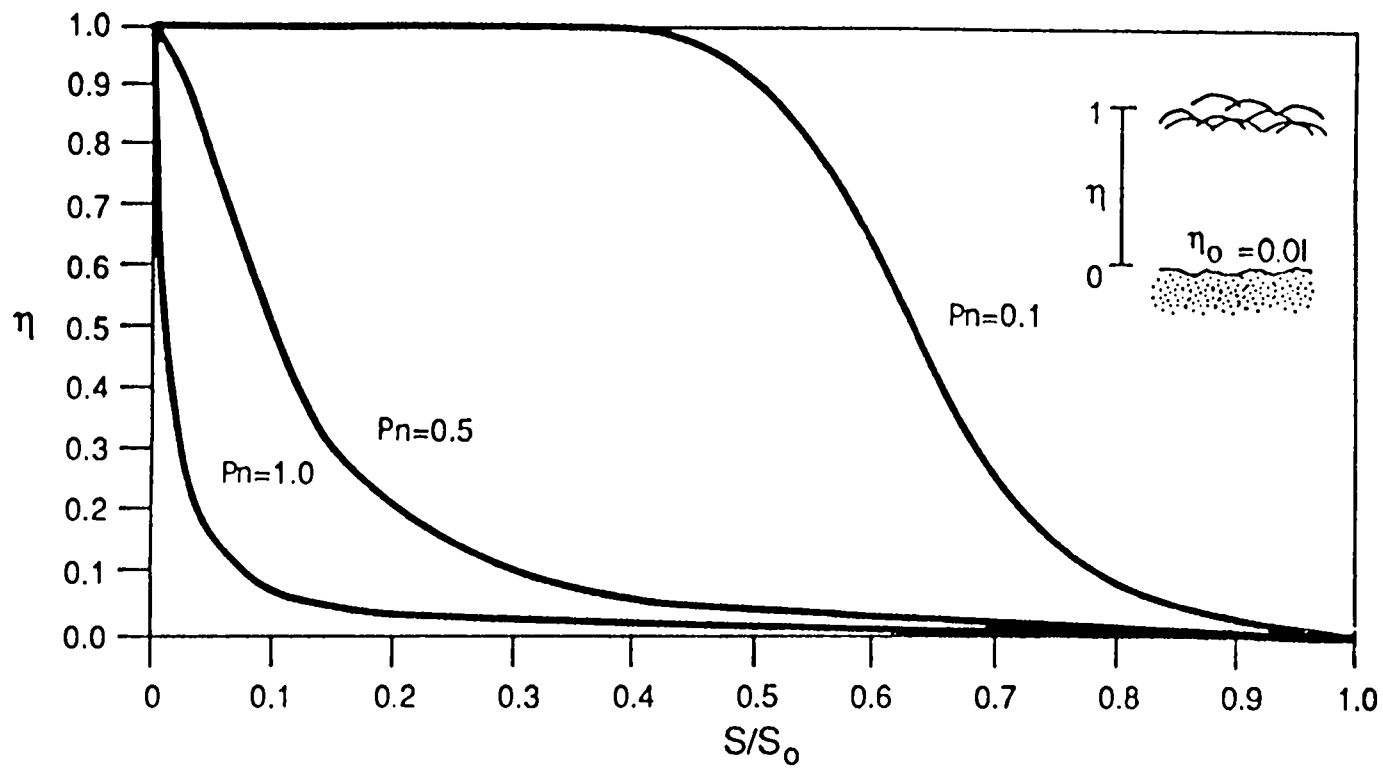
$$\rho = \rho_s S_0 \left[ \frac{\eta_0}{1-\eta_0} \frac{1-\eta}{\eta} \right]^{Pn} \quad (2-5)$$

where  $\rho_s$  is particle density. The density gradient is then

$$\frac{d\rho}{d\eta} = -\rho_s S_0^{Pn} \left[ \frac{\eta_0}{1-\eta_0} \right]^{Pn} \frac{1}{\eta^2} \left[ \frac{1-\eta}{\eta} \right]^{Pn-1} \quad (2-6)$$

A parameter of fundamental importance in stratified flow theory is the Brunt-Vaisala frequency (N) given by (Lin and Pao 1979)

Figure 2-1. Relative concentration ( $S/S_0$ ) as a function of dimensionless height ( $\eta$ ) in a turbulent surge.  $S_0$  is the particle volume concentration of at reference level  $\eta_0 = 0.01$ . Profiles are shown for three values of the distribution Rouse number ( $Pn$ ).



$$N = \frac{1}{2\pi} \left[ \frac{-g}{\rho} \frac{d\rho}{dy} \right]^{1/2} \quad (2-7)$$

where  $g$  is acceleration due to gravity, directed in the negative  $y$  direction.  $N$  represents the maximum possible frequency of internal waves in a stratified flow. Just as waves may occur on a density interface (which represents an infinite density gradient), waves also occur in a continuously stratified flow (Yih 1980). This can be visualized by considering the continuously stratified flow as consisting of an infinite number of very small density interfaces upon which the waves travel. Most stratified flow research has centered on flows with linear density gradients ( $d\rho/dy = \text{constant}$ ) or with density interfaces, which closely approximate atmospheric and ocean currents. As mentioned above, concentration or density stratification in flows dominated by turbulent transport is nonlinear so that the local  $N$  is a function of height in the flow.

Substituting  $\eta$  for  $y$  and applying Equation (2-6), the Brunt-Vaisala frequency profile for a pyroclastic surge becomes

$$N(\eta) = \frac{1}{2\pi} \left[ \frac{g}{d} \frac{Pn}{\eta(1-\eta)} \right]^{1/2} \quad (2-8)$$

Thus  $N$  is not only a function of height in the flow but also depends

on the distribution Rouse number, as shown in Figure 2-2. Note that  $N$  is not a preferred frequency but is the maximum frequency at the specified level in the flow. Internal waves may have any frequency as long as  $N$  is not exceeded.

The Froude number ( $Fr$ ) is of fundamental importance in all flows where inertial and gravitational forces are present. In continuously stratified flows  $Fr$  is defined as

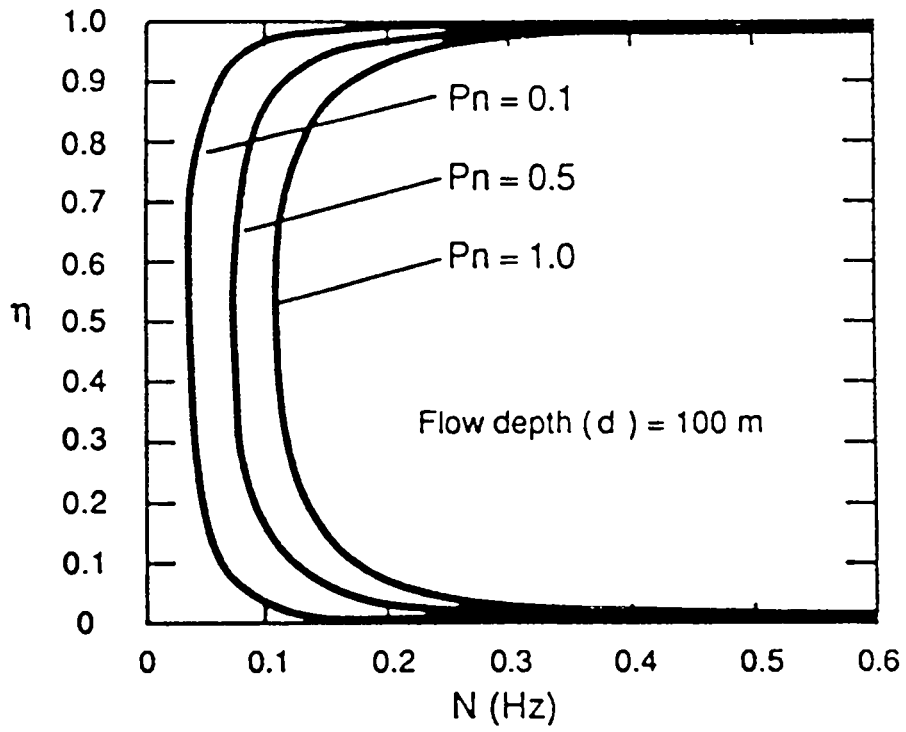
$$Fr = \frac{u}{Ny_h} \quad (2-9)$$

where  $y_h$  is a height scale and  $u$  is flow velocity (Lin and Pao 1979). The height scale can represent either the height of an obstacle in the flow or, in a more general form,

$$y_h = \frac{(\Delta\rho)_s d}{d\rho/d\eta} \quad (2-10)$$

By this definition,  $y_h$  is simply the depth through which a specified density difference  $(\Delta\rho)_s$  occurs. The term  $Ny_h$  represents the speed of internal gravity waves generated at height  $h$ . Thus  $Fr$  can be thought of as a ratio of flow velocity to internal gravity wave speed. In flows with nonlinear  $N$  profiles such as those considered in this chapter,  $Fr$  varies with height even if the flow is inviscid.

Figure 2-2. Example Brunt-Vaisala frequency (N) profiles for a 100 m thick pyroclastic surge at various distribution Rouse numbers (Pn).



One more parameter of importance in stratified flow theory is the Richardson number (Ri). This dimensionless group represents a ratio of "buoyancy" forces to turbulence production, and is given by

$$Ri = \frac{-gd}{\rho} \frac{d\rho/d\eta}{(du/d\eta)^2} \quad (2-11)$$

In a fluid with strong stable density stratification, turbulence is damped because parcels of fluid being moved to different levels by eddies will experience a buoyancy force and tend to return to their original levels. For a boundary layer on a flat plate at zero incidence, if  $Ri > 1/4$ , the flow is stable and turbulence cannot occur no matter how high the Reynolds number (Schlichting 1979, pp. 512-513). For pyroclastic flows and surges, which are density-stratified flows over rough surfaces, the exact critical value of Ri is not clearly defined. The manner in which Ri varies with height in a surge is complex and probably cannot be predicted analytically at present. For example, solving for Ri by applying Equation (2-6) and using the standard relation for a turbulent flow velocity profile yields the result that Ri is at a minimum at the flow boundary, since this is the region of highest shear in the flow. The same solution predicts that the Richardson number increases very rapidly with increasing height. However, observed Ri values in rivers carrying suspended loads, where the same relations should

hold, indicate that  $Ri$  is roughly constant with height above the immediate vicinity of the boundary. Thus, while the effects of variations of the Richardson number can be discussed qualitatively, no attempt is made to analyze it further in this chapter. Wilson (1985) has also discussed the effects of density stratification on turbulence in terms of fluidization-induced density gradients.

The above parameters have been introduced and are used extensively in this chapter because they describe the interplay of forces that affect pyroclastic surges. In the discussion that follows, the emphasis is on how these parameters vary as a surge flows away from its vent or encounters topography. The discussion is largely qualitative and is based on general physical characteristics of turbulent flows. No solutions of the equations of motion are given in terms of the stratified flow parameters. At the current state of knowledge this cannot be achieved because there is as yet no general theory describing turbulent flows.

#### CONDITIONS FOR TURBULENT TRANSPORT

I now consider the conditions necessary for the turbulent transport model used in this chapter. While it is generally agreed that pyroclastic surge deposits such as those found around maars and tuff rings are the product of dominantly turbulent transport, some disagreement has arisen as to whether highly energetic flows, such as the May 18, 1980 blast at Mount St. Helens, can be classified as pyroclastic surges (Walker and McBroom 1983, 1984; Waitt 1984;

Hoblitt and Miller 1984). Because of the importance of this problem with regard to interpreting the deposits, the possibility of turbulent transport at Mount St. Helens is specifically addressed.

It has recently been argued (Walker 1983) that turbulent transport can only be effective relatively near the source of a pyroclastic current, and that the majority of clasts in the current would quickly settle into a highly concentrated basal pyroclastic flow. For instance, in his discussion of the Mount St. Helens blast, Walker (1983) stated that "... the distance of travel (nearly 30 km from vent at Mount St. Helens) is unduly great for a low-concentration cloud moving against air resistance and depending on internal turbulence to maintain particles in suspension.

Sparks et al. (1978) have demonstrated how rapidly particles settle from such a cloud." This argument is based on the modeling of Sparks et al. (1978), but it is questionable whether the Sparks et al. model is applicable to Mount St. Helens. Their model is based on column collapse, where the gas-pyroclast mixture falls to the ground and moves laterally across a rather steep slope near the vent and a gentle slope of  $10^\circ$  beyond that. In addition, they used a roughness of 1 cm and assumed that the entire flow was a boundary layer. These conditions imitate those found around many established ignimbrite-producing volcanoes, but none of them are met for the Mount St. Helens blast. Kieffer (1981) has shown that the laterally moving flow produced by the blast was not due to column collapse, but instead was the result of laterally directed discharge. The

topography around Mount St. Helens is very rugged, characterized by sharp ridges and valleys giving a relief of hundreds of meters. In addition, the blast moved over devastated forest with stumps about 1 m high as roughness elements. The assumption of flow thickness equalling boundary layer thickness that was used by Sparks et al. (1978) is probably incorrect for most cases. At Mount St. Helens, Kieffer and Sturtevant (1986) have reported evidence, based on erosional features thought to be due to boundary layer vortices, that boundary layers in some areas were on the order of 3 - 10 m thick, while the total flow thickness was several hundreds of meters.

In view of the difficulties discussed above in applying the modeling of Sparks et al. (1978), an alternative approach is taken here in order to determine if turbulent transport was important at Mount St. Helens. In these calculations, relevant values of substrate roughness height, boundary layer thickness, free stream velocity, and pyroclast settling velocity were used to calculate particle Rouse numbers for particles with diameters of 0.1, 1, and 10 cm. These are compared to the critical value of the particle Rouse number, which is approximately  $Pn_i = 2.5$  (Middleton and Southard 1978, pp. 6.37-41), above which turbulent suspension is ineffective. The following equation for velocity in a turbulent boundary layer is used (Dingman 1984, pp. 105)

$$u = \frac{u_*}{k} \ln \left( \frac{y}{y_0} \right) \quad (2-12)$$

where  $y_0$  is the roughness parameter. Equation (2-12) is a direct consequence of mixing length theory. For hydraulically rough flow, which is assumed here,

$$\frac{y_0}{k_s} = \frac{1}{30} \quad (2-13)$$

$k_s$  being the actual physical height of roughness elements. Use of (2-13) allows (2-12) to be written as

$$u = \frac{u_*}{k} \ln \left( \frac{30y}{k_s} \right) \quad (2-14)$$

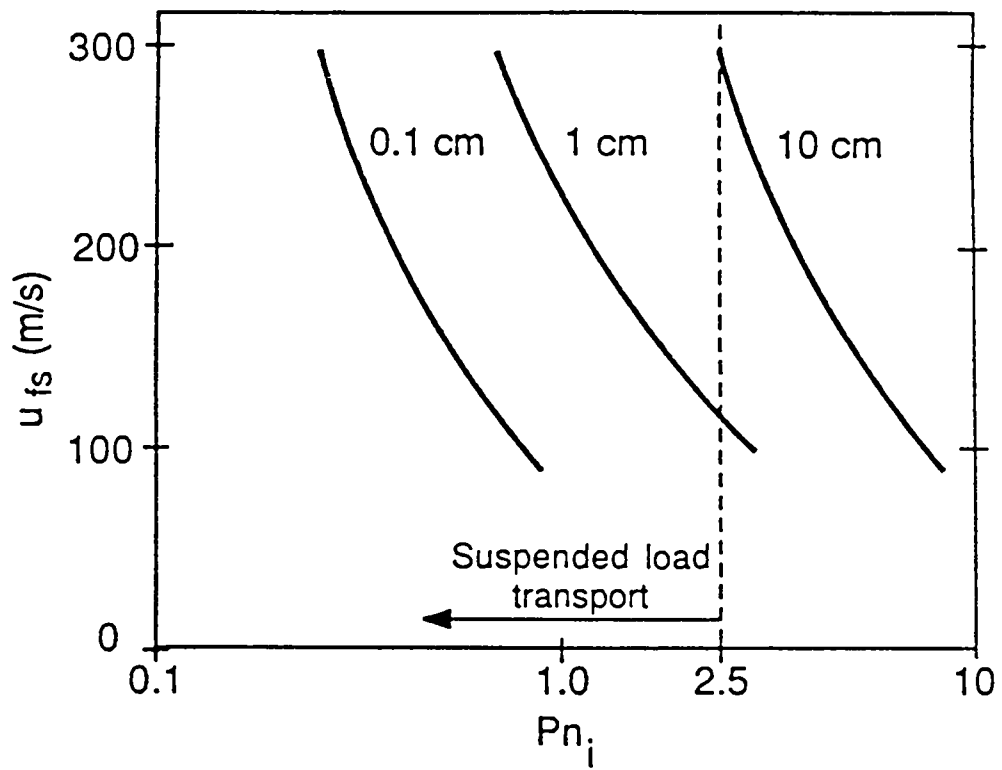
Velocity  $u$  equals the free stream velocity at the top of the boundary layer ( $y = d_{d1}$ ). Using  $d_{d1} = 5$  m and  $k_s = 1$  m,  $u_*$  was determined for velocities ranging from 100 to 300 m/s (this calculation is relatively insensitive to variations of  $d_{b1}$  within the range of values at Mount St. Helens). Particle settling velocities were calculated assuming a particle density of 2000 kg/m<sup>3</sup>

in a dusty gas mixture of steam at 300°C and 1 atmosphere pressure with an average solid volume concentration of about  $4.8 \times 10^{-3}$ , which corresponds to the mass ratio of 25 used by Kieffer (1981). A constant particle drag coefficient of 0.44 was used for settling velocity calculations (Bird et al. 1960, pp. 190-194). Values of  $u^*$  and particle settling velocity  $w_i$  allowed direct calculation of the particle Rouse numbers ( $Pn_i$ ) using Equation (2-1).

Figure 2-3 shows  $Pn_i$  for the three clast sizes given above as a function of free stream velocity  $u_{fs}$ . Pyroclasts with diameters of 1 cm or less are easily transported by turbulence. As  $u_{fs}$  approaches 300 m/s, particles approaching 10 cm diameter are carried in suspension. Model calculations by Kieffer (1981) indicate that flow velocities at Mount St. Helens may have approached 300 m/s, thus it seems likely that large lithic fragments could have been transported by turbulence in the blast. Certainly most ash and fine lapilli-sized clasts could have been easily transported in low-concentration suspension. It is thought that the addition of form drag from larger scale roughness such as avalanche hummocks and from the rough topography would lower all particle Rouse numbers, so that lithic fragments in excess of 10 cm could have been transported by turbulence at velocities much lower than 300 m/s.

On the basis of sediment diffusion experiments in flumes (Jobson and Sayre 1970), Sparks et al. (1978) argue that even in a flow with sufficiently low  $Pn_i$  most sediment will settle out of the flow within distances corresponding to about 10 km in pyroclastic

Figure 2-3. Particle Rouse numbers ( $Pn_i$ ) for lithic clasts with diameters of 0.1, 1, and 10 cm as a function of free stream velocity ( $u_{fs}$ ) for the Mount St. Helens blast. Parameters include roughness height of 1 m, boundary layer thickness of 5 m, clast density of  $2000 \text{ kg m}^{-3}$ , and particle volume concentration of  $4.8 \times 10^{-3}$ . For values of  $Pn_i$  greater than 2.5, turbulent suspension is ineffective. See text for discussion.



systems. However, the flume experiments referred to were aimed at studying longitudinal diffusion in uniform flows. Kieffer (1981) has suggested convincingly that the Mount St. Helens blast was essentially an overpressured jet, so that flow over most of its extent was in the compressible range and was actually supersonic out to about 10 km north of the vent. For nearly half of the extent the flow was accelerating, with velocity increasing from about 105 to 320 m/s according to Kieffer's (1981) model calculations. Therefore, the flow was probably non-uniform, unlike the Jobson and Sayre experiments. As the blast moved across the landscape its suspended-load carrying capacity increased throughout the expansion stage.

Note that relations derived from flume experiments have been heavily used in the present chapter. However, these relations have only been used to derive local conditions in a flow. As stated in the previous section, variables such as the Rouse number and Brunt-Vaisala frequency will change in the flow direction when the flow is not uniform.

Past models for pyroclastic transport processes have been based mainly on gravity as the driving force of the flows. As we have seen at Mount St. Helens, another important driving force arising from the thermodynamics of the flows is supersonic expansion. Most previously studied pyroclastic surge deposits occur around maar volcanos (Moore 1967; Fisher and Waters 1970; Waters and Fisher 1971; Wohletz and Sheridan 1979; Walker 1984). These deposits do

not extend for more than a few km from their sources. They are apparently derived from surges formed by collapse of low phreatomagmatic eruption columns; their source of energy was gravity which dissipated quickly due to drag. Flows dominated by turbulent transport over larger distances (tens of km) may have had a significant component of driving force due to supersonic expansion. The necessarily high initial flow velocity (sonic or supersonic) may be due to collapse from an extremely high eruption column or to overpressured conditions in the column. An overpressured jet need not be laterally directed as was the Mount St. Helens blast. Simple Prandtl-Meyer expansion of a vertical jet as it exits the vent might have the same result. The following question might be asked: Are deposits that suggest turbulent transport over tens of kilometers, such as the Mount St. Helens blast and the Taupo ignimbrite (see discussion below), indications of overpressured eruptions?

#### SURGE BED FORMS

Bed forms such as dunes, ripples, and chute-and-pool structures are very common in pyroclastic surge deposits (Fisher and Waters 1970; Waters and Fisher 1971; Schmincke et al. 1973; Crowe and Fisher 1973; Sparks and Walker 1973; Wohletz and Sheridan 1979). They are similar in many ways to bed forms that occur in water transport systems, but they are commonly lower-angle and more subtle than their water-formed counterparts, except in the deposits of wet surges, where particle-to-bed cohesion is important. Low dips of

foreset and backset laminations in many surge bed forms preclude dune migration by avalanching or rolling of grains down lee-sides (or stoss-sides for antidunes) (Fisher and Schmincke 1984, p. 251). In surges, as in flumes, small-scale ripples may occur on larger bed forms, and dunes may migrate downstream or upstream (here called antidunes, unless the dune can be demonstrated to have moved upstream due to accretion on its wet surface). In some cases ripples migrate downstream even where they occur on antidunes. The precise mechanisms by which bed forms originate in pyroclastic surges are poorly understood.

#### Wavelength Variations

Data indicate that bed form wavelength tends to decrease gradually as flow distance (measured from the vent) increases (Wohletz and Sheridan 1979; Waters and Fisher 1971). In addition, Moore (1967) has documented a rapid decrease in bed form wavelength where pyroclastic surges of the Taal Volcano flowed uphill and decelerated. At Ubehebe volcano in California, Crowe and Fisher (1973) noted that bed form wavelengths increase where substrate dip increases in the direction of flow. Thus the indications are that bed form wavelength is a function of flow velocity or flow power (Fisher and Schmincke 1984, p. 251), although the exact physical link between them is in question. Consideration of stratified flow dynamics holds a possible answer.

As a surge moves across the ground, especially if the ground is relatively smooth like the rim of a maar volcano, turbulence will

become less intense as flow distance increases. This is due to slowing of the flow and the self-dissipative nature of turbulence. The result will be an increasing distribution Rouse number or decreasing carrying capacity of the surge. From Figure 2-1 it can be seen that increasing  $P_n$  implies a steeper density gradient near the bed. Now, dune mechanics in flumes and rivers are tied to waves on the flow surfaces (Kennedy 1963). In pyroclastic surges we have no compelling reason to assume the presence of a density interface, so here I consider the more general case of a continuous stratification. Thus, it is proposed that bed forms in surges are related to internal waves. The horizontal speed of internal gravity wave propagation is equal to  $Ny_h$ ,  $y_h$  being given by Equation (2-10). Minimum possible internal wavelength scales with wave speed divided by maximum (Brunt-Vaisala) frequency, or simply  $y_h$ .  $y_h$  will decrease with decreasing flow velocity due to the steepening density gradient. Thus, the minimum internal wavelength decreases with distance. It is here suggested that bed form wavelength is forced to accommodate the minimum internal wavelength in the near-bed region, and reflects the changes in internal wavelength with flow distance.

The idea of internal waves relating to dune formation may be extended to ripples. Initiation of ripples in sediment transport systems is usually attributed to rather random events. For instance, Richards (1982) states that: "Chance discontinuities in the (viscous) sublayer, with a height ( $h'$ ) of a few grain diameters,

cause flow separation eddies of up to  $100h'$  in length. Sedimentation in these eddies results in incipient ripple formation." This explanation is for the beginning stages of ripple formation, but gives no convincing reason for the periodic nature of ripples. It is suggested that this periodic nature is related to internal waves in the bed load. Transport in bed load is not due to turbulence but to saltation and rolling, and has its own characteristic type of density gradient (not treated here; see Savage 1984). In a pyroclastic surge, it is suggested that large scale bed forms such as dunes and antidunes are related to internal waves in the suspended load (near the bottom but above the bed load) where turbulent transport dominates, and smaller scale ripples are related to internal waves within the thin bed load.

The connection of bed forms with internal waves may have broad applications for other sediment transport systems. For instance, the above explanation of ripple wavelength should hold for water systems as well as pyroclastic surges. Bed forms have long been observed in particulate pipe flows (Kennedy 1963; Thomas 1964) where there is no free surface for waves, thus the bed form periodicity may be attributed to internal waves. Also, bed forms in deep marine environments may be related to internal waves in the density-stratified water (Karl et al. 1986).

#### Migration Direction

Migration direction of bed forms in pyroclastic surges is probably related to whether the near-bed region of the surge is

subcritical or supercritical relative to internal waves, except where governed by cohesion in wet surges. This was briefly addressed by Crowe and Fisher (1973). They proposed that the Froude number criterion for surges probably applies to an internal density interface. However, as discussed in the preceding section, there is no evidence for a density interface. Instead, the relevant Froude number is that given by Equation (2-8). When the near-bed  $Fr < 1$ , downstream migration of bed forms dominates. When  $Fr > 1$ , upstream migration occurs. The transition from supercritical to subcritical flow (hydraulic jump) is probably more complex in a flow with nonlinear but continuous stratification than in one with a density interface, and may occur gradually over a short distance rather than abruptly.

## PYROCLASTIC SURGE FACIES

### Proximal to Distal Facies Changes

Wohletz and Sheridan (1979) defined three pyroclastic surge facies: sandwave, massive, and planar. Sandwave facies occurs proximally and is dominated by sandwave (or wavy) beds with some massive beds. Massive facies includes massive, sandwave, and planar beds and occurs in medial locations. Planar facies is defined by a dominance of planar beds with lesser amounts of massive beds, and is the distal facies. Wohletz and Sheridan (1979) used a deflation/fluidization approach to explain these facies relationships, where solids in a flowing surge become more

concentrated near the base of the surge as it moves away from vent. According to this model, particle support in surges is due to a relative upward movement of gases with respect to particles (fluidization), resulting in a highly expanded, turbulent flow near source that leaves sandwave deposits. As gases escape during lateral transport, degree of fluidization decreases, and eventually deposition occurs only as thin non-turbulent grain flows to produce planar beds. Massive beds, then, result from deposition from flow that is transitional between highly-fluidized turbulent sandwave and non-fluidized, non-turbulent planar flow and deposition. Thus, in the model of Wohletz and Sheridan (1979), surge facies are the result of progressive deflation of the flow with distance.

An alternative view taken here is based on turbulent transport in a stratified flow. When a surge is initiated at the vent, it has a high velocity owing to kinetic energy gained by column collapse, blast waves (Wohletz et al. 1984), and other near-vent processes. This produces a low Rouse number (Equation (2-2)) which increases with flow distance, giving rise to an increasing near-bed density gradient with distance (Figure 2-1). Now consider the Richardson number given by Equation (2-9). As a pyroclastic surge moves away from the vent, increasing density gradient and decreasing inertial forces will produce an increase in  $Ri$  near the bed and damping of turbulence. Thus, it is possible to explain the surge facies changes observed by Wohletz and Sheridan (1979) in terms of a progressively increasing density (grain concentration) gradient at

the base of a surge (Fisher and Schmincke 1984, p. 256). Proximal locations have relatively low  $P_n$  and  $R_i$ , and thus are highly turbulent and deposit a wavy, thin bed load. It is in this region where bed form processes discussed in the previous section are most likely. In medial locations, the flows are more stratified at the bottom and less turbulent, forming massive beds. In distal regions, nearly all the remaining particle load is at the base and there is a very strong density stratification. Non-turbulent grain flow (Bagnold 1956; Savage 1984; Wohletz and Sheridan 1979) dominates here, producing reversely graded planar beds.

Note that the process of increasing particle concentration near the base of a surge is, in a way, analogous to the deflation process of Wohletz and Sheridan (1979). However, the mechanisms for increasing basal concentration are different. In the model presented here, increasing basal concentration is the result of a decreasing capability of the surge to carry its load by turbulent transport. In the model presented by Wohletz and Sheridan (1979), increasing basal concentration is due to progressive loss of fluidizing gases. Both processes probably occur, but as presented here, turbulence, rather than fluidization, is the dominant transport mechanism in surges.

#### Facies Variations due to Topography

A common feature of pyroclastic surge deposits is that they are thicker in topographically low areas than on high areas (Wohletz and Sheridan 1979; Fisher and Heiken 1982; Fisher et al. 1987), and

commonly show local facies variations due to topography which are overprinted on proximal to distal variations discussed above. This topographically controlled property of surges is evidence for their density-stratified nature. Do the following thought experiment: follow a parcel of fluid along its streamline in a non-stratified flow. When the fluid parcel impinges upon a topographic obstacle, say a hill, it will move up and over the hill, assuming that the hill is infinite along the horizontal axis perpendicular to flow. Now consider the same parcel, but in a stably stratified fluid (see Figure 2-4). When the parcel encounters the hill, the up-and-over motion will be retarded because this requires that the parcel moves into regions of lower density than itself. For the parcel to surmount the hill it must have enough kinetic energy upstream of the hill to counteract the negative buoyancy. For a given stratified flow encountering an obstacle, there will be a level (streamline) above which all fluid has sufficient energy to top the obstacle and below which all fluid either is stopped (blocked) or simply moves around the obstacle with no upward motion (Figure 2-4). This critical level is referred to as the "dividing streamline." The relationship between upstream kinetic energy, density gradient, and height ( $y_{ds}$ ) of the dividing streamline was due originally to Sheppard (1956) and was discussed and tested by Snyder et al. (1985). It is:

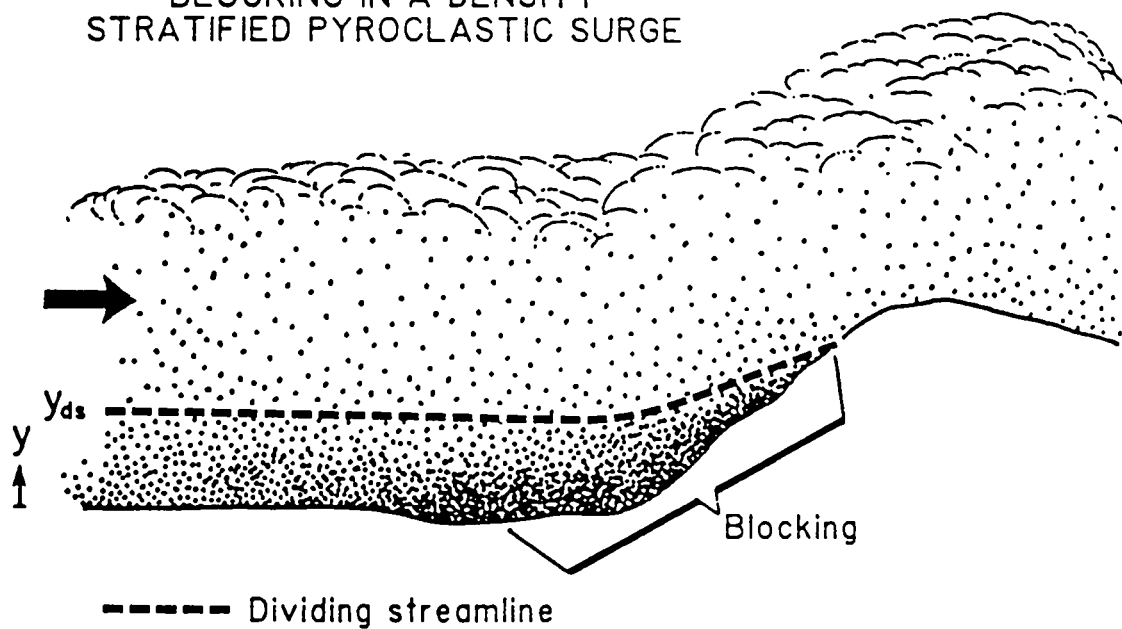
$$\left(\frac{1}{2}\rho u_{\infty}^2\right)_{y_{ds}} = g \int_{y_{ds}}^{y_m} (y_{ds}-y) \left[\frac{-d\rho}{dy}\right] dy \quad (2-15)$$

Here, the left-hand side is simply the kinetic energy of a fluid parcel at the level  $y_{ds}$  far upstream of the obstacle. The right-hand side is potential energy gained by hill overtopping,  $y_m$  being defined here as the hill height. Although this equation does not take into account viscous effects and other flow complexities, it has been very successful in predicting  $y_{ds}$  in laboratory experiments with low Froude numbers, as shown by Snyder et al. (1985). Equation (2-15) should not be extended quantitatively to pyroclastic surges without experimental evidence supporting its applicability, because it has only been tested on low Froude number flows with linear density gradients. As discussed earlier, for turbulent transport systems such as surges, the Brunt-Vaisala frequency is a function of height and leads to a wide range of Fr within the flow. However, the dividing streamline concept is useful for visualizing flow behavior relative to topography. Note that the process of blocking does not require that the flow be thicker than the height of the obstacle. It only requires that the flow be internally stratified.

The degree of thickening in topographic lows reflects two types of processes. The first is the result of a substrate where long axes of low areas are roughly parallel to flow direction. In this

Figure 2-4. Blocking in a stratified pyroclastic surge as it encounters a hill. The dashed line indicates the position of the dividing streamline, which occurs at height  $y_{ds}$  (see Equation 2-15). Below  $y_{ds}$ , material cannot flow over the obstacle and must either stop or flow around it. In a pyroclastic surge, this may lead to thick, massive deposits in topographic lows.

BLOCKING IN A DENSITY  
STRATIFIED PYROCLASTIC SURGE



case, deposits on highs are thinner essentially because they formed at levels above the maximum-concentration lower parts of the flow. In some cases it may be possible to have massive facies in lows and sandwave facies on highs due to much higher particle concentration near the base of the flow. The extreme example of this is a surge moving down a deep canyon, where increasing Rouse number causes lower parts to become dense enough to take on characteristics of a pyroclastic flow (gravity transformation; Fisher 1983) while the upper parts leave deposits more typical of surges (e.g., the 1902 eruptions of Mt. Pelee; Fisher and Heiken 1982).

The second thickening process occurs where surges encounter ridges or valleys with long axes at high angles to flow direction. Material below the dividing streamline is "blocked," and must either stop or flow around the obstacle while staying at a constant level. It is easy to visualize how this might lead to a thick deposit at the base of such obstacles. A possible example of blocking is the occurrence of secondary pyroclastic flows in deposits of the May 18, 1980 blast at Mount St. Helens (Hoblitt et al. 1981; Fisher et al. 1987). Apparently, as the blast moved across the South Coldwater Creek valley, dense pyroclastic flows formed and moved down the valley almost at right angles to the flow direction of the main blast, a scenario that can be explained by blocking. Druitt and Bacon (1986) have also discussed this process and its effects on lithic breccia deposition during the ignimbrite-forming eruptions at Crater Lake, Oregon.

### The Low-Aspect-Ratio Ignimbrite Problem

A subject of recent controversy in pyroclastic geology has been the interpretation of deposits as surges by some workers (e.g. Fisher and Heiken 1982; Fisher et al. 1987) and as low-aspect-ratio ignimbrites (LARI) by others (Walker and McBroom 1983; Walker 1983). The main difference between the interpretations is that pyroclastic surges are thought of as low-concentration currents where turbulent transport dominates, as discussed above, whereas pyroclastic flows that produce LARI's are considered to be high-velocity, high-concentration currents where turbulence occurs but is not the principal particle support mechanism. Because of the significance of this problem for understanding flow and deposition mechanisms of pyroclastic systems, it is addressed here in terms of stratified flow processes.

The two best studied deposits that fit into the category of LARI are the Taupo ignimbrite (Wilson 1985) and the deposit of the May 18, 1980 Mount St. Helens (MSH) blast (Waite 1981; Hoblitt et al. 1981; Fisher et al. 1987). While these two deposits differ in the details of their stratigraphy, they show broad similarities. Table 2-1 lists the general characteristics of the deposits, including terminology used for their stratigraphy. This listing is by no means comprehensive, and the reader is directed to the references given with Table 2-1 for more detailed descriptions and granulometric data. The overall characteristics of the Taupo ignimbrite and the MSH deposit can be summarized as follows. The

lowest parts of the deposits consist of coarse (relative to overlying layers) bottom layers which occur throughout most of the lateral extents, being thicker in topographic lows than on highs. The coarse bottom layers are overlain by landscape mantling veneer deposits which are bedded and commonly cross bedded. In valleys the mantling deposit grades laterally into thicker, massive, valley filling deposits. The valley filling deposits have flat tops and characteristics of pyroclastic flow deposits sensu stricto (Sparks 1976).

Wilson and Walker (1982) proposed a model for the development of the various facies of the Taupo ignimbrite. In their model, coarse bottom layers are formed by explosive jetting of material from the front of a pyroclastic flow (layer 1(P)) and sedimenting of heavy particles from the head (layer 1(L)). Valley fill facies (valley-ponded ignimbrite, VPI) represents deposition from the body of the flow, and the tail of the flow leaves the mantling veneer deposit (IVD). Wilson (1985) expanded this model to account for lateral variations in the Taupo deposit by considering the flow to be a giant fluidized bed. In this model, easier fluidized material such as low-density pumice and pumiceous ash are carried higher in the flow and deposited furthest from the vent. Wilson (1985) also discussed the density stratification that would be produced by the fluidized bed scenario, and suggested that this would effectively damp turbulence.

Table 2-1: Summary of Characteristics of Taupo Ignimbrite and 18 May 1980 Mount St. Helens Blast Deposit

Deposit	Flow Velocities	Coarse Bottom Layers	Landscape-Mantling Upper Layers	Valley-Filling Upper Layers
Taupo <sup>1</sup>	c. 150 m/s, possibly up to 300 m/s	<p>Layer 1(P) - pumiceous deposits, massive, local fluidization textures.</p> <p>Fines-depleted Ignimbrite (FDI) - pumiceous, low fines (&lt;1/8 mm) content relative to other 1(P) deposits.</p> <p>Layer 1(H) - Lithic and crystal deposits. Overlies 1(P) in most places.</p>	<p>Ignimbrite veneer deposit (IVD) - bedded, grades laterally into VPI. Cross bedded within 25 km of vent and in lee of obstacles. Crystal, lithic contents and pumice density follow trends of VPI with distance. Contains less coarse material than VPI. Only locally fines-depleted.</p>	<p>Valley pond ignimbrite (VPI) - massive, thickness depending on dimensions of valleys and distance from vent. Commonly has poorly developed layer 2a. Above 2a lithics are normally graded, pumices reversely graded to form pumice concentration zones at top. Fines content increases and pumice density decreases with increasing distance from vent.</p>
Mount St. Helens <sup>2</sup>	100-300 m/s	<p>Layer A0 - massive or exhibiting sheared textures. Mixture of substrate material and juvenile dacite. Note: A0 is not coarse relative to other layers in all places.</p> <p>Layer A1 - coarse, fines-depleted blocks and lapilli to coarse ash. Massive. Poorly sorted relative to layer A2.</p>	<p>Ridge-top facies of layer A2 - thinner, finer grained than valley-fill facies. Commonly is laminated and cross bedded in its upper part, although lower part is massive.</p>	<p>Valley-fill facies of layer A2 - thicker, coarse grained than ridge-top equivalent. Massive throughout its thickness.</p> <p>Layer A2* - secondary blast-flow deposits. Formed from flowback of fluidized material from slopes into valleys.</p>

<sup>1</sup> Wilson (1985), Walker and Wilson (1983), Walker et al. (1981a,b).

<sup>2</sup> Fisher et al. (1987), Kieffer (1981), personal observation.

On the other hand, Fisher et al. (1987) attributed the MSH deposits to deposition from an expanded, turbulent surge. They also ascribed certain layers to specific parts of the flow, suggesting that the coarse bottom layer is deposited from the back of the head region. The landscape mantling and valley filling upper deposits were both attributed to the body of the flow. The Fisher et al. model draws direct analogy with known dynamics of turbidity currents.

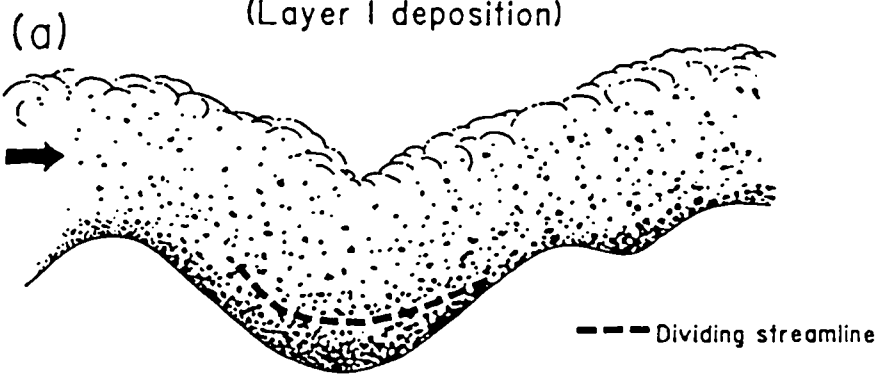
A new model is proposed here for the development of deposits with the above characteristics. This model explains only the broad relationships of the various facies. It is thought that detailed characteristics of individual deposits can be explained in terms of the general framework of this model, taking into account the unique conditions of each eruption. The model combines ideas of Wilson (1985) and Fisher et al. (1987). The flow is stratified according to particle settling velocity as in the Wilson model, but, as in the Fisher et al. model, the stratification is due to turbulent transport instead of fluidization. The likelihood of turbulent transport for most observed particle sizes has already been addressed for the MSH blast. While the Taupo ignimbrite is much more extensive than the MSH deposit, conditions such as rugged topography and high-speed flow (estimated velocities for the Taupo flow are given in Table 2-1) were similar for the two events. In addition, most of the far-travelled material at Taupo is pumiceous (Wilson, 1985), and has much lower settling velocities than the

dense lithic fragments transported by the MSH blast (Figure 2-3). The new model differs from both the Wilson and Fisher et al. models in that the geometry of a flow (head, body, tail) plays no role in developing the stratigraphy. Instead, lateral changes in deposition are related to the interactions of the turbulent stratified flow with topography and to velocity variations due to distance from vent. Vertical changes in deposition are due to time evolution of the supply rate and type of material to the flow.

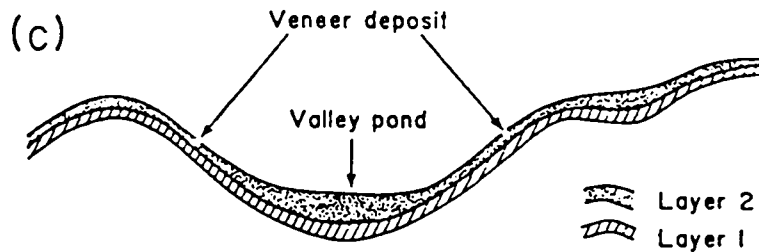
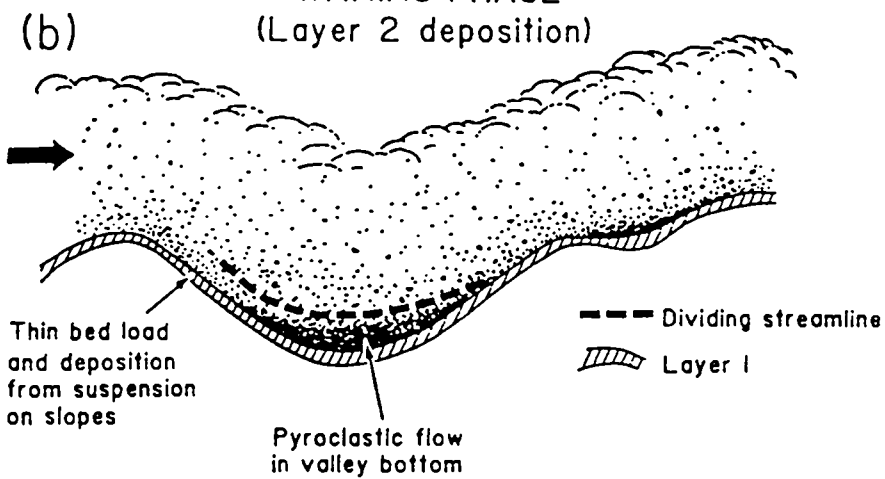
The model is shown diagrammatically in Figure 2-5. Coarse bottom layers, called layer 1, are deposited from suspended load during the high energy waxing phase of the flow event (Figure 2-5a). Blocking occurs in topographic lows to produce thicker deposits there. As the supply rate of material to the flow begins to decrease (e.i., eruption discharge decreases), remaining particles with lower settling velocities fall out of suspension (Figure 2-5b). This material may move along the bed as traction carpet or as dense, small scale flows to produce stratified and cross stratified layer 2 veneer deposits that mantle the landscape. Cross stratification in the veneer deposit is due to bed form processes discussed earlier. This type of deposition is typical of more conventional pyroclastic surges such as those found around tuff rings. In support of this at Taupo is the fact that cross stratification in the veneer deposit (other than that induced by topography) is found only within about 25 km from the vent (Walker et al. 1981b; Wilson 1985), which may correspond to the proximal sandwave facies of Wohletz and Sheridan

Figure 2-5. Diagrammatic illustration of the sequence of events leading to a deposit consisting of coarse bottom layers (layer 1) overlain by layer 2, which has a landscape-mantling veneer facies and a thick, massive valley pond facies. The model assumes turbulent transport and resulting stratification. (a) Layer 1 is deposited during the high-energy waxing phase of the flow. Deposits are thicker in valleys due to blocking below the dividing streamline. During this phase most deposition is directly from suspension. (b) Layer 2 is deposited as remaining low-settling-velocity material falls out of the waning flow. Bed-load movement may produce stratification, and bed-form processes discussed in the text produce cross-bedding in the veneer deposit. Blocking continues in topographic lows, resulting in local pyroclastic flows with reversely graded bases, pumice concentration zones on their tops, and other features commonly seen in pyroclastic flow deposits. (c) The final product of the above processes.

WAXING PHASE  
(Layer 1 deposition)



WANING PHASE  
(Layer 2 deposition)



(1979) discussed earlier in this chapter. Also during the waning phase, material is blocked in valleys to form thick, massive layer 2 deposits. Note that while material in the valley ponds may have moved as pyroclastic flows within individual valleys, particles were transported from the vent to the valleys by turbulence. This contrasts with the model of Wilson and Walker (1982).

Note that in this model fluidization textures such as fines-depleted pipes and patches (Wilson 1985) are formed mainly after deposition or during the very final stages of deflation of a deposit. One objection that may be raised to this model is that the deposits are too poorly sorted to have been formed from a low concentration suspension. However, it is not clear that deposition from suspended load would lead to good sorting. For example, recent experiments by Ghosh et al. (1986) suggest that the sorting of such deposits may closely reflect the sorting of the actual suspended load.

#### SUMMARY

The results of this study are summarized below.

1. Turbulent suspension transport is likely for many pyroclastic currents, including the May 18, 1980 blast at Mount St. Helens. This is especially true if the flows are initiated at sonic or supersonic velocities.

2. Surge bed forms may be related to internal waves. Decreasing bed form wavelength with flow distance reflects a similar

relation between minimum wavelength of internal waves and the distribution Rouse number. Dunes and ripples are related to internal waves in the bottom of the suspended load and in the bed load, respectively. Bed form migration direction is related to the internal Froude number.

3. The proximal to distal facies progression described by Wohletz and Sheridan (1979) can be explained in terms of changing density stratification with flow distance. Namely, the increasing Richardson number with flow distance results in progressive damping of near-bed turbulence.

4. Surge deposits in topographic lows may be thicker and more massive than on topographic highs, reflecting two processes. The first occurs when the long axis of relief is at low angles to the flow direction. In this case, relatively thick and massive deposits form in depressions because the particle concentration higher there. Second, when the long axis of relief is at high angles to the flow direction, blocking of denser material may produce massive pyroclastic flows that move down slope, possibly independent of the overall flow direction of the overriding surge.

5. Deposits which have been termed both "pyroclastic surge" and "low-aspect-ratio ignimbrite," such as at Mount St. Helens and Taupo, can be explained by a general model incorporating turbulent transport, stratified flow, and time evolution of the eruptive events. Coarse bottom deposits represent deposition from suspended load during the initial high-energy (waxing) phase of the eruption.

Finer-grained and bedded upper layers represent deposition of remaining fine material as the eruptive event wanes. Massive valley deposits are due to blocking.

APPENDIX 2A: DEFINITION OF NOTATION FOR CHAPTER 2

---

Symbol	Definition	Dimensions
d	Total flow thickness	L
d <sub>b</sub>	Boundary layer thickness	L
Fr	Froude number	--
g	Gravitational acceleration	LT <sup>-2</sup>
k	Von Karman constant (=0.4)	--
k <sub>s</sub>	Height of roughness element	L
N	Brunt-Vaisala frequency	T <sup>-1</sup>
P <sub>n</sub>	Distribution Rouse number	--
P <sub>nj</sub>	Particle Rouse number	--
Ri	Richardson number	--
S	Particle volume concentration	--

---

$S_{avg}$	Average particle vol. fraction	--
$S_i$	Volume concentration of particles with settling velocity $w_i$	--
$S_0$	Particle volume fraction at $\eta_0$	--
$u$	Flow velocity	LT-1
$u_{fs}$	Free stream velocity	LT-1
$u^*$	Shear velocity	LT-1
$u_\infty$	Velocity upstream of obstacle	LT-1
$w_i$	Settling velocity class $i$	LT-1
$y$	Vertical axis, height	L
$y_{ds}$	Height of dividing streamline	L
$y_h$	Height scale	L
$y_m$	Hill or obstacle height	L
$y_0$	Roughness parameter	L

$\eta$	Dimensionless height $y/d$	--
$\eta_0$	Dimensionless reference level	--
$\rho$	Surge bulk density	ML <sup>-3</sup>
$\rho_s$	Particle material density	ML <sup>-3</sup>
$(\Delta\rho)_s$	Specified density difference	ML <sup>-3</sup>

---

CHAPTER 3: NUMERICAL MODELS OF PLINIAN ERUPTION  
COLUMNS AND PYROCLASTIC FLOWS

INTRODUCTION

This chapter reports a second step in application of numerical solution of the time-dependent, nonlinear, multiphase hydrodynamics equations to explosive volcanic phenomena associated with Plinian eruptions. The first step is presented in the paper by Wohletz et al. (1984), which outlines an overall evolution of caldera-related eruptions. In this evolutionary sequence, a dike of volatile-rich magma is catastrophically exposed to the atmosphere, producing an initial phase of unsteady flow characterized by shocks propagating into the atmosphere and rarefactions propagating down the conduit. This initial phase, during which ash is driven out of the vent and laterally across the landscape largely by the pressure fluctuations associated with blast waves, has been discussed in reference to the Peach Springs Tuff eruption in Chapter 1. The blasting phase eventually comes to an end with the development of steady discharge from the vent, which is characterized by the development of ash plumes and pyroclastic flows. This chapter is devoted to modeling the first few minutes of steady discharge.

To develop perspective for the model results, previous modeling of steady eruption columns is briefly reviewed. Description of the hydrodynamics equations used in the models is followed by analysis of the 51 numerical experiments. Dimensionless ratios are used to

analyze the effects of various forces on eruption dynamics. Finally, I discuss implications of the modeling for development of pyroclastic flows and associated depositional facies variations.

#### Previous Modeling

Modeling of explosive volcanic eruptions has become popular over the past twenty years with development of quantitative field techniques for the study of pyroclastic deposits. The fact that most large eruptions have not been witnessed and recorded has spurred modeling efforts to obtain an understanding of eruption processes responsible for various types of tephra deposits. With respect to Plinian eruptions most modeling has been based upon entrainment theory of turbulent jets and plumes. In the first treatment of columns using this approach, Wilson (1976) uses a single-phase, incompressible, turbulent jet model from Prandtl (1949) with modifications to account for gravity and thermal effects of entrained particles. Wilson's treatment solves the equations for conservation of mass and momentum involving Prandtl's empirical relations for the rate of entrainment of ambient air (reflected in the assumed rate of widening of the jet with height). This approach assumes that pressure in the column at any given elevation is in perfect equilibrium with the ambient pressure. Sparks and Wilson (1976) and Sparks et al. (1978) extended the turbulent plume treatment to include the conditions under which entrainment of ambient air, which produces buoyancy in a column, is not sufficient

to thrust the column higher by convection, and the column collapses at the top of the gas thrust (jet) region to form pyroclastic flows.

In an effort to quantify the dynamics of Plinian eruption columns in the convective thrust region, which comprises most of the height of Plinian column, Settle (1978) and Wilson et al. (1978) apply the empirical formula of Morton et al. (1956) for incompressible, convective plumes. This approach involves a power law relationship between mass discharge rate and eruption column height, namely  $H \propto D^{1/4}$ , where  $H$  is the height of the column top and  $D$  is the mass discharge rate of magma. Jakosky (1986) raises some questions about this relation, suggesting that it may be somewhat fortuitous due to the simplifications involving the atmospheric lapse rate and the use of the visible cloud top instead of the mass-averaged cloud top for the value of  $H$ . Sparks and Wilson (1982) apply the same type of incompressible turbulent plume theory to the 1979 eruptions of Soufriere, using an empirical entrainment constant (similar to a mixing length). This approach is extended by Wilson and Walker (1987), who account for atmospheric wind, and applied to tephra dispersal. Sparks (1986) refines the theory of eruption plumes within the framework of turbulent, incompressible convection, and includes climatic effects. Carey and Sparks (1986) apply the refined theory to tephra dispersal.

The May 18, 1980 blast at Mount St. Helens brought attention to the importance of compressible fluid dynamic processes in volcanic jets. With this focus, Kieffer (1981) applied experimentally

observed jet dynamics to that eruption, and discussed the effects of exit pressures that exceed local ambient pressure. The jet is then characterized by complex patterns of rarefaction waves and shocks. To further this concept, Kieffer and Sturtevant (1984) present results of laboratory experiments on single phase (one material) jets that are thermodynamically similar to multiphase volcanic products within a single-phase (pseudogas) approximation scheme. These experiments provide important insight into effects of jet exit pressure and mixture density.

In summary, previous work on eruption columns consists of two general approaches. The first is to model the effects of turbulence and gravity but to neglect the thermodynamics of the flows. The second is to examine the thermodynamics of the flows but neglect turbulence and gravity. Also, both approaches have essentially considered the flows as single-phase fluids with properties modified by the presence of particles. In an effort to close the gap between the two approaches, I have modeled the compressible, two-phase flow in a gravitational field. Although a crude approximation of turbulence effects is included, this approach does not strictly model turbulence and related diffusive processes. This next step awaits development of a theory of turbulent, two-phase, compressible flow.

The modeling effort reported here has been continued with the opinion that use of empirical entrainment theory, derived from incompressible flow experiments, is problematic and may be

misleading. This problem is due to the strong dependence of mixing upon Mach number in shear flows -- namely that entrainment rates decrease substantially with increasing Mach number (Brown and Roshko 1974). Basic similarity considerations show that it is not satisfactory to model volcanic eruption columns as incompressible flows either theoretically or in the laboratory. Column velocities of several hundreds of meters per second are typical of Plinian eruptions. Kieffer and Sturtevant (1984) show that with moderate solid particle concentrations, the sound speeds of the eruptive mixtures are less than several hundred meters per second. So, in general, the Mach number effect should not be neglected and the full conservation of energy equation must be solved along with continuity and conservation of momentum to make a reasonable model.

## THEORETICAL APPROACH

### Governing Equations

A comprehensive review of mathematical and numerical techniques for multiphase flow is given by Stewart and Wendroff (1984). The approach taken here is to solve the full set of two-phase, compressible Navier-Stokes equations for injection of a hot, particle-laden gas into a cool, density-stratified atmosphere. The geometry of the problem is shown in Figure 3-1. Each phase is modeled as a continuum, one being compressible (gas phase) and the other incompressible (solid phase), using the formulation given by

Harlow and Amsden (1975). In this situation the governing equations in vector form are:

$$\frac{\partial}{\partial t}(\theta_s \rho_s) + \vec{\nabla} \cdot (\theta_s \rho_s \vec{u}_s) = 0 \quad (3-1a)$$

$$\frac{\partial}{\partial t}(\theta_g \rho_g) + \vec{\nabla} \cdot (\theta_g \rho_g \vec{u}_g) = 0 \quad (3-1b)$$

$$\begin{aligned} \frac{\partial}{\partial t}(\theta_s \rho_s \vec{u}_s) + \vec{\nabla} \cdot (\theta_s \rho_s \vec{u}_s \vec{u}_s) = & -\theta_s \vec{\nabla} p + K_s (\Delta \vec{u}) \\ & + \theta_s \rho_s \vec{g} - \vec{\nabla} \cdot \tau_s \end{aligned} \quad (3-2a)$$

$$\begin{aligned} \frac{\partial}{\partial t}(\theta_g \rho_g \vec{u}_g) + \vec{\nabla} \cdot (\theta_g \rho_g \vec{u}_g \vec{u}_g) = & -\theta_g \vec{\nabla} p + K_g (\Delta \vec{u}) \\ & + \theta_g \rho_g \vec{g} - \vec{\nabla} \cdot \tau_g \end{aligned} \quad (3-2b)$$

$$\theta_s \rho_s \left[ \frac{\partial I_s}{\partial t} + \vec{\nabla} \cdot (I_s \vec{u}_s) - I_s \vec{\nabla} \cdot \vec{u}_s \right] = R_s - \tau_s : \vec{\nabla} \vec{u}_s \quad (3-3a)$$

$$\begin{aligned} \theta_g \rho_g \left[ \frac{\partial I_g}{\partial t} + \vec{\nabla} \cdot (I_g \vec{u}_g) - I_g \vec{\nabla} \cdot \vec{u}_g \right] = & -p \vec{\nabla} \cdot (\theta_g \vec{u}_g + \theta_s \vec{u}_s) + R_g \\ & + |K_g| (\Delta \vec{u})^2 - \tau_g : \vec{\nabla} \vec{u}_g \end{aligned} \quad (3-3b)$$

Subscripts s and g refer to the solid (pyroclast) and gas phases of the flow, respectively.  $\theta$  is volume fraction of a given phase,  $\rho$  is

the material density,  $\vec{u}$  is velocity,  $p$  is the pressure of the gas phase,  $K$  is the momentum transfer (drag) function,  $\vec{g}$  is the gravitational acceleration,  $\tau$  is the viscous stress tensor,  $I$  is specific internal energy, and  $R$  is the interphase heat transfer. Finally,  $\Delta\vec{u}$ , the slip velocity, is given by  $\Delta\vec{u} = \vec{u}_g - \vec{u}_s$ . All symbols and their definitions are listed in Appendix 3A.

Equations 3-1a,b are conservation of mass for the solid and gas phase, respectively. Equations 3-2a,b are conservation of momentum. In Equation 3-2a, note that the pressure term represents the accelerating force on the particle phase due to the gas pressure gradient. Since the pyroclasts are assumed to be dispersed, with negligible particle-particle interactions, a pressure for the solid phase vanishes. For both phases, conservation of specific internal energy (Equations 3-3a,b) includes effects of interphase heat transfer and viscous dissipation. In addition to these, the specific internal energy of the gas phase is influenced by pressure work and energy produced by interphase drag. The numerical approximation of these equations is discussed in Appendix 3D.

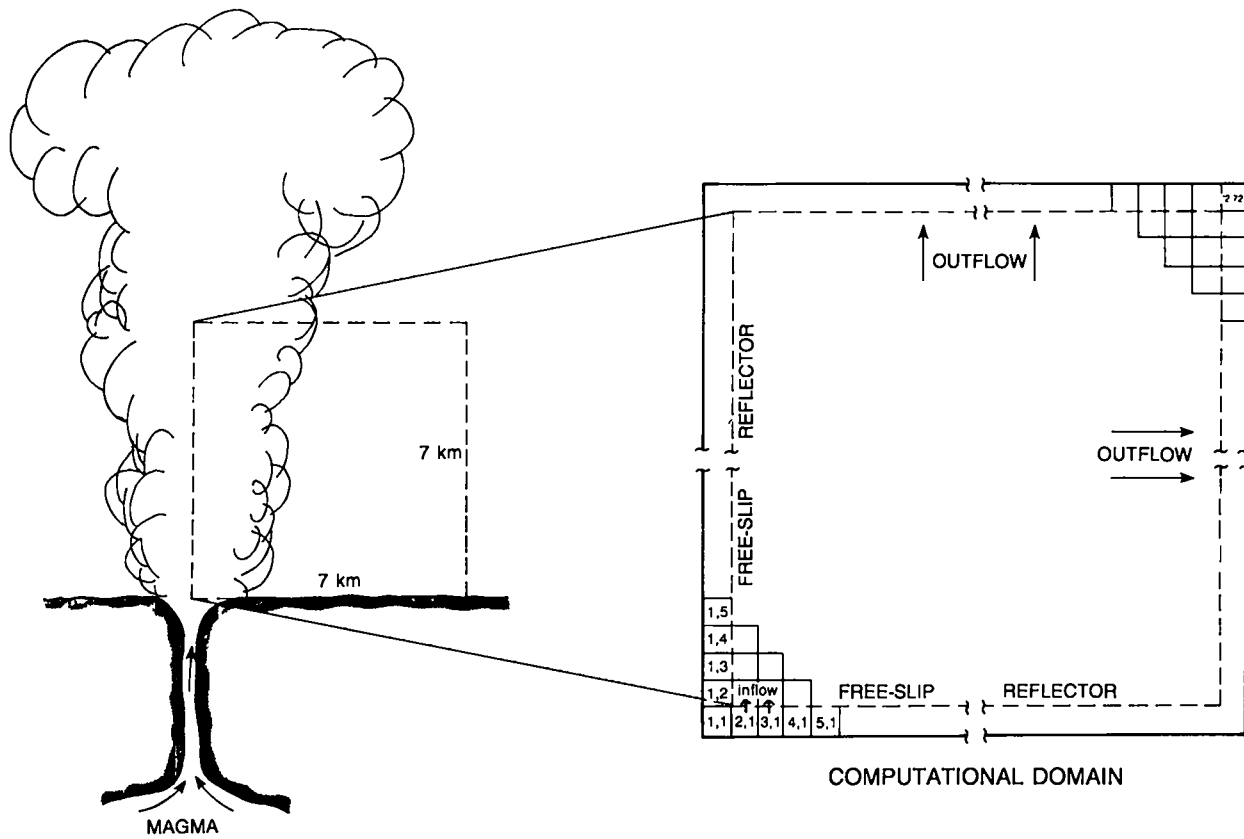
Equations 3-1,2,3 are very similar to those applied to the blast phase of explosive eruptions by Wohletz et al. (1984), with the exception of terms involving heat conduction within the gas phase and viscous effects. Appendix 3E summarizes scaling arguments that show intraphase heat conduction to be minor compared to other forms of energy transfer in Equations 3-3a,b. Building upon the

modeling of Wohletz et al. (1984) a stress tensor is included in the momentum and energy equations, taking the form

$$\tau = -\theta\rho\nu \begin{bmatrix} 2 \frac{\partial u}{\partial r} & 0 & \left[ \frac{\partial v}{\partial r} + \frac{\partial u}{\partial z} \right] \\ 0 & 2 \frac{u}{r} & 0 \\ \left[ \frac{\partial v}{\partial r} + \frac{\partial u}{\partial z} \right] & 0 & 2 \frac{\partial v}{\partial z} \end{bmatrix} \quad (3-4)$$

This expression is appropriate for two-dimensional cylindrical coordinates,  $r$  being the radial distance from the symmetry axis and  $z$  being vertical distance above the vent exit plane (simplified from Bird et al. 1960, p. 89). Because the Reynolds number for these flows is very large ( $\sim 10^{10}$  or larger, see Appendix 3E), the contribution of stress from "molecular" viscosity (which is influenced by the presence of particles) is negligible. However, such high Reynolds numbers indicate that turbulence is likely in the flows, in which case it is necessary to consider turbulence-induced diffusion of transport quantities (mass, momentum, and energy). As stated earlier a detailed model of compressible, multiphase turbulence has not been developed, so as a crude approximation a mixing-length approach has been used to determine effective turbulence viscosity. This approach is useful in many cases (see, for example, Chapter 2 and Valentine 1987), but can be dangerous if care is not used, since it relies on an analogy between turbulent

Figure 3-1: Geometry of problem and the computational domain. The flow field is computed for a 7 x 7 km area above and laterally away from the vent, with the computational domain discretized into 100 x 100 m cells (toroids in three dimensions, since a cylindrical geometry is assumed) for finite-difference approximation of Equations 3-1,2,3. The outer "frame" of cells are used for specification of boundary conditions. See text for discussion.



transport and molecular transport as determined by kinetic theory (see discussion by Tennekes and Lumley 1972, pp. 8-14, 57). In light of this analogy, I have chosen only to model what is likely to be a reasonable minimum turbulence viscosity so that

$$\nu = 0.2L |\vec{u}| \quad , \quad (3-5)$$

where the length scale,  $L$ , is set at 100 m, the mesh size in the numerical solutions. Equation 3-5 is appropriate for a mean eddy diameter in the turbulent flow of about 20 m, a conservative approximation based on the scale of turbulence eddies observed in historic Plinian eruptions (ranging up to several hundred meters in diameter). This treatment of turbulence viscosity is not intended to be physically rigorous, but only to give a crude minimum approximation of turbulence effects.

When equations 3-1,2,3 are written in expanded form for cylindrical coordinates in two dimensions, the result is a system of eight coupled, nonlinear, partial differential equations with sixteen dependent variables. Closure of the partial differential equations is obtained by applying the following algebraic relationships (Equations 3-6 - 3-12):

$$I_s = c_{vs} T_s \quad (3-6a)$$

$$I_g = c_{vg} T_g \quad (3-6b)$$

$$p = (\gamma - 1)\rho_g I_g \quad (3-7)$$

$$\theta_g = 1 - \theta_s \quad (3-8)$$

$$K_g = -K_s \quad (3-9)$$

$$R_g = -R_s \quad (3-10)$$

Equations 3-6a,b are the thermal equations of state for each phase, with  $c_{vs}$  and  $c_{vg}$  being the specific heats at constant volume for the solid and gas phases, respectively. Specific heats are treated as constants (for values see Appendix 3B). Equation 3-7 is the mechanical equation of state for the gas phase, with  $\gamma$ , a constant, being the ratio of specific heats at constant pressure and constant volume of the gas. Equation 3-8 relates the volume fraction of the gas phase to that of the solid phase. Equations 3-9 and 3-10 state that momentum and heat transfer between phases are coupled in such a manner that a gain in momentum/heat by one phase is the result of loss of momentum/heat in the other phase.

The functions  $K_s$  and  $R_s$  are given by

$$K_s = \frac{3\theta_s \rho_g c_d}{16r_s} |\dot{u}| \quad (3-11)$$

and

$$R_s = \frac{-3\theta_s \epsilon}{r_s} [e_s T_s^4 - a_g T_g^4] - \frac{3\theta_s k_g}{2r_s^2} [2.0 + 0.6(Ry_s^{1/2} Pr_g^{1/3})] \Delta T, \quad (3-12)$$

where

$$Ry_s = \frac{2r_s |\Delta \dot{u}|}{\nu_g}, \quad (3-13)$$

$$Pr_g = \frac{c_{pg} \rho_g \nu_g}{k_g}, \quad (3-14)$$

and

$$\Delta T = T_s - T_g \quad (3-15)$$

Equation 3-11 is simplified from Harlow and Amsden (1975) in which  $c_d$  is a drag coefficient (taken as unity for this work following the analysis of Walker et al. 1971) and  $r_s$  is the radius of the particles. Equation 3-12, the heat transfer function, is the sum of heat transfer due to radiation and forced convection. In the radiative heat transfer term,  $\epsilon$  is the Stefan-Boltzmann constant, and  $a_g$  and  $e_s$  are the absorptivity of the gas and emissivity of the particles, respectively (note that this is written to represent radiative transport from the particles to the gas). For conditions

of interest here, particles emit radiation in the near-infrared region of the electromagnetic spectrum, so that the gas phase (water vapor) has  $a_g \approx 0.9$  (Flaud et al. 1977) and the particle phase has  $e_s \approx 0.8$ . The forced-convection term in Equation 3-12 is an empirical relation involving Reynolds and Prandtl numbers (Equations 3-13 and 3-14), with  $c_{pg} = \gamma c_{vg}$  and  $\nu_g$  being the kinematic viscosity of the gas alone (Appendix 3B). Detailed discussions and development of the terms in Equation 3-12 for single spheres are given in Chapters 13 and 14 of Bird et al. (1960) (note that Equation 3-12 accounts for more than one particle, as determined by  $\theta_s$  and  $r_s$ ). Radiative heat transfer is minor compared to heat transfer via forced convection for cases of interest here.

The computational domain is shown in Figure 3-1. The axis of the flow is modeled as a rigid reflector in order to preserve the symmetry of the system. The Earth's surface is modeled as a smooth, free-slip reflector because any boundary layer phenomena are expected to occur on a scale too small to be resolved by the mesh. The upper and right-hand edges of the domain are "open" to allow flow out of the domain. The atmosphere is gravitationally stable with an exponential density stratification, and is modeled as a perfect gas with the same isentropic exponent as the erupting gas. Treatment of the atmosphere as steam instead of air does not have a strong effect on the large-scale features of an eruption because of the small difference in  $\gamma$  for the two gases. This

simplification greatly reduces required computation time (otherwise the problem would be a three-phase flow). The computational domain covers an area of 7 x 7 km, and is divided into an Eulerian (fixed reference frame) grid of 100 x 100 m squares. The time step for computation is set at 0.02 s, which satisfies the Courant condition for flow speeds up to 5000 m/s. Eruption discharge begins at  $t = 0$  and computation of the flow field continues until  $t = 200$  s, which roughly corresponds to the achievement of steady state flow within the computational domain for most runs. Eruption discharge is fixed by the operator for these steady discharge experiments, in contrast to earlier simulations carried out by Wohletz et al. (1984) where discharge was a time-dependent, computed condition. All of the numerical experiments reported here have exit temperatures of 1200 K. The numerical representation of the equations and accuracy are discussed in Appendix 3D. The computer code, "DASH" (dusty air shock), originally written by T. Cook and F. Harlow of Los Alamos National Laboratory, has been modified for applications to volcanic problems by M. Horn (Horn 1986).

51 numerical experiments were completed in order to make a sensitivity study of the effect of various initial and boundary conditions upon the modeled eruption. Of greatest interest were the effects of differing values of inflow gas pressure, velocity, particle loading, and particle size at the vent exit plane. Appendix 3C lists these conditions for all the computer runs, and particular models will be identified by their run number. Because

the solutions obtained are listed by the computer for each variable given above and for each computational cell and time step, a large volume of numerical results were generated. Each run produced more than 500 pages of printed data. Graphics programs were written to produce six r-z contour plots of  $\theta_s$ ,  $\log \theta_s$ ,  $\rho_g$ ,  $p$ ,  $T_s$ , and  $T_g$  for each time step. Two additional r-z vector plots show  $\vec{u}_s$  and  $\vec{u}_g$ . More than 400 plots were recorded for each run. Each run required about 2.5 hours of Cray-1 time (note that this machine vectorizes arrays and operates at a rate of about  $10^8$  floating point operations per second).

#### Dimensionless Parameters

The approach for study of the large volume of numerical data generated by these experiments consists of non-dimensionalization of data in order to compact and compare it. The dimensional analysis given here pertains to terms in the momentum equations (3-2a,b) as defined by exit conditions, and as such lends insight into the interplay of forces acting on an eruption column as it exits the vent. Because of the simplifications inherent in the model, the actual values of the dimensionless parameters cannot be extrapolated to natural eruptions. Relative variations in the parameters, however, can be used to understand processes in a natural eruption.

I focus on those variables that effect the large-scale behavior of eruption columns. Examination of the momentum equations (3-2a,b) reveals four different types of forces: (1)

inertia, (2) pressure gradient, (3) interphase drag, and (4) gravitation. Forces involving molecular or "dusty-gas" viscosity are negligible compared to these forces, as shown in Appendix 3E, and the effects of the turbulence viscosity are not considered in this discussion. The pressure gradient at the vent can be represented by the difference between exit pressure and local atmospheric pressure. Interphase drag or momentum coupling can be represented by the settling velocity of particles, with low settling velocities reflecting good coupling. Gravitational forces acting on an eruption column are determined by the density difference between the erupting mixture and the ambient atmosphere, and the size scale of the column which is measured by the vent radius. Gravitational forces thus can be also called buoyancy forces, since an eruption column exiting with a bulk density equal to that of the atmosphere will experience no downward acceleration from gravity.

All these effects are put into ratios to form the following parameters:

$$Tg_m = \frac{p_e - p_{atm}}{(\rho_m - \rho_{atm})gR_v} \quad , \quad (3-16)$$

$$Pn = \frac{w_s}{v_e} \quad , \quad (3-17)$$

$$Ri_m = \frac{\rho_m v_e^2}{(\rho_m - \rho_{atm}) g R_v} \quad (3-18)$$

For these equations, subscript e refers to conditions at the vent exit plane,  $v_e$  being the initial vertical velocity (both phases are assigned equal velocities at the exit), and  $w_s$  being the terminal velocity of the particles. Terminal velocity is arrived at by balancing gravitational and drag forces on a particle so that, within the simplified treatment in this chapter,

$$w_s = \left[ \frac{16 r_s g (\rho_s - \rho_g)}{3 c_d \rho_g} \right]^{1/2} \quad (3-19)$$

The mixture density is determined by  $\rho_m = \theta_s \rho_s + \theta_g \rho_g$ .  $R_v$  is the vent radius. In words,  $Tg_m$ , here referred to as the "thermogravitational parameter," is a ratio of thermodynamic (pressure) driving forces to buoyancy forces;  $P_n$ , the Rouse number, is a ratio of clast settling velocity to upward flow velocity; and the Richardson number,  $Ri_m$ , is a ratio of inertial forces to buoyancy forces. The subscript m indicates that these parameters are defined in terms of the properties of the erupting mixture. For very small particles with low values of the Rouse number, the mixture will behave nearly as a single continuum, since the

particles are in near-equilibrium with the gas both thermally and dynamically.

Another parameter that affects the large-scale dynamics of the eruption column is the ratio of exit pressure to ambient pressure,  $K_p$ , given by

$$K_p = \frac{p_e}{p_{atm}} \quad . \quad (3-20)$$

This parameter influences the shape and velocity field of the column (Liepmann and Roshko 1957; Kieffer 1984), and is discussed in detail in a forthcoming section. Other parameters that will be discussed in this chapter include the density ratio ( $D_s$ ) defined by

$$D_s = \frac{\rho_m}{\rho_{atm}} \quad , \quad (3-21)$$

and the Mach number ( $M$ ) defined by

$$M = \frac{u_m}{c_m} \quad , \quad (3-22)$$

where the mixture sound speed ( $c_m$ ) is given by (Kieffer 1981)

$$c_m = \left[ \frac{(c_{pg} + mc_{vs})}{(c_{vg} + mc_{vs})} \frac{c_v(\gamma - 1)T}{(1 + m)} \right]^{1/2} \quad . \quad (3-23)$$

In this equation,  $m$  is the mass ratio of solids to gas. The Mach number as defined here only holds for small particles with low  $Pn$ , so that the mixture can be approximated as a single continuum (pseudogas). Note that  $u_m$  in Equation 3-22 is the magnitude of the velocity of the mixture, implying that there is no slip between phases. For runs where particles are larger than  $10^{-4}$  m (above which slip velocities exceed about 10% of the gas velocity),  $M$  is not calculated.

Dimensional and dimensionless parameters for all runs reported in this chapter are tabulated in Appendix 3C. Included in Appendix 3C are values of mass discharge rate of magma ( $D = \pi R_v^2 \rho_m v_e$ ) for comparison with previously published values.

#### GENERAL FEATURES OF THE NUMERICAL EXPERIMENTS

Definition of some terminology will facilitate description of various features of the model runs. These terms are illustrated for an example eruption in Figure 3-2. The "column" designates the main vertical part of the eruption flow field above the vent. The "working surface" is at the top of the column, where large-scale vorticity and an increased diameter result from the column's penetration into the atmosphere. This term is adapted from Blandford and Rees (1974) and Norman et al. (1982), who have modeled the structure of high-speed jets for astrophysical applications. When a column does not collapse it will be referred to as a "Plinian column," in contrast to a "fountain" that develops

when a column collapses. The laterally-moving, ground-hugging flow that results from a fountain is called the "pyroclastic flow." The word "flow" will be used to describe fluid motions in general unless it is preceded by "pyroclastic," which restricts it to the above definition. "Pyroclastic-flow head" is the front of a pyroclastic flow.

Two example numerical experiments are shown in Figures 3-3 and 3-4. The plots show several types of information. Contours of the logarithm of ash volume fraction ( $\theta_s$ ), each contour being an order of magnitude different from neighboring contours, give an idea of the morphology of the cloud and the distribution of particles. The innermost contour, where most of the ash in a given eruption resides, corresponds to  $\theta_s$  at the exit plane. The velocity field of the solid phase is superimposed on the volume-fraction plots. Velocity vectors are drawn outward from the center of each computational cell in the direction of flow and with length proportional to flow speed. The combined  $\theta_s$ -velocity plots are especially useful because they give information about the shape and motion of the eruption cloud, which can be compared to observed natural eruptions. Pressure and density contours are shown for the compressible (gas) phase, and temperature contours of the solid phase are also given. Plots of gas temperature and velocity are not shown here but are very similar to the corresponding ones for the solid field except where the particles are relatively coarse.

The eruption discharge begins at time zero. The fast flow of dense material into the atmosphere results in an initial compression pulse that travels away from the vent as a hemispherical wave. Gas density and pressure plots at early times display this pulse. In this numerical model, the pressure signal is diffused over several computational cells, but in nature it is likely that this signal would form a shock (pressure discontinuity) after travelling a small distance from the vent (Kieffer 1981; Wohletz et al. 1984). As eruption time progresses, the eruption columns continue to rise, and, at late time, the models shown in Figures 3-3 and 3-4 begin to depart significantly in their behavior. The eruption column in Figure 3-3 begins to spread laterally at several kilometers altitude, but after the spreading it continues to rise until the working surface is out of the computational domain. The run in Figure 3-4 also begins to spread laterally at several kilometers altitude, but instead of continuing upward, the part of the column that has spread then falls back to the ground, resulting in a pyroclastic flow. The interpretation of these two types of behavior follows volcanologic observation: Figure 3-3 represents an eruption that produces a high-standing Plinian column, while Figure 3-4 is a fountain that produces pyroclastic flows. Details of the behavior of noncollapsing and collapsing columns are discussed below. Most important at this stage, however, is an understanding of the conditions that determine whether or not a column will collapse.

Figure 3-2: Illustration of terminology for various features of a Plinian eruption.

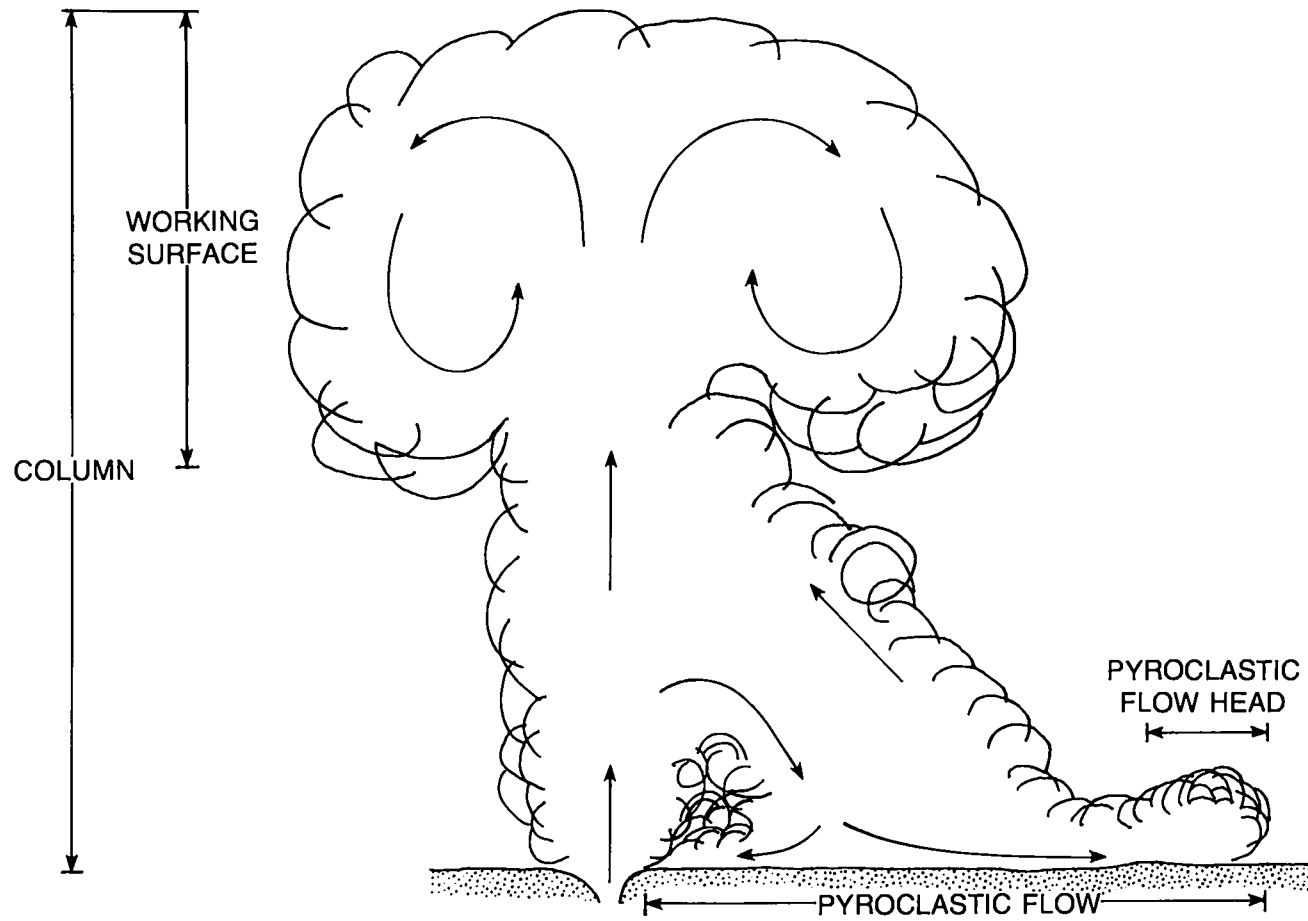


Figure 3-3: Numerical eruption producing a Plinian column (Run 49). Contour plots of  $\log\theta_S - \vec{u}_S$ ,  $p$ ,  $\rho_g$ , and  $T_S$  are shown for three times after initiation of discharge (10, 80, and 110 s). The innermost  $\log\theta_S$  contour corresponds to  $\theta_S = 10^{-3}$ , and each contour outward represents an order of magnitude decrease in  $\theta_S$ . Maximum flow speeds of about 400 m/s are attained in the basal 2 km of the column. The exit pressure of this eruption is 0.69 MPa ( $K_p = 6.9$ ). The initial atmospheric pressure signal is shown in the pressure and gas-density plots at  $t = 10$  s as a perturbation in the ambient values.  $T_S = 1200$  K at the exit plane (this temperature is used for all runs reported in this chapter).  $T_S$  contours are drawn at 100 K intervals, so that the outermost temperature contour corresponds to 500 K. See detail of the basal portion of the column in Figure 3-6.

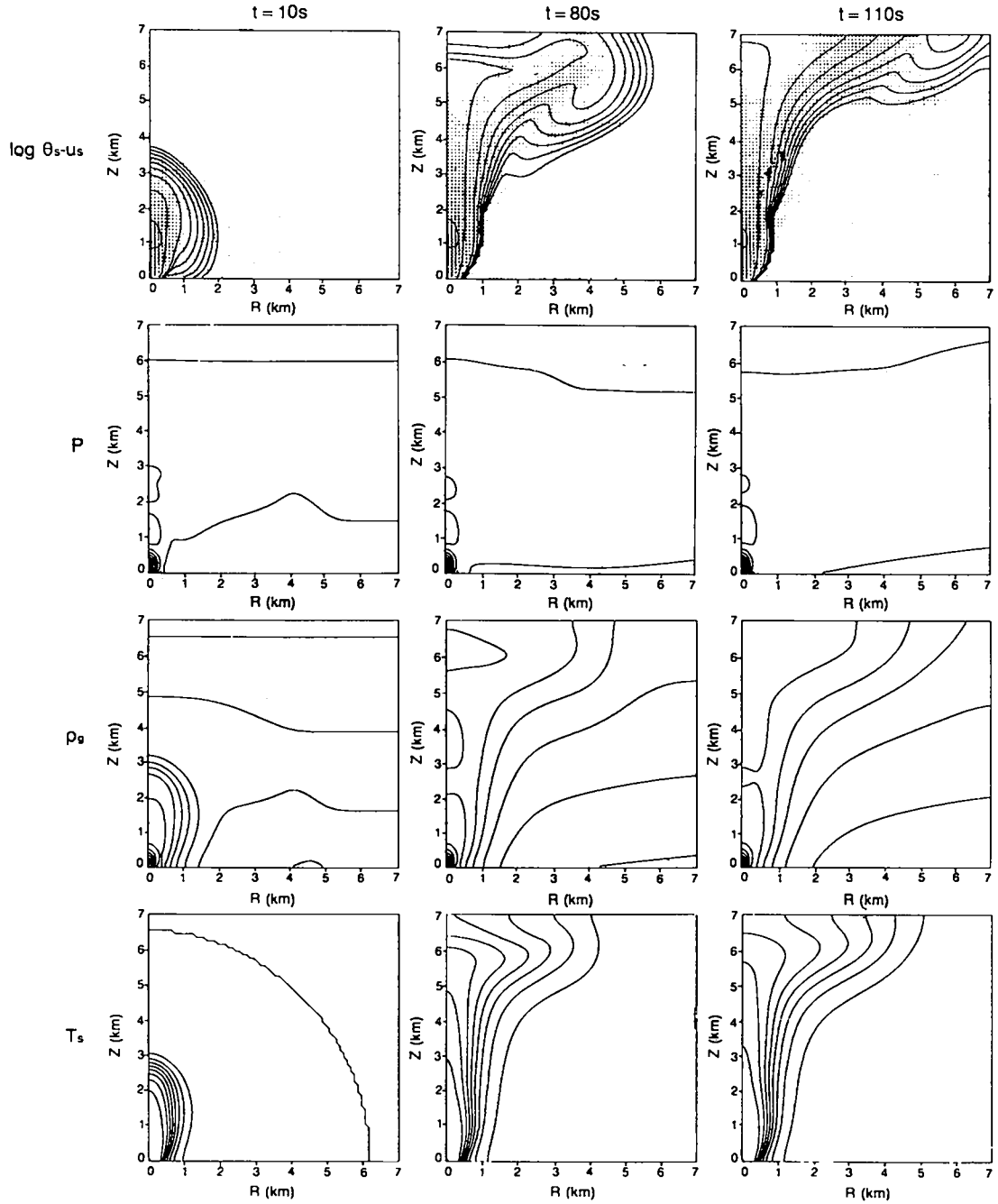
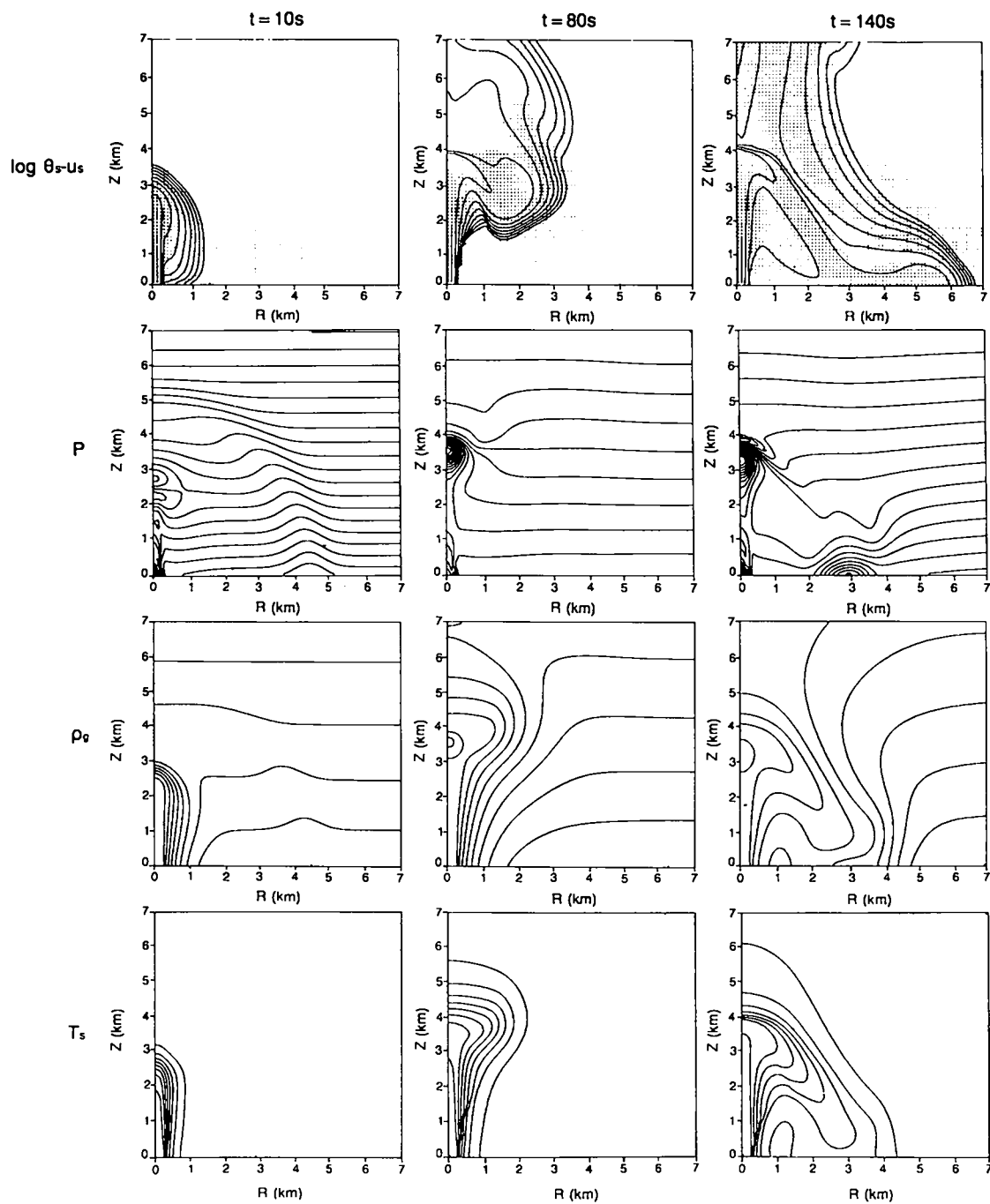


Figure 3-4: Numerical experiment producing a pyroclastic fountain (Run 8). Contour plots of  $\log\theta_s - \vec{u}_s$ ,  $P$ ,  $\rho_g$ , and  $T_s$  are shown at  $t = 10, 80, \text{ and } 140$  s. The innermost  $\theta_s$  contour corresponds to a solid volume fraction of  $10^{-3}$ , and maximum speed of 300 m/s occurs at the exit plane. The exit pressure of this eruption equals the ambient pressure ( $K_p = 1$ ). Note the atmospheric pressure signal at  $t = 10$  s, which shows with better resolution than the eruption of Figure 3-3 because pressure contours are drawn at smaller intervals for this run. High pressure cells are located at the elevation of collapse and where the collapsing flow impinges upon the ground. The contour plot of  $\rho_g$  at  $t = 140$  s shows how hot, relatively low-density gas is dragged beneath relatively high-density ambient gas by the solid phase, producing an unstable situation where the hot gas tends to rise out of the basal flow. This in turn leads to development of a cloud of ash that rises above the basal pyroclastic flow due to buoyancy.  $T_s$  contours follow closely plot of  $\rho_g$ .



### Eruption Column Collapse

As discussed in the section Dimensionless Parameters, variables affecting the large-scale behavior of eruption columns are summarized in the parameters  $Tg_m$ ,  $Ri_m$ ,  $Pn$ , and  $K_p$ . Special attention is given here to  $Tg_m$ ,  $Ri_m$ , and  $K_p$ . The effect of the Rouse number is such that a column with large- $Pn$  clasts will tend to collapse under conditions that would otherwise produce a Plinian column. This result illustrates the tendency of large- $Pn$  clasts to follow nearly ballistic paths. Note that computations in DASH apply one particle size per run and do not follow size distributions that are found in nature, which limits the full interpretation of particle size effects. The effect of multiple particle sizes in an eruption is a subject for other calculations and is not presented here. So, while it is reasonable to predict that an overall increase in  $Pn$  will produce a tendency toward column collapse, a specific relationship is not sought by using a single-particle-size model. On the other hand, by varying the properties of the eruptive mixtures, while retaining a constant particle size (approximately constant  $Pn$ ), the behavior of the eruptions with constant size distributions can be compared.

Intuitively, one might expect a large  $Tg_m$  to be typical of Plinian columns, since this implies a large upward driving force from the pressure gradient relative to the downward force of negative buoyancy (where the column exits with a density larger than that of the atmosphere). The same is true of the Richardson

number -- a large initial component of inertia will counteract the negative buoyancy. Indeed, the Richardson number, which is determined by the mixture density (directly related to exsolved gas content), exit velocity, and vent radius, embodies all the variables considered by Sparks et al. (1978), Wilson et al. (1980), and Wilson and Walker (1987). Since  $Tg_m$  and  $Ri_m$  contain all the major forces acting on an eruption column, a collapse criterion might be completely defined in terms of these two parameters. In the course of the numerical experiments, however, it was found that column collapse is also very sensitive to the pressure ratio. This result follows from the effect of overpressure ( $K_p > 1$ ) on column structure (Kieffer, 1981, 1982, 1984; Kieffer and Sturtevant, 1984); as the supersonic flow exits the vent, the gas phase expands and accelerates to achieve pressure equilibrium with the atmosphere. This gas expansion decreases the flow's bulk density and thus decreases the magnitude of the negative buoyancy force (details of jet structure in the model runs will be discussed in a later section). The transfer of kinetic energy to internal energy that takes place across the subsequent shock (referred to as the Mach disk shock) is mainly reflected in a temperature increase and velocity decrease. Above the Mach disk shock, velocity returns to values very similar to those found at equivalent altitudes in a pressure-balanced jet. However, the mixture density does not increase very much across the shock so that there is a net decrease of density relative to a pressure-balanced jet. Thus, after going

through the initial expansion and shock stage, the flow still has a large velocity but the negative buoyancy force is greatly reduced. The importance of the pressure ratio relative to the density ratio is shown in several of the numerical experiments. For example, Run 26 ( $K_p = 20$ ) has an exit density about nine times as large as Run 67 ( $K_p = 2$ ). Even though they have the same values of  $Tg_m$  and  $Ri_m$ , the denser run forms a Plinian column and the less dense run forms a fountain.

In summary, three dimensionless parameters can be used to determine the conditions necessary for Plinian columns or fountains. A column collapse criterion, established by a sensitivity analysis of the computer results, forms a surface in  $Tg_m$ - $Ri_m$ - $K_p$  space (Figure 3-5). Although this criterion does not directly apply to natural eruptions, it does demonstrate how the main driving forces combine in a nonlinear manner to control the dynamics of an eruption column. In terms of measurable eruption quantities, this criterion suggests that, in general, if conditions in an eruption tend toward lower exit pressure, lower exit velocity, higher mixture density (lower gas content), and larger vent radius, then that eruption will tend to evolve toward a collapsing column or fountain. Values of the dimensionless parameters are coupled (e.g., pressure is affected by vent radius), so the parameters cannot be considered independent of each other.

Sparks et al. (1978), Wilson et al. (1980), and Wilson and Walker (1987) proposed collapse criteria based upon the effects of

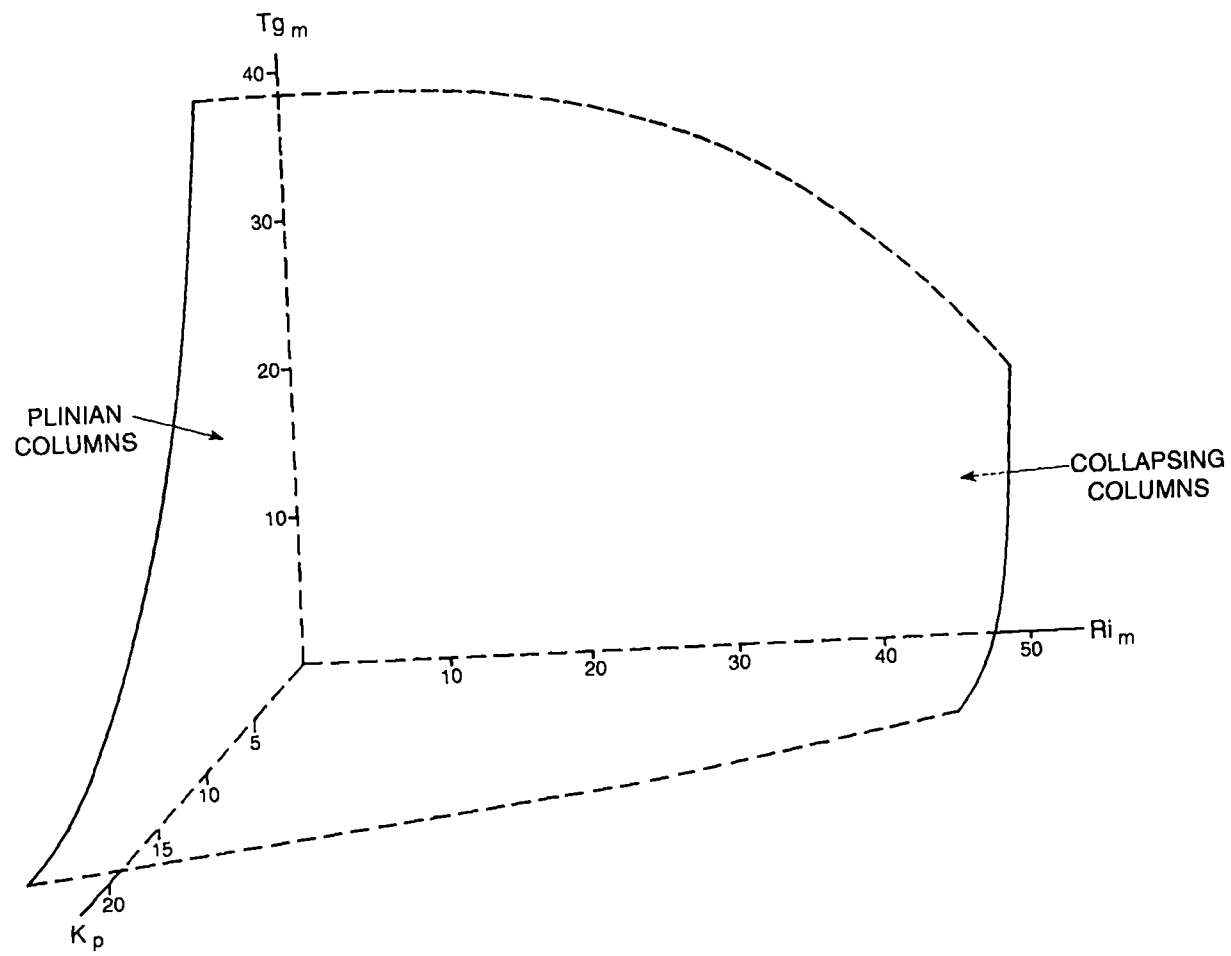
exit velocity, gas content, and vent radius. The important difference between results presented here and the previous criteria is the inclusion of thermodynamic (pressure) effects. The previous criteria, as mentioned earlier, do not directly account for the thermodynamics of the flows because they assume that columns are pressure-balanced and remain in equilibrium with the local ambient pressure at all heights above the vent. Since pressure fluctuations of at least a few bars are to be expected during an eruption (even during the steady phases of discharge, because of vent erosion), it is of primary importance to account for exit pressure. Formation of a Plinian column does not require entrainment and heating of atmospheric air. Although it is clear from observations that turbulence and related entrainment operate to some degree during Plinian eruptions, the pressure effects presented here do not support the earlier assumption that column behavior is determined entirely by the efficiency of air entrainment.

#### Evolution of the Modeled Eruption Columns

##### Non-collapsing (Plinian)

I now focus on the model eruption shown in Figure 3-3 (Run 49). The various plots are shown for times of 10, 80, and 110 seconds after discharge begins. Conditions for this eruption (Appendix 3C) place it above the surface separating Plinian columns from fountains in Figure 3-5. The eruption is overpressured, which plays an important role in its appearance and behavior.

Figure 3-5: Collapse of eruption columns (assuming similar particle size characteristics) is determined largely by the values of  $T_{gm}$ ,  $R_{im}$ , and  $K_p$  as defined for exit conditions. Critical conditions for column collapse appear to form a surface in three-dimensional space defined by these three parameters, as shown here. Exit conditions that plot above the surface produce Plinian columns, while those below the surface produce collapsing columns or fountains leading to pyroclastic flows.



By  $t = 10$  s, the top of the column is at about 3.5 km elevation. Velocity vectors show an initial radial-outward flow immediately above the vent followed by a radial-inward flow above about 1.5 km elevation. Between about 0.8 km and 1.5 km there is a region of low  $\theta_s$  directly corresponding to a region of low pressure. These features are related to the internal structure of the supersonic, overpressured column. The velocity vectors show vortex development at just above 2 km elevation (not visible in Figure 3-3); this structure corresponds to the rolling vortex of the working surface that is observed in natural eruptions and laboratory experiments (Kieffer and Sturtevant 1984). Overall, the eruption column at this stage is rather wide due to initial radial flow. The atmospheric pressure signal, apparent in the gas pressure and density plots, has reached a distance of about 5 km from the vent, and about four seconds later it propagates out of the computational domain.

Plots for  $t = 80$  s show the outer sheath of the column continuing to be pulled upward into the rolling vortex, which has experienced an outward displacement in addition to its general upward movement. The lower 1 km of the column shows the characteristic flaring or diamond-like structure of overpressured jets (the step-like appearance of this flaring is an artifact of the numerical mesh). Regions of relative low and high gas pressure and density further illustrate the typical structure of an overpressured jet. Near the top of the computational domain the

gas pressure within the column is somewhat higher than that of the adjacent atmosphere. This is due to a decrease in velocity at this elevation and resultant conversion of kinetic energy to internal energy. By  $t = 110$  s, the velocity at this elevation has increased and pressure has decreased accordingly. Also at  $t = 110$  s, the rolling vortex, which has spread laterally to the edge of the computational domain, is beginning to accelerate rapidly upward and out of the domain, and by  $t = 140$  s (not shown) the working surface has completely exited the domain.

As mentioned earlier the external form displayed by the model column reflects the internal structures typical of overpressured jets, and it is appropriate at this point to discuss in some detail the internal structure of the overpressured Run 49. In particular, I focus on the lowest 2.5 km, where jet dynamics as discussed by Kieffer (1981, 1984) and Kieffer and Sturtevant (1984) dominate the flow. Figure 3-6 shows detailed radial profiles of pressure, solid volume fraction, and mixture density at 500 m intervals above the vent when  $t = 64$  s. At each elevation interval, local atmospheric pressure and density are shown by dashed lines. The outer edge of the eruption column corresponds to the location of the  $\theta_s = 10^{-6}$  contour, which approximates the visible edge of the eruption column (Horn 1986).

At zero elevation (the exit plane), the pressure exceeds atmospheric (by a factor of 6.9 in this case) in the inner 200 m. Although the vent has a radius of 200 m, the mixture immediately

expands to give the column a basal radius of slightly more than 400 m. Beyond the edge of the vent, however, the flow has undergone Prandtl-Meyer expansion to a pressure slightly lower than atmospheric. Because of this expansion of the gas phase,  $\theta_s$  is decreased by more than an order of magnitude relative to its exit value. Mixture density follows the trend of solid volume fraction.

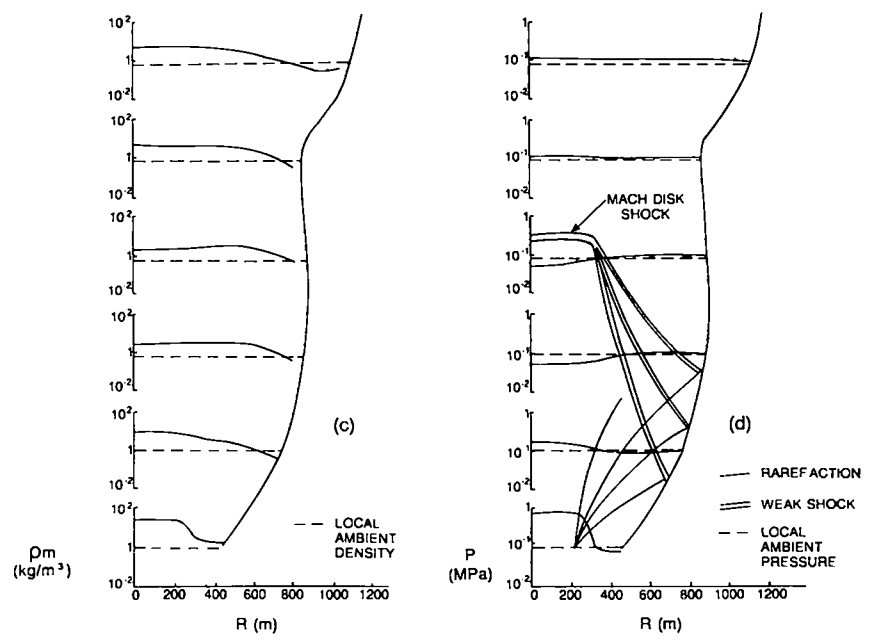
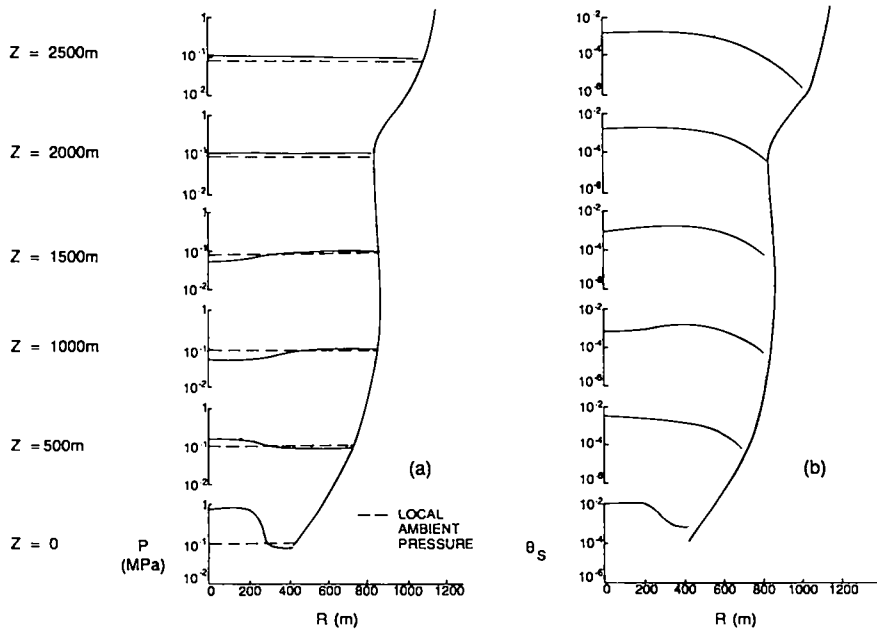
At 500 m, the amount of overpressure in the core of the column has decreased significantly compared to conditions at the vent. Along the margins of the column, beyond about 300 m from its center, the pressure has increased relative to the zero elevation value, so that it is nearly equal to the local atmospheric pressure.  $\theta_s$  and mixture density have maximum values at the center of the column and decrease outward.

At 1000 m elevation, the pressure within the inner 500 m of the column is substantially lower than local atmospheric pressure. Beyond this inner region, the flow is close to atmospheric pressure. This distribution of pressure is the result of overcompensation of the flow in its trend toward pressure equilibrium with the atmosphere, and produces  $\theta_s$  and mixture density profiles with maxima located away from the center of the column. At 1500 m elevation, the pressure within the inner 300 m of the column is still less than atmospheric, and the outer part of the column is now slightly overpressured relative to the atmosphere. Again, the solid-volume-fraction and mixture-density plots have maxima located away from the center of the flow.

By 2000 m elevation, the core of the flow has recompressed so that it has a pressure slightly higher than the local atmospheric;  $\theta_s$  and  $\rho_m$  have maximum values in the center of the column and decrease steadily outward.

These phenomena can be explained in terms of observations from experiments with overpressured jets (JANNAF 1975; Kieffer 1984; Kieffer and Sturtevant 1984) and detailed numerical modeling of jets (Norman et al. 1982). This previous experimental and numerical work has shown that overpressured, supersonic jets flare rapidly upon exiting their nozzles (vents) and expand by the Prandtl-Meyer process. Oblique rarefactions reflect off the edges of the jets to form weak converging shocks. The shocks meet at some distance downflow of the nozzle exit and form a strong shock that is parallel to the exit plane (Mach disk shock). Approximate locations of rarefactions and shocks in the model run discussed above are shown in Figure 3-6d. Rarefaction zones are well represented in the numerical model because in reality they are zones of smooth pressure gradients. Shocks, on the other hand, are nearly discontinuities in real gas flows. However, in the numerical results they are smeared out over larger distances than would be expected in nature due to numerical diffusion (Hirt 1968). In addition, the presence of particles in a gas flow produces an effective thickening of shocks, because, although the gas itself undergoes a sharp discontinuity, the imperfect coupling of particles and gas requires a finite distance for the particles to

Figure 3-6: Detail of the basal 2.5 km of the overpressured eruption shown in Figure 3-3. Radial variations of  $p$  (a),  $\theta_s$  (b), and mixture density  $\rho_m$  (c) are plotted at 500 m intervals above the exit plane. (d) shows how oblique rarefactions and shocks interact with the flow to produce the observed dynamics. See text for detailed discussion.



regain equilibrium with the gas (Carrier 1958; Rudinger 1960; Marble 1970). Thus there are no sharply defined shocks produced by the numerical model, which instead shows regions of rapid compression, illustrated as shocks drawn in Figure 3-6d.

Collapsing column (fountain)

Figure 3-4 shows the evolution of an example collapsing eruption column and resulting pyroclastic flow (Run 8, see Appendix 3C). This eruption plots below the critical surface of Figure 3-5, and is in pressure equilibrium with the atmosphere at the exit plane.

At  $t = 10$  s, the working surface is between 2 and 3.5 km elevation with velocity vectors showing development of a rolling vortex in this region (not visible at scale of figures). The velocity vectors also show a rapid deceleration toward the top of the column along the r-axis. This deceleration produces high-pressure regions in the flow as kinetic energy is converted to internal energy (manifested as pressure). The atmospheric pressure signal is about 5 km from the vent at 10 seconds, and out of the computational domain a few seconds later.

At  $t = 80$  s, the column has spread laterally at an elevation of about 3.5 km, and that part of the flow is beginning to collapse toward the ground. At the elevation of collapse, vertical velocity along the axis of symmetry has decreased to zero, resulting in a high-pressure (and high gas density) cell. Also noteworthy is the difference between the shapes of the bases of the eruption columns

shown in Figures 3-3 and 3-4. The model in Figure 3-4 exits at atmospheric pressure and does not display the flaring property of the run in Figure 3-3. Note the well-developed vortex above the front of the collapsing flow (here referred to as the "stem"). Also note that significant quantities of ash continue to rise above the forming fountain. This observation is consistent with observations from modern eruptions, and serves to point out a difficulty in using cloud shape to determine whether or not a column is collapsing. If a column is undergoing asymmetrical collapse, an observer on one side may witness collapse and resulting pyroclastic flows, while an observer on the other side will only see a steadily-rising plume of ash. Thus two radically different interpretations of eruption dynamics could result from real-time observations of the same eruption, and it is expected that pyroclastic flow deposits and fallout deposits may form contemporaneously (this possibility is suggested from field observations of deposits from the 1912 eruptions of Novarupta; Hildreth 1987).

By  $t = 140$  s, pyroclastic flows are moving laterally across the ground. A high pressure cell is present where the collapsing stem impinges on the substrate, reflecting rapid deceleration and conversion of kinetic energy into internal energy. The gas density plot shows that the collapsing flow results in injection of less dense, hot gas beneath a relatively cooler and denser atmosphere. There are two components of pyroclastic ground flow: one component

moves outward while the second component of pyroclastic flow moves inward toward the vent. At 140 s, the inward moving component is just beginning to meet the main column, where later it is reincorporated into the column. This phenomenon may produce considerable recycling of material during the course of an eruption, a possible consequence being the mixing of earlier erupted ash with later products. This process has not been documented in the field, but it may be responsible for obscuring temporal magma compositional changes that otherwise might be preserved by vertical zonation of the pyroclastic deposit. For example, a sharp compositional interface in the magma chamber might be smeared out stratigraphically in corresponding ignimbrite, so that it may be incorrectly interpreted as having been a smooth compositional gradient. Whether this remixing process occurs during an eruption depends, for example, on the slope away from the vent. Where a collapsing stem impinges on an outward-dipping slope, the inward-flowing part may produce pyroclastic flow with insufficient momentum to flow up the slope toward the vent. Also, as will be discussed in a later section, clast sizes control the distances from the vent at which collapsing stems hit the ground. Coarse material collapsing very close to the vent can effectively damp out the backflow.

## IMPLICATIONS FOR PYROCLASTIC-FLOW TRANSPORT AND IGNIMBRITE FACIES

Results of the numerical experiments are not appropriate for application to outcrop features smaller than the 100 m computational grid. Most features observed on the outcrop scale are strongly influenced by the detailed rheology of pyroclastic flows (Sparks 1976; Wilson 1980; Wilson and Head 1981; Freundt and Schmincke 1986; Valentine and Fisher 1986). In the multiphase treatment used here, bulk fluid properties are essentially Newtonian, and a detailed treatment of pyroclastic flow mechanics could incorporate granular flow dynamics (Savage 1984). The strength of this model is that it sheds light on the large scale features of an eruption, and the interpretations presented below pertain only to broad facies relationships commonly observed in pyroclastic flow deposits (see reviews by Fisher and Schmincke 1984, pp. 203-206; Cas and Wright 1987, pp. 244-250).

### Pyroclastic Flows

The structure of model pyroclastic flows reflect important physical processes that control runout of pyroclastic flows and ignimbrite facies. In addition to the results of Run 8, shown in Figure 3-4, three other examples of fountains (Runs 19, 59, and 61) are shown in Figures 3-7,8,9, where  $\theta_s$  and velocity vectors are plotted at three times. Conditions for these runs are given in Appendix 3C, and the main variations relative to the run in Figure 3-4 are: a short eruption discharge duration (50 s) for Run 19;

Figure 3-7:  $\log\theta_s-\vec{u}_s$  plots of the flow field produced by a brief discharge duration (Run 19). At  $t = 50$  s, discharge is "turned off," and the flow is producing a collapsing fountain. Although the bulk of material in the eruption cloud produces laterally-moving pyroclastic flow, a buoyant cloud of ash continues to rise above the vent, attaining upward speeds in excess of 50 m/s. Note the well-developed vortex above the head of the pyroclastic flow, especially evident at  $t = 70$  s, and that maximum velocities in the ash plume occur away from the symmetry axis.

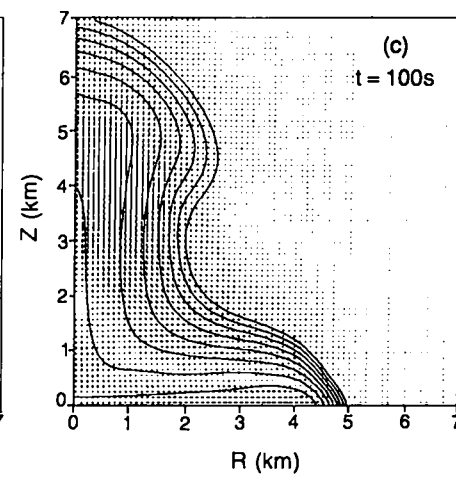
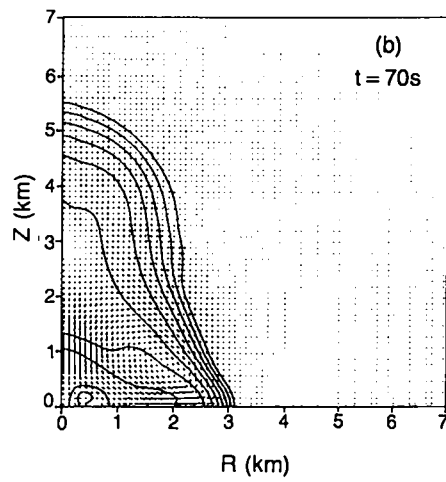
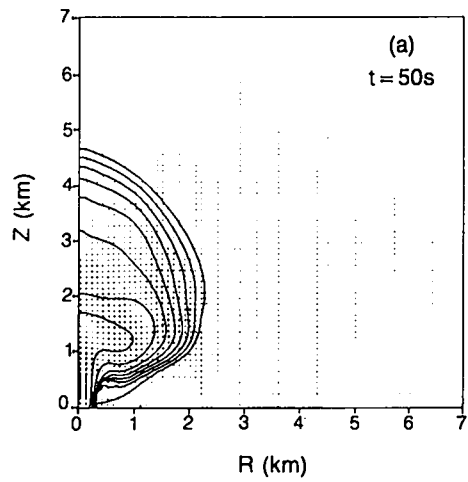


Figure 3-8:  $\log\theta_s-\vec{u}_s$  plots of coarse-grained eruption (Run 59).

Because of poor coupling between the gas and solid phases, structure of the pyroclastic flow is well illustrated by the innermost contour of the lateral flow. A relatively thick head with a slight overhang is shown, followed by a relatively thinner body of the flow.

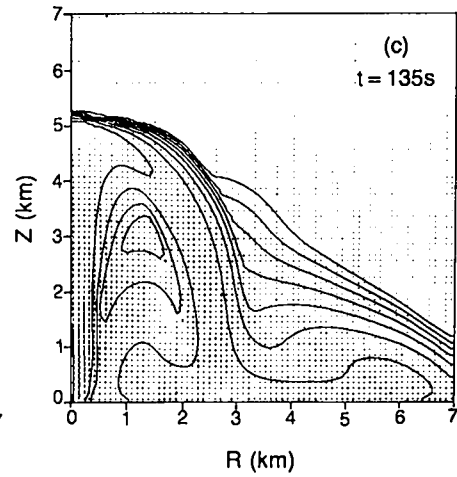
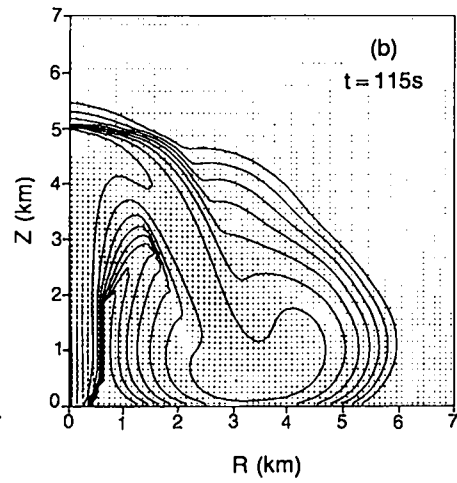
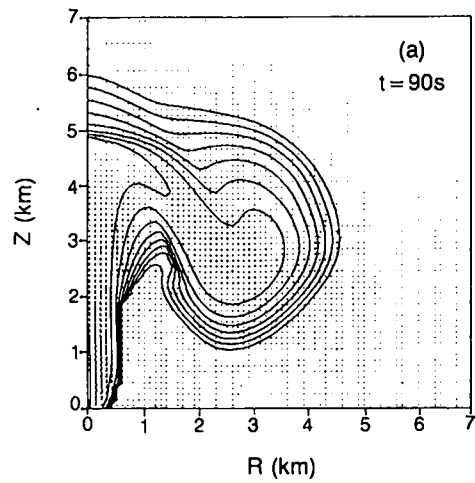
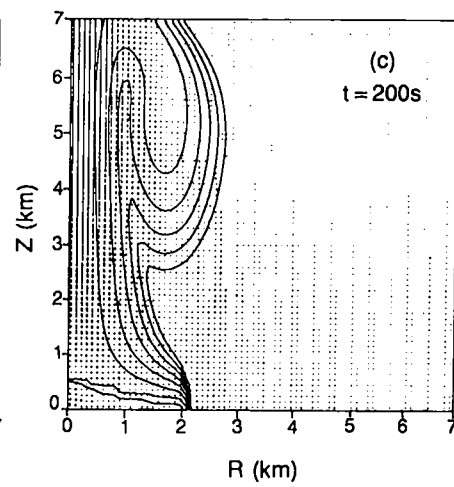
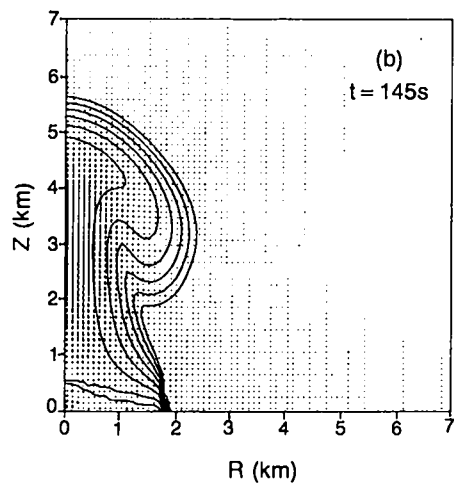
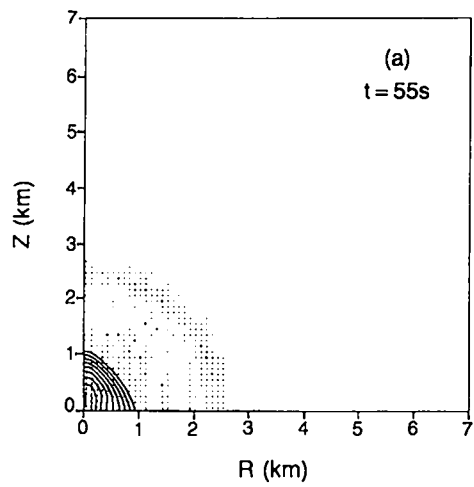


Figure 3-9:  $\log\theta_S-\vec{u}_S$  plots of a relatively weak eruption (Run 61).

Most of the pyroclastic material rises only 300 m above the vent, then moves laterally as a slow pyroclastic flow. However, a buoyant plume of ash continues to rise above the vent at relatively high speeds approaching 120 m/s (note the exit velocity is only 73 m/s). This rising ash cloud produces a strong radially inward flow in the atmosphere, which exerts sufficient drag on the pyroclastic flow to effectively stop its progress.



large particle Rouse number (particles are equivalent to 10 cm radius lithic fragments) for Run 59; and low  $Tg_m$  and  $Ri_m$  in Run 61.

Pyroclastic flows produced by brief discharge

Figure 3-7 (Run 19) shows the development of a pyroclastic flow and its evolution after discharge has ended. This has relevance for pyroclastic flows produced by relatively brief periods of column collapse either from eruptions consisting of discrete explosions or from sustained Plinian eruption columns with brief periods of instability (producing intra-Plinian pyroclastic flows; Wright 1981; Wilson and Walker 1985; Walker 1985). At  $t = 50$  s, the column begins to collapse at an elevation of about 2 km, and the eruption discharge is "turned off." 20 s later, at  $t = 70$  s, most of the erupted material (contained within the innermost  $\theta_s$  contour) is falling back to the ground and moving outward as the beginning stages of pyroclastic flow. Note the strong vortex development on top of the pyroclastic flow and that ash continues to rise immediately above the vent. The final snapshot in Figure 3-7 ( $t = 100$  s) shows the development of a pyroclastic flow with a relatively thick head that tapers gradually ventward to a lower-concentration tail. The head of the pyroclastic flow consists of a relatively low-concentration front and a well-developed vortex along its top. One might expect the deposits of such an eruption to reflect an initial low concentration phase, followed by a higher-concentration phase, and ending with another low-concentration phase. Note the cloud of buoyant ash rising above

the vent with relatively high velocities between about 3 - 6 km elevation. This phenomena suggests that it would be difficult to determine exactly when discharge ends based on field observations of eruption column dynamics.

Pyroclastic flows produced by coarse-grained eruption

Figure 3-8 shows Run 59 at  $t = 90, 115,$  and  $135$  s. This model eruption consists of clasts of large Rouse number (10 cm radius, density of  $2400 \text{ kg/m}^3$ ), so that interphase coupling is extremely poor. Note that this eruption has the same mixture parameters at the vent as Run 49. Run 49 (Figure 3-3) produced a Plinian column and Run 59 produced a fountain, which demonstrates the effect of  $Pn$  on eruption dynamics.

Because of the poor coupling between the solid and gas phase caused by large Rouse number, Run 59 permits observation of the development of density-current structure. At 90 s, the collapsing stem of the column has a well-developed head, caused by resistance of the atmosphere into which it is flowing and by drag associated with vortex flow. When  $t = 115$  s, the stem has just impinged on the ground, and by  $t = 135$  s, pyroclastic flows are moving rapidly outward and inward. Note that the inner contour of the pyroclastic flow, where the densest part of the flow exists, displays a thickened head with a slight overhang at its front. This is a common feature of density currents produced by laboratory experiments (Hampton 1972; Allen 1970, pp. 189-192), lending credence to the numerical model presented here. This structure

also supports ideas put forth by Wilson (1980, 1985), and Wilson and Walker (1982) on the geometry of pyroclastic flows.

At later times in the run of Figure 3-8, the dilute cloud that occurs above the pyroclastic flow gradually collapses toward the ground until it is less than 2 km thick. Compare this to runs with lower- $P_n$  particles, which produce buoyant, continuously rising ash clouds (discussed in detail below). This difference again is a reflection of the coupling between particles and gas.

Pyroclastic flows produced by low  $T_{gm}$ - $R_{im}$ - $K_p$  eruption

Figure 3-9 shows Run 61 at three times. As can be seen in Appendix 3C, this run has relatively low values of  $T_{gm}$  and  $R_{im}$ , and is pressure-balanced at the exit plane. In addition the Rouse number of the particle phase is low. These conditions correspond to natural conditions of low energy eruption in which eruptive products appear to "boil" over the vent rim (e.g. the eruption of Mount Lamington described by Taylor 1958).

Most of the material erupted during Run 61 rises only to 200-300 m above the vent, then collapses to form a slow-moving pyroclastic flow. A low-concentration cloud of ash continues to rise above this level; the beginning stages of this cloud are seen in the plot for  $t = 55$  s. After 145 s of discharge, the pyroclastic flow has only moved a total of about 2 km away from the vent. The buoyant ash cloud, however, is rising very rapidly, resulting in a strong radially-inward wind as the atmosphere is dragged up with the cloud. By  $t = 200$  s the inward wind produced

by ash-cloud rise is exerting enough drag on the low energy pyroclastic flow to effectively halt its progress. Material initially flowing outward in the pyroclastic flow is gradually fed into the head of the flow and then sucked up into the buoyant ash cloud. Thus it is seen that for a pyroclastic flow to make any lateral progress, it must have enough inertia to counteract the inward wind produced by the convective rise of the ash cloud above the vent.

The results of Run 61 point to yet another problem with field observation of eruptions. An eruption that produces a very low energy pyroclastic flow that is prematurely halted by wind drag may appear to be entirely Plinian, especially if near-vent topography or suspended ash hides the flow. Obviously, this would result in a gross misinterpretation of the energetics of that eruption.

#### Ground Surge

Basal deposits of ignimbrites commonly display features of pyroclastic surge deposits, such as improved sorting relative to pyroclastic flow deposits and cross stratification. These basal deposits were termed "ground surge" by Sparks and Walker (1973), and were placed in the layer 1 position of the "standard" ignimbrite sequence of Sparks et al. (1973) and Sparks (1976). Subsequent variants of layer 1 deposits include ground layers and fines-depleted ignimbrite (Walker et al. 1981; Wilson and Walker 1982). In addition, deposits that record turbulent boundary layer

processes in pyroclastic flows have been predicted by Valentine and Fisher (1986).

Layer 1 deposits that fall into the category of ground surge have been interpreted in terms of three models. First, Wilson and Walker (1982) suggest that ground surge deposits are associated with unsteady processes at the fronts of pyroclastic flows. Second, Wohletz et al. (1984) present numerical modeling that suggests ground surges may be related to initial unsteady flow and blasting phenomena at the beginning of an eruption. The third model (Fisher, 1979) suggests that these deposits record the initial stages of eruption column collapse. In Fisher's model, the outer sheath of the eruption column has a lower particle concentration and is finer-grained than its core. The lower concentration is postulated to be due to mixing with ambient air, and the fine-grained property is due to size grading inherited from the conduit flow. The model assumes that when column collapse begins the outer sheath of the column collapses first, producing fine-grained, low-concentration pyroclastic surges that are subsequently followed by denser, coarser-grained pyroclastic flows.

Numerical modeling of gas-particle flows moving through diverging nozzles by Ishii et al. (1987) shows that the outer parts of the flows have lower particle concentrations because of the relatively slow response of the particles to the nozzle shape, compared to the nearly instantaneous response of the gas. Thus if a volcanic eruption occurs through a flaring vent one might expect

higher particle concentrations and coarser sizes in the core of the eruption column flow than at its edges, supporting the idea put forth by Fisher (1979). The DASH models also indicate this concentration gradient, but they do not directly support the idea that the outer sheath of the column will collapse before the core. Instead, at the elevation of collapse, the entire cross section of the column "flops" downward at the same time. Still, as illustrated in Figure 3-4, the lower-concentration outer part of the column is pushed in front of the higher-concentration core material during initial collapse. The result is that lower concentration parts of the flow hit the ground first and then continue to move laterally in front of higher-concentration parts (note that this effect is exaggerated somewhat in the numerical experiments due to numerical diffusion; Hirt 1968). It is possible that this leading part of the flow may have characteristics of pyroclastic surges, and thus lay down bedded and cross bedded deposits just prior to the main pyroclastic flow. This is more likely to be an active process near the vent, because with increasing runout distance the low-concentration front may be stripped off by aerodynamic drag and possibly overtaken by the dense pyroclastic flow.

#### Ash Cloud

The presence of a dilute ash cloud above model pyroclastic fountains and related pyroclastic flows, mentioned several times in the preceding discussion, has several important implications. In

Figure 3-4 at  $t = 140$  s, notice the cloud of ash rising above the fountain and pyroclastic flow. This dilute ash cloud flows back toward the axis of symmetry by convective inflow of the atmosphere, and then rises to form a buoyant plume analogous to the ash cloud discussed by Fisher (1979) (see also documented ash clouds from the May 18, 1980 eruption of Mount St. Helens in Criswell 1987). The ash cloud is thought to deposit a "co-ignimbrite ash," layer 3 of the standard ignimbrite sequence of Sparks et al. (1973). Fine ash layers at the tops of pyroclastic flow units have been described at numerous locations (Wilson and Walker 1985; Wilson 1985; Bacon 1983; Sparks 1976; Fisher 1979). Recently, Rose and Chesner (1987) suggested that the voluminous 75 ka Toba eruption generated several hundred cubic kilometers of this co-ignimbrite ash. Layer 3 has been attributed to sorting of fine ash in collapsing eruption columns and elutriation of fine ash from the dense pyroclastic flow (Sparks and Walker 1977; Wilson 1980). Denlinger (1987) finds that turbulent-boundary-layer and granular-flow processes act together to produce ash clouds. Layer 3 seems to have been deposited by fallout in some cases and by lateral transport in others (i.e. ash cloud surge of Fisher 1979).

DASH results indicate the following interpretation. Ash may buoyantly rise above the main pyroclastic flow, carried by rising hot gas (fluidization; Wilson 1980, 1984) and by diffusive processes such as turbulence (Denlinger 1987). The rising ash forms a relatively low-concentration cloud that flows inward,

relative to the main pyroclastic flow, toward the main axis of the eruption column. As mentioned above, this is largely due to drag from atmospheric wind that is pulled inward and upward with the eruption column. The majority of ash cloud material rises buoyantly and is later deposited by fallout. Coarser tephra may be deposited during the backflow of the ash cloud, resulting in dunes and other features typical of pyroclastic surge deposits on top of pyroclastic-flow units. In this fashion, dunes recording crest migration toward the vent are not necessarily antidunes, because their parent flow (the ash cloud) may have been itself flowing toward the vent relative to the underlying pyroclastic flow.

This backflow phenomena is predicted by DASH for only near-vent locations. As radial distance increases, ash clouds may become detached from the parent pyroclastic flow and move unaffected by backflow and also can continue flowing after the pyroclastic flow itself has come to a stop (see discussion by Denlinger 1987). Farther from the vent, and for small eruptions, the inward-flowing wind decreases so that the ash cloud would be able to rise vertically, move entirely according to its own momentum, or be blown by the non-volcanic wind in any direction.

#### Proximal Co-ignimbrite Breccias and the Deflation Zone

##### Previous work

The numerical modeling presented here has important bearing on near-vent processes that produce proximal breccias often observed to be related to ignimbrites. Detailed descriptions of proximal

breccias have been given by Wright and Walker (1977, 1981), Wright (1981), Druitt (1985), Druitt and Sparks (1982), Druitt and Bacon (1986), Bacon (1983), Caress (1985), Kite (1985), and Freundt and Schmincke (1985). Several terms have been used for these deposits and each term corresponds to a specific flow/emplacement mechanism (see below). I use the term "proximal co-ignimbrite breccia" as a nongenetic name for lithic-rich breccias that are found in proximal areas around ignimbrite vents and are laterally equivalent to or associated with ignimbrites. Proximal co-ignimbrite breccias originate by the same eruptive event as their laterally equivalent ignimbrites. This discussion pertains to outflow ignimbrite only, and does not consider intracaldera breccia formation (Lipman 1976).

Proximal co-ignimbrite breccias were first discussed by Wright and Walker (1977) and were termed by them "co-ignimbrite lag-fall" deposits. They were interpreted by Wright and Walker (1977, 1981) to represent deposition of heavy clasts at the site of column collapse. The term "lag-fall" reflects the idea that the breccia material falls from the eruption column and lags behind the remainder of the material that coalesces to form pyroclastic flows. Walker (1985) simplified the term used for these deposits to "lag breccia," and proposed a model whereby the breccias are deposited from a highly expanded, turbulent zone around a collapsing eruption column. This zone, called the "deflation zone," was postulated by Sparks et al. (1978) and Sparks and Walker (1977) to be the site where dense pyroclastic flows are actively segregating from a low-

concentration flow. Druitt and Sparks (1982) observe that coarse, poorly-sorted, clast-supported breccias vertically and laterally grade into ignimbrite, and that the breccias are laterally equivalent to layer 2bL, the lithic concentration zone commonly found near the base of ignimbrite flow units (Sparks et al. 1973). In the above models, sorting of proximal breccias is attributed to gas streaming, analogous to fluidization, during lateral flowage of the material.

The significance of proximal breccias in terms of eruption dynamics has been discussed by Druitt and Sparks (1984), Druitt (1985), and Walker (1985). These workers suggest that the occurrence of proximal breccias within a caldera-forming eruption sequence marks the onset of caldera collapse. In addition, Walker (1985) proposes that variations in the extent of proximal breccias in a given eruption sequence are related to variations in the extent of the deflation zone due to discharge fluctuations. Druitt (1985) suggested that the formation of proximal breccias is at least partly due to overpressured conditions at the vent which enhance vent erosion. He suggests that this condition will be met during periods of rapidly increasing discharge, such as the onset of caldera collapse.

#### Modeling Approach and Results

In order to examine the behavior of various clast Rouse numbers, I have run the DASH code with clast radii ranging from  $10^{-4}$  to  $10^{-1}$  m. To isolate the effects of particle characteristics

alone, experiments were designed to compare eruptions with different particle radii but with identical mixture parameters, so that  $P_n$  was varied while  $T_{gm}$ ,  $R_{im}$ ,  $K_p$ , and  $D_s$  were held constant. Referring to Appendix 3C, the runs discussed here are 8, 40, 43, and 46.

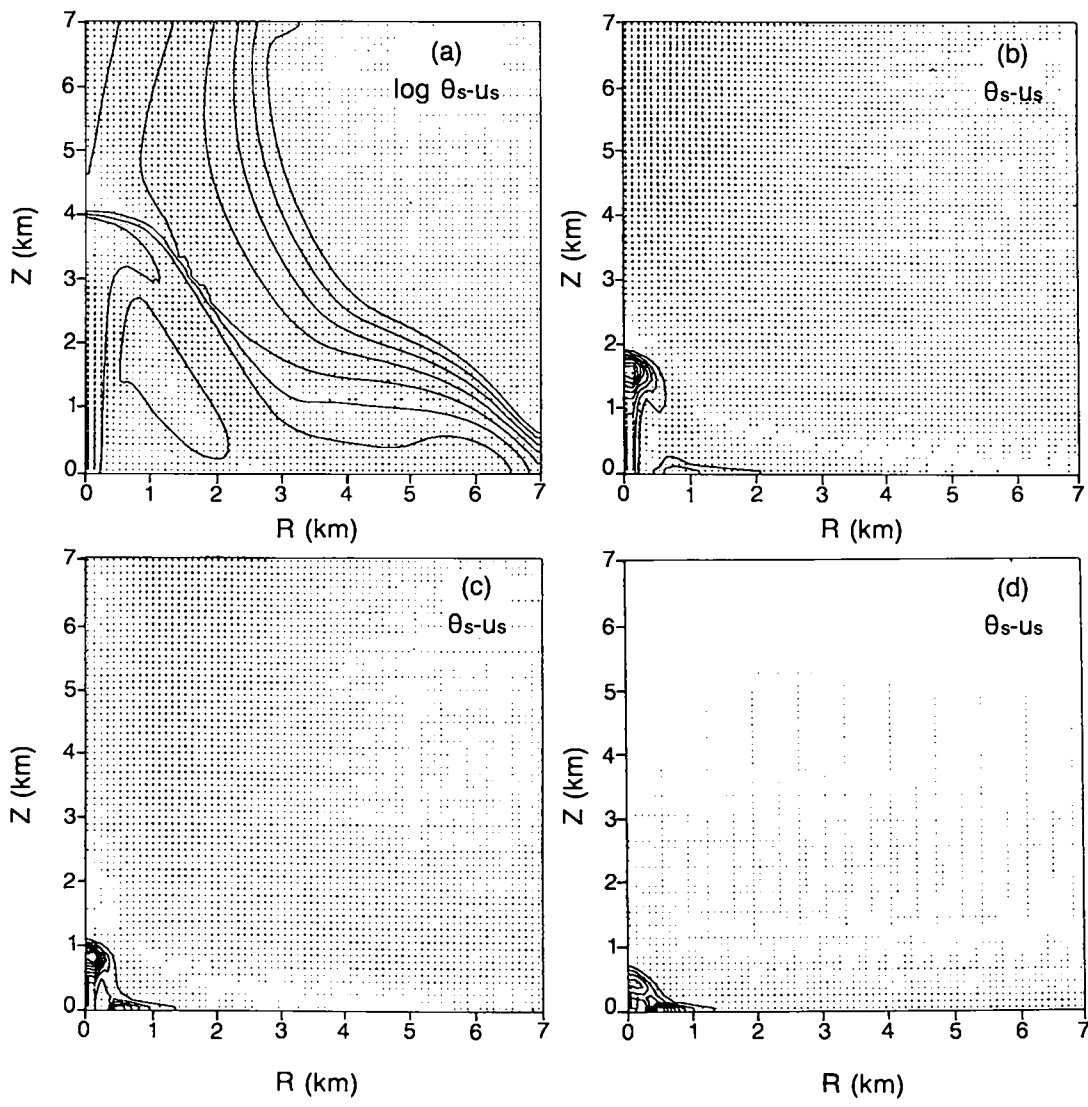
Figure 3-10 shows the  $\theta_s$ -velocity plots for four experiments at late stages of column collapse ( $t = 185$  s). Two general results are illustrated: (1) collapse height varies inversely with  $P_n$ ; and (2) higher- $P_n$  clasts hit the ground much closer to the vent than their finer counterparts. For example, fine ash is transported to about 3.5 km above the vent and falls to the ground at a radial distance of about 2.5 km, while 1 cm radius lapilli moves only to 0.7 km and falls to the ground at about 0.5 km from the vent center. 10 cm lithic fragments return to the ground at only 300 m from the center of the vent. Not surprising from a physical standpoint, these results simply reflect the degree to which particles are coupled with the gas phase in an eruption (see also discussion by Wilson et al. 1987). Very fine particles are nearly perfectly coupled with the gas. They are dragged up much higher before the mixture density causes instability and collapse. Large particles, on the other hand, are barely affected by gas drag, and follow paths that are more nearly ballistic. In reality, large clasts will experience an increased drag force caused by the presence of fine particles suspended in the gas. Thus the results of the present numerical modeling can not be exactly applied to

natural eruptions. Nonetheless, these experiments show the relative effects of varying  $P_n$ , and I feel that the results apply qualitatively to real eruptions. Furthermore, the above results indicate that the sorting observed in proximal breccias is primarily inherited from the eruption column itself, and that gas sorting during lateral flowage is a second order process.

Numerical experiments for all Rouse numbers show the formation of pyroclastic flows that consist of inwardly and outwardly moving parts as was discussed in an earlier section. The finest material involved in collapse will fall to the ground at the largest distance from vent, and all pyroclastic flows outside of this distance will move away from the vent. What happens inside this envelope in a real eruption, however, is not clear. Some backflow of finer material into areas where coarser material is falling will lead to some mixing of the two. On the other hand, very close to the vent, the coarsest material having followed nearly ballistic paths may flow radially outward where it may mix with progressively finer material. During flow away from the vent, coarse clasts become progressively diluted because of two processes: 1) sedimentation out of flow, and 2) mixing with increasing quantities of finer clasts.

This simple analysis of model results can explain most features of proximal co-ignimbrite breccias described by previous authors. Some deposits, especially those extremely close to vent, may be expected to have characteristics of fallout deposits, such

Figure 3-10: Ash volume fraction and velocity plots for eruptions at late time ( $t = 185$  s), demonstrating how pyroclastic-flow dispersal depends upon Rouse number ( $Pn$ ). The only parameter that varies between these eruptions is the particle size. (a)  $\log\theta_S-\vec{u}_S$  plot of Run 8 (same as Figure 3-4), with  $Pn = 0.028$ . Pyroclasts rise to about 3.5 km elevation, and impinge upon the substrate at a distance of about 2.5 km from vent. (b)  $\theta_S-\vec{u}_S$  plot of Run 46,  $Pn = 0.088$ , shows pyroclasts rising only to 1.1 km and impinging upon the ground at 0.6 km from vent center. (c)  $\theta_S-\vec{u}_S$  plot of Run 40,  $Pn = 0.28$ , where material rises to 0.7 km elevation and hits the ground at 0.5 km from vent center. (d)  $\theta_S-\vec{u}_S$  plot of Run 43,  $Pn = 0.88$ , with pyroclasts rising to 0.4 km elevation and hitting the ground at 0.3 km from vent center. Note that only (a) plots contours of  $\log\theta_S$ : (b) - (d) plot straight  $\theta_S$ , since the poor coupling between the gas and solid phases in these runs limits pyroclast dispersal.  $\log\theta_S$  plots of (b) - (d) would only show one contour.



as continuous bedding and good sorting (Wright and Walker 1977, 1981). These deposits would have indeed be true fallout because they simply "piled up" where the material hit the ground. However, the models show that much of the material can continue to flow after falling to the ground, producing discontinuous stratification and mixing with finer and less dense material. In places, coarse-grained flows originating from the vent may move over newly-deposited, finer, pumiceous ash. If the coarse-grained flows are lithic rich, they will be much denser than the underlying ash deposit, and pods and rafts of lithic breccia may sink down into the underlying material (Druitt and Sparks 1982). This situation is expected to enhance degassing of the underlying ash resulting in increased formation of degassing pipes.

Plots of maximum lithic size versus distance from vent commonly show inflection points (Wright and Walker 1977; Wright 1981; Wilson 1985; Druitt and Bacon 1986; Caress 1985). These inflections are suggested by the above authors to mark the outer edge of the postulated deflation zone. In contrast, the DASH models suggest that the inflection simply represents the runout distance of coarse breccia material as defined by its potential energy line (Sheridan 1979). Beyond that point, transport is determined by the pumice flow, which may carry lithics and undergo grading processes as discussed by Sparks (1976) and many other authors.

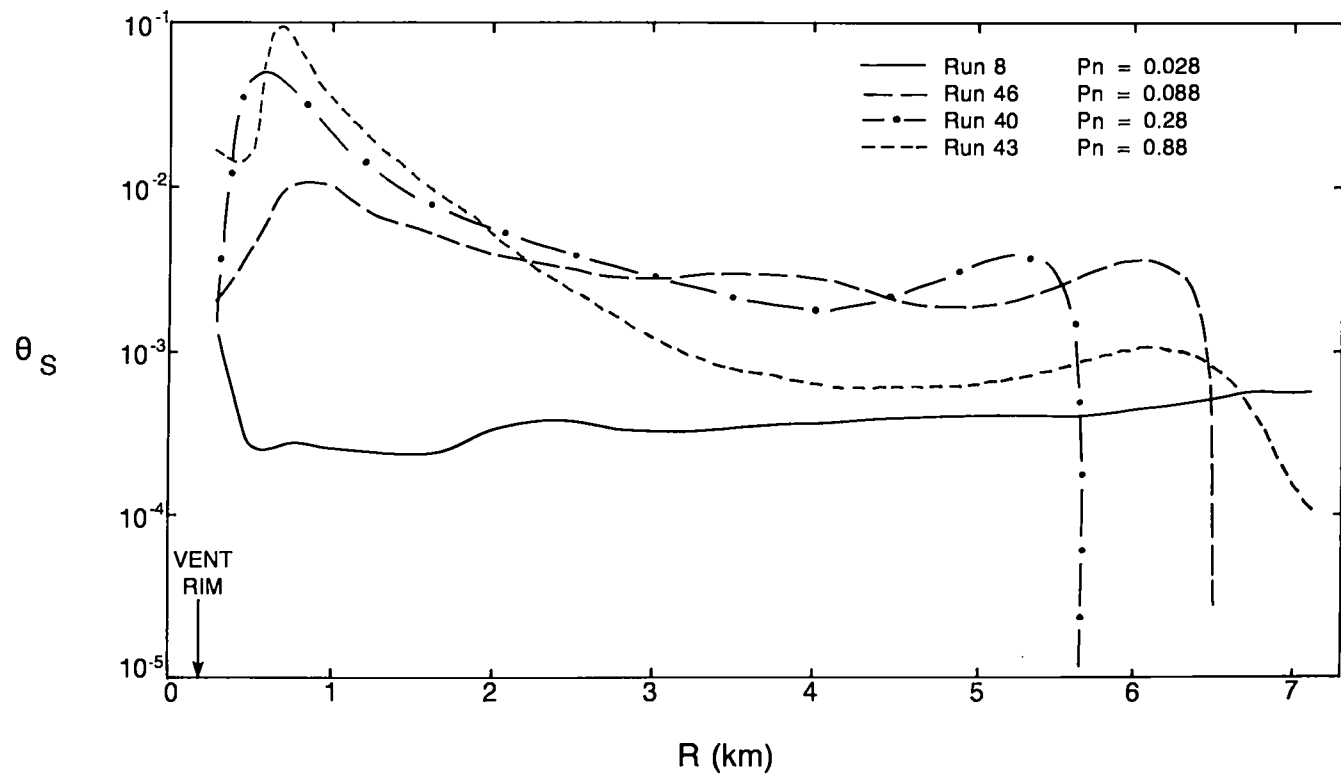
In summary, the main result of the numerical models regarding proximal co-ignimbrite breccias is that the concept of the deflation zone is not supported. In fact, the modeling indicates that the near-vent region will have the highest particle concentration ground flow, as opposed to being very low-concentration as postulated for the deflation zone concept (Figure 3-11).

#### CONCLUSIONS

Numerical models of Plinian eruptions have been made in which the full set of Navier-Stokes equations are separately solved for solid-particle and gas phases in two dimensions. These models provide direct analysis of some basic nonlinear processes active in eruption columns, processes that can not be generally understood by intuitive reasoning alone. The main results of the analysis of 51 numerical experiments are as follows:

1. The most fundamental types of eruption column behavior, high-standing Plinian and collapsing fountain, are determined by the density and velocity of the erupting mixture, the exit pressure, and the vent radius. The critical conditions for eruption column collapse form a surface in  $Tg_m-Ri_m-K_p$  space for eruptions with similar grain size characteristics. Column behavior is more strongly influenced by the ratio of exit pressure to ambient pressure than by the ratio of column density to ambient density within the framework of this numerical model.

Figure 3-11: Solid volume fraction ( $\theta_S$ ) plotted against radial distance from vent center for the model eruptions shown in Figure 3-10 ( $t = 185$  s). Peaks in  $\theta_S$  between 0 - 3 km from vent center correspond to sites where collapsing flow is impinging upon the ground, so that the proximal area is the area of highest pyroclast concentration. This runs contrary to the deflation zone concept. Note that Runs 46, 40, and 43 have each have second maximum in  $\theta_S$  between 5 - 7 km from the vent. These features are associated with the heads of the individual pyroclastic flows.



2. Overpressured eruptions display features that are observed in laboratory experiments of overpressured jets. The erupting mixture initially expands and accelerates above the vent, then compresses and decelerates through a Mach disk shock. This process produces a characteristic diamond-shaped cross section at the base of eruption columns.

3. Pyroclastic flows can consist of two parts. One part flows outward from the vent to form outflow facies tuff, the other part may flow toward the vent and thus result in recycling of erupted material back into the column. Pyroclastic flows produced by the numerical model display a relatively thick head, a thinner body, and a lower-concentration tail. This structure corresponds well with laboratory density currents. In order to flow away from the vent, a pyroclastic flow must have enough momentum to overcome drag of convectively inflowing atmosphere. Insufficient momentum may result in a weak pyroclastic flow eruption with only a towering ash cloud visible to the observer.

4. The numerical experiments suggest that during the beginning stages of eruption column collapse, lower-concentration outer parts of the column may be pushed ahead of higher-concentration parts. When the material impinges on the ground, the result is a pyroclastic flow with a low-concentration front. This may lead to deposition of the ground surge deposit commonly observed beneath pyroclastic flow deposits.

5. Buoyant, low-concentration clouds of ash that rise above fountains and related pyroclastic flows are observed in all eruptions (excepting those in which the particles are very coarse). In proximal areas (within 7 km from vent), the ash clouds typically flow toward the vent relative to the main pyroclastic flow. Deposits from the inflowing ash cloud may show ventward-migrating dunes. In natural eruptions it is likely that the ash cloud may obscure pyroclastic flow processes and lead to misinterpretation of eruption dynamics. It is also expected that fallout deposits may form concurrently with pyroclastic flows, so that caution must be used in interpreting deposits in terms of eruption processes.

6. The model supports an origin of proximal co-ignimbrite breccias by sorting within the eruption column. In this case, coarser clasts collapse from the column at lower elevations and hit the ground closer to the vent than finer clasts. The breccias become finer-grained with distance mainly due to sorting that occurs before hitting the ground instead of during lateral flowage. Lateral flow of all the material spreads the clast size distribution laterally over greater distances than the vertical distribution in the eruption column. It is suggested that the inflection point commonly observed in maximum-lithic-size versus distance-from-vent plots is related to the potential energy line of the breccia material.

7. The numerical model does not support the existence of a "deflation zone" in proximal areas around a fountain, as has been

suggested by previous authors. Instead, pyroclastic flows in this area appear to have a higher concentration than any other location in the computational domain.

APPENDIX 3A: DEFINITION OF NOTATION FOR CHAPTER 3

Symbol	Definition	Dimensions
$\alpha$	Radiation absorptivity	--
$Ar$	Archimedes number, ratio of buoyancy forces to viscous forces	--
$c_m$	Sound speed	$L T^{-1}$
$c_d$	Drag coefficient	--
$c_p$	Heat capacity at constant pressure	$L^2 T^{-2} K^{-1}$
$c_v$	Heat capacity at constant volume	--
$D$	Mass discharge rate of magma	$MT^{-1}$
$D_a$	Ratio of eruption mixture density to atmospheric density	--
$\epsilon$	Radiation emissivity	--
$g$	Gravitational acceleration, directed toward $-z$	$LT^{-2}$
$H$	Elevation of top of eruption column	$L$
$I$	Specific internal energy	$L^2 T^{-2}$
$k$	Thermal conductivity	$MT^{-3} K^{-1}$
$K$	Interphase momentum transfer function	$M^{-3} T^{-1}$
$K_p$	Ratio of vent exit pressure to atmospheric pressure	--
$L$	Characteristic length	$L$
$M$	Mach number, ratio of flow speed to sound speed	--
$m$	Ratio of mass of solid phase per unit volume of mixture to mass of gas phase per unit volume of mixture	--
$p$	Gas pressure	$M L^{-1} T^{-2}$
$\Delta p$	Characteristic pressure change	$M L^{-1} T^{-2}$
$P_n$	Rouse number, ratio of particle settling velocity to vertical flow speed	--
$Pr$	Prandtl number, ratio of momentum diffusivity to thermal diffusivity	--
$q$	Intraphase conductive heat transport	$MT^{-3}$
$Q$	Transport quantity	--

R	Interphase heat transfer	$M^{-1}T^{-3}$
r	Radial distance from symmetry axis	L
$r_s$	Particle radius	L
$R_v$	Vent radius	L
$RI_m$	Richardson number, ratio of inertia to buoyancy in terms of erupting mixture properties	--
$Re$	Reynolds number, ratio of inertia to viscous dissipation	--
t	Time	T
T	Temperature	K
$\Delta T$	Temperature difference between phases $T_s - T_g$	K
$T_{gm}$	Thermogravitational parameter, ratio of pressure driving force to buoyancy	--
u	Radial component of velocity	$LT^{-1}$
$\vec{u}$	Velocity vector	$LT^{-1}$
$\Delta \vec{u}$	Slip velocity $\vec{u}_g - \vec{u}_s$	$LT^{-1}$
v	Axial component of velocity	$LT^{-1}$
$v_e$	Axial (vertical) velocity component at vent exit plane	$LT^{-1}$
$w_s$	Terminal or settling velocity of particles	$LT^{-1}$
z	Axial (vertical) distance above vent exit plane	L
$\epsilon$	Stefan-Boltzmann constant	$MT^{-3}K^{-4}$
$\gamma$	Ratio of specific heats of gas phase	--
$\theta$	Volume concentration of specified phase	--
$\nu$	Momentum diffusivity or kinematic viscosity	$L^2T^{-1}$
$\rho$	Material density of specified phase	$M^{-3}$
$\tau$	Viscous stress tensor	$M^{-1}T^{-2}$

Subscripts

atm atmosphere  
dg dusty-gas  
e conditions at vent exit plane  
g gas (compressible) phase  
l radial computational cell index  
j axial computational cell index  
m mixture  
n time cycle for computation  
s solid (incompressible) phase

---

APPENDIX 3B: MATERIAL PROPERTIES AND VALUES OF PHYSICAL PARAMETERS  
USED IN NUMERICAL EXPERIMENTS

Parameter	Value	Reference
$a_g$	0.9	Flaud et al. [1977]
$c_d$	1.0	Walker et al. [1971]
$c_{vg}$	1406 J/kg·K	Reynolds and Perkins [1977, p. 642]
$c_{vs}$	954 J/kg·K	Riehle [1973]
$c_{pg}$	1867 J/kg·K	Reynolds and Perkins [1977, p. 642]
$e_s$	0.8	CRC Handbook Chem. Phys. [1979, p. E-393]
$g$	9.8 m/s <sup>2</sup>	
$k_g$	0.5 W/m·K	Incropera and DeWitt [1981, p. 779]
$\epsilon$	$5.670 \times 10^{-8}$ W/m <sup>2</sup> ·K <sup>4</sup>	
$\gamma$	1.33	Reynolds and Perkins [1977, p. 642]
$\nu_g$	$1.1 \times 10^{-4}$ m <sup>2</sup> /s	Incropera and DeWitt [1981, p. 779]
$\rho_s^2$	2400 kg/m <sup>3</sup>	

1 This value of  $\nu_g$  is used in Equations 12-14, the heat exchange terms, and in Appendix B.

2 In Runs 50-52,  $\rho_s = 500$  kg/m<sup>3</sup> (pumice).

APPENDIX 3C: EXIT CONDITIONS FOR MODEL ERUPTIONS

Run #	$v_0$ (m/s)	$\theta_0$	$P_0$ (MPa)	$R_0$ (m)	$r_0$ (m)	$\dot{b}$ (kg/s)	$T_{0m}$	$R_{0m}$	$P_n$	$K_p$	$D_a$	$M$	PL/F <sup>1</sup>	$t_0^2$ (Sec)
8	300	10 <sup>-2</sup>	0.1	200	10 <sup>-4</sup>	1.8x10 <sup>9</sup>	0	47.3	2.8x10 <sup>-2</sup>	1.0	33.4	4.7	F	200
10	200	10 <sup>-2</sup>	0.1	200	10 <sup>-4</sup>	6.0x10 <sup>8</sup>	0	21.0	4.2x10 <sup>-2</sup>	1.0	33.4	3.1	F	200
11	100	10 <sup>-2</sup>	0.1	200	10 <sup>-4</sup>	3.0x10 <sup>8</sup>	0	5.3	8.4x10 <sup>-2</sup>	1.0	33.4	1.6	F	200
12	200	10 <sup>-2</sup>	0.1	200	10 <sup>-4</sup>	6.0x10 <sup>8</sup>	0	21.0	4.2x10 <sup>-2</sup>	1.0	33.4	3.1	F	40
13	200	10 <sup>-2</sup>	0.1	200	10 <sup>-4</sup>	6.0x10 <sup>8</sup>	0	21.0	4.2x10 <sup>-2</sup>	1.0	33.4	3.1	F	25
14	200	10 <sup>-2</sup>	0.1	200	10 <sup>-4</sup>	6.0x10 <sup>8</sup>	0	21.0	4.2x10 <sup>-2</sup>	1.0	33.4	3.1	F	15
15	200	10 <sup>-2</sup>	0.1	200	10 <sup>-4</sup>	6.0x10 <sup>8</sup>	0	21.0	4.2x10 <sup>-2</sup>	1.0	33.4	3.1	F	60
16	150	10 <sup>-2</sup>	0.1	200	10 <sup>-4</sup>	4.5x10 <sup>8</sup>	0	11.8	5.6x10 <sup>-2</sup>	1.0	33.4	2.3	F	200
17	250	10 <sup>-2</sup>	0.1	200	10 <sup>-4</sup>	7.5x10 <sup>8</sup>	0	32.9	3.3x10 <sup>-2</sup>	1.0	33.4	3.9	F	200
18	200	10 <sup>-2</sup>	0.1	200	10 <sup>-4</sup>	6.0x10 <sup>8</sup>	0	21.0	4.2x10 <sup>-2</sup>	1.0	33.4	3.1	F	5
19	200	10 <sup>-2</sup>	0.1	200	10 <sup>-4</sup>	6.0x10 <sup>8</sup>	0	21.0	4.2x10 <sup>-2</sup>	1.0	33.4	3.1	F	50
21	300	10 <sup>-2</sup>	0.01	200	10 <sup>-4</sup>	1.8x10 <sup>9</sup>	-2.0	47.3	8.8x10 <sup>-2</sup>	0.1	33.4	14.8	F	200
22	300	10 <sup>-2</sup>	1.0	200	10 <sup>-4</sup>	9.7x10 <sup>8</sup>	18.3	42.2	8.8x10 <sup>-3</sup>	10.0	35.9	1.5	PL	200
23	200	10 <sup>-2</sup>	0.5	200	10 <sup>-4</sup>	6.2x10 <sup>8</sup>	8.5	21.0	1.9x10 <sup>-2</sup>	5.0	34.6	1.4	F	200
24	200	10 <sup>-2</sup>	1.0	200	10 <sup>-4</sup>	6.5x10 <sup>8</sup>	18.3	21.0	1.3x10 <sup>-2</sup>	10.0	35.9	1.0	F	200
25	200	10 <sup>-2</sup>	1.5	200	10 <sup>-4</sup>	6.7x10 <sup>8</sup>	27.6	21.0	1.1x10 <sup>-2</sup>	15.0	37.1	0.8	PL	200
26	200	10 <sup>-2</sup>	2.0	200	10 <sup>-4</sup>	6.9x10 <sup>8</sup>	36.2	21.0	9.3x10 <sup>-3</sup>	20.0	38.3	0.7	PL	200
31	200	5x10 <sup>-2</sup>	0.1	200	10 <sup>-4</sup>	3.0x10 <sup>9</sup>	0	20.5	4.2x10 <sup>-2</sup>	1.0	107.3	7.1	F	200
32	200	10 <sup>-1</sup>	0.1	200	10 <sup>-4</sup>	6.0x10 <sup>9</sup>	0	20.5	4.2x10 <sup>-2</sup>	1.0	334.3	10.3	F	200
33	200	5x10 <sup>-3</sup>	0.1	200	10 <sup>-4</sup>	3.0x10 <sup>8</sup>	0	21.7	4.2x10 <sup>-2</sup>	1.0	17.0	2.2	F	200
34	100	10 <sup>-2</sup>	0.1	300	10 <sup>-4</sup>	6.8x10 <sup>8</sup>	0	3.5	8.4x10 <sup>-2</sup>	1.0	33.4	1.6	F	200
35	200	10 <sup>-2</sup>	0.1	300	10 <sup>-4</sup>	1.4x10 <sup>9</sup>	0	14.0	4.2x10 <sup>-2</sup>	1.0	33.4	3.1	F	200
36	300	10 <sup>-2</sup>	0.1	300	10 <sup>-4</sup>	2.0x10 <sup>9</sup>	0	31.5	2.8x10 <sup>-2</sup>	1.0	33.4	4.7	F	200
37	100	10 <sup>-2</sup>	0.1	200	10 <sup>-2</sup>	3.0x10 <sup>8</sup>	0	5.3	8.4x10 <sup>-1</sup>	1.0	33.4	--	F	200
39	200	10 <sup>-2</sup>	0.1	200	10 <sup>-2</sup>	6.0x10 <sup>8</sup>	0	21.0	4.2x10 <sup>-1</sup>	1.0	33.4	--	F	200
40	300	10 <sup>-2</sup>	0.1	200	10 <sup>-2</sup>	1.8x10 <sup>9</sup>	0	47.3	2.8x10 <sup>-1</sup>	1.0	33.4	--	F	200
41	100	10 <sup>-2</sup>	0.1	200	10 <sup>-1</sup>	3.0x10 <sup>8</sup>	0	5.3	2.6x10 <sup>0</sup>	1.0	33.4	--	F	200

42	200	10 <sup>-2</sup>	0.1	200	10 <sup>-1</sup>	6.0×10 <sup>8</sup>	0	21.0	1.3×10 <sup>0</sup>	1.0	33.4	--	F	200
43	300	10 <sup>-2</sup>	0.1	200	10 <sup>-1</sup>	1.8×10 <sup>9</sup>	0	47.3	8.8×10 <sup>-1</sup>	1.0	33.4	--	F	200
46	300	10 <sup>-2</sup>	0.1	200	10 <sup>-3</sup>	1.8×10 <sup>9</sup>	0	47.3	8.8×10 <sup>-2</sup>	1.0	33.4	--	F	200
47	100	10 <sup>-2</sup>	0.1	200	10 <sup>-3</sup>	3.0×10 <sup>8</sup>	0	5.3	2.6×10 <sup>-1</sup>	1.0	33.4	--	F	200
49	300	10 <sup>-2</sup>	0.69	200	10 <sup>-4</sup>	1.8×10 <sup>9</sup>	12.3	47.3	1.1×10 <sup>-2</sup>	6.9	33.7	1.8	PL	200
50 <sup>3</sup>	300	10 <sup>-2</sup>	0.1	200	10 <sup>-2</sup>	1.9×10 <sup>8</sup>	0	53.3	1.3×10 <sup>-1</sup>	1.0	7.2	--	F	200
51 <sup>3</sup>	300	10 <sup>-2</sup>	0.1	200	10 <sup>-1</sup>	1.9×10 <sup>8</sup>	0	53.3	4.0×10 <sup>-1</sup>	1.0	7.2	--	F	200
52 <sup>3</sup>	300	10 <sup>-2</sup>	0.1	200	10 <sup>-3</sup>	1.9×10 <sup>8</sup>	0	53.3	4.0×10 <sup>-2</sup>	1.0	7.2	--	F	200
53	300	10 <sup>-2</sup>	0.37	200	10 <sup>-4</sup>	1.8×10 <sup>9</sup>	5.7	47.3	1.4×10 <sup>-2</sup>	3.7	36.8	2.4	F	200
54	100	10 <sup>-2</sup>	1.38	300	10 <sup>-4</sup>	7.5×10 <sup>8</sup>	16.9	3.5	2.2×10 <sup>-2</sup>	13.8	36.8	0.4	F	200
55	100	10 <sup>-2</sup>	2.06	300	10 <sup>-4</sup>	7.8×10 <sup>8</sup>	24.7	3.5	1.8×10 <sup>-2</sup>	20.6	36.5	0.3	PL	200
56	300	10 <sup>-2</sup>	1.03	300	10 <sup>-4</sup>	2.2×10 <sup>9</sup>	12.6	31.5	8.7×10 <sup>-3</sup>	10.3	36.0	1.5	PL	200
57	300	10 <sup>-2</sup>	1.38	300	10 <sup>-4</sup>	2.2×10 <sup>9</sup>	16.9	31.5	7.5×10 <sup>-3</sup>	13.8	36.8	1.2	PL	200
58	300	10 <sup>-2</sup>	1.38	300	10 <sup>-1</sup>	2.2×10 <sup>9</sup>	16.9	31.5	2.4×10 <sup>-1</sup>	13.8	36.8	--	F	200
59	300	10 <sup>-2</sup>	0.69	300	10 <sup>-1</sup>	2.1×10 <sup>9</sup>	8.5	31.5	3.4×10 <sup>-1</sup>	6.9	33.7	--	F	200
60	205	3.1×10 <sup>-3</sup>	0.1	100	10 <sup>-4</sup>	4.8×10 <sup>7</sup>	0	47.3	4.1×10 <sup>-2</sup>	1.0	10.5	1.7	F	200
61	73	1.3×10 <sup>-3</sup>	0.1	200	10 <sup>-4</sup>	3.6×10 <sup>7</sup>	0	3.5	1.1×10 <sup>-1</sup>	1.0	4.5	0.4	F	200
62	228	1.6×10 <sup>-3</sup>	0.1	200	10 <sup>-4</sup>	1.2×10 <sup>8</sup>	0	31.5	3.7×10 <sup>-2</sup>	1.0	5.7	1.4	F	200
63	312	2.6×10 <sup>-2</sup>	1.0	200	10 <sup>-4</sup>	2.5×10 <sup>9</sup>	7.2	50.2	8.5×10 <sup>-3</sup>	10.0	69.7	2.5	F	200
64	244	7.0×10 <sup>-3</sup>	0.5	200	10 <sup>-4</sup>	5.4×10 <sup>8</sup>	12.0	31.5	1.5×10 <sup>-2</sup>	5.0	24.6	1.4	F	200
65	202	2.0×10 <sup>-2</sup>	1.0	200	10 <sup>-4</sup>	1.2×10 <sup>9</sup>	9.5	21.0	1.3×10 <sup>-2</sup>	10.0	68.8	1.4	F	200
66	171	9.5×10 <sup>-4</sup>	0.1	100	10 <sup>-4</sup>	1.3×10 <sup>7</sup>	0	21.0	4.9×10 <sup>-2</sup>	1.0	3.4	0.8	F	200
67	128	1.1×10 <sup>-3</sup>	0.2	100	10 <sup>-4</sup>	1.4×10 <sup>7</sup>	36.2	21.0	4.6×10 <sup>-2</sup>	2.0	4.9	0.5	F	200
68	131	1.7×10 <sup>-3</sup>	0.2	100	10 <sup>-4</sup>	1.8×10 <sup>7</sup>	27.5	21.0	4.5×10 <sup>-2</sup>	2.0	6.2	0.6	F	200
69	374	2.1×10 <sup>-2</sup>	1.0	300	10 <sup>-4</sup>	5.6×10 <sup>9</sup>	5.7	47.3	7.1×10 <sup>-3</sup>	10.0	73.8	2.7	PL	200

<sup>1</sup> PL = plinian column, F = fountain (collapsing column).

<sup>2</sup> t<sub>0</sub> = duration of discharge.

<sup>3</sup> In these runs, ρ<sub>g</sub> = 500 kg/m<sup>3</sup> (similar to pumice). In all other runs, ρ<sub>g</sub> = 2400 kg/m<sup>3</sup>.

### APPENDIX 3D: NUMERICAL FORMULATION AND ACCURACY

The numerical representation of the Navier-Stokes equations used in the DASH code is discussed in detail in Harlow and Amsden (1975). The overall technique is very similar to that utilized in the KACHINA code (Amsden and Harlow 1974), which was used by Wohletz et al. (1984), except that in DASH the intraphase heat conduction terms are neglected and a crude turbulence viscosity is used as discussed in the text. The differencing scheme for conservation of mass is explicit for the incompressible (solid) phase and implicit for the compressible (gas) phase. Conservation of internal energy is represented by explicit finite-difference equations (FDE's) for both phases. Conservation of momentum is represented by implicit finite-difference equations for both phases. Below I show the mass and internal energy FDE's, which are relatively simple, and the interested reader is referred to Harlow and Amsden (1975) and Amsden and Harlow (1974) for the more complex FDE form of the momentum equation along with the general solution procedure.

Field variables  $P$ ,  $\theta$ ,  $\rho$ , and  $I$  are defined at cell centers, while velocity components are defined at midpoints of cell edges. Field quantities are transported from cell center to cell center via the donor cell (upwind differencing) technique. In the finite-difference representation of the differential equations given below, indices  $i$  and  $j$  refer to cell-center coordinates in the  $r$  and  $z$  directions, respectively, and superscript  $n$  is the time

cycle. For terms with no time cycle specification, assume cycle n. In addition,  $\delta r$  corresponds to the radial cell dimension,  $\delta z$  to the axial cell dimension, and  $\delta t$  to the time step for computation. As noted in the text, for this work  $\delta r = \delta z = 100$  m and  $\delta t = 0.02$  s. Terms enclosed in angle brackets are subject to the donor-cell condition, which states that

$$\langle urQ \rangle_{i+1/2,j} = (ur)_{i+1/2,j} \cdot \begin{cases} Q_{i,j} & \text{if } u_{i+1/2,j} \geq 0 \\ Q_{i+1,j} & \text{if } u_{i+1/2,j} < 0 \end{cases} \quad (3D-1)$$

where Q is any field variable. This relationship similarly holds for motion in the z-direction.

Equations 3-1a,b, conservation of mass, are approximated as

$$\begin{aligned} & \frac{n+1(\theta_s \rho_s)_{i,j} - n(\theta_s \rho_s)_{i,j}}{\delta t} + \frac{n \langle u_s r \theta_s \rho_s \rangle_{i+1/2,j} - n \langle u_s r \theta_s \rho_s \rangle_{i-1/2,j}}{r_i \delta t} \\ & + \frac{n \langle v_s \theta_s \rho_s \rangle_{i,j+1/2} - n \langle v_s \theta_s \rho_s \rangle_{i,j-1/2}}{\delta z} = 0 \quad (3D-2) \end{aligned}$$

and

$$\begin{aligned} & \frac{n+1(\theta_g \rho_g)_{i,j} - n(\theta_g \rho_g)_{i,j}}{\delta t} \\ & + \frac{n+1 \langle u_g r \theta_g \rho_g \rangle_{i+1/2,j} - n+1 \langle u_g r \theta_g \rho_g \rangle_{i-1/2,j}}{r_i \delta r} \end{aligned}$$

$$+ \frac{n^{+1} \langle v_g \theta_g \rho_g \rangle_{i,j+1/2} - n^{+1} \langle v_g \theta_g \rho_g \rangle_{i,j-1/2}}{\delta z} = 0 \quad (3D-3)$$

for the solid and gas phases, respectively. Next, the specific internal energy equations (3a,b) are approximated by the following FDE's for the solid and gas phase, respectively.

$$\begin{aligned} & \theta_s \rho_s \left\{ \frac{n^{+1} (I_s)_{i,j} - n (I_s)_{i,j}}{\delta t} + \frac{\langle u_s r I_s \rangle_{i+1/2,j} - \langle u_s r I_s \rangle_{i-1/2,j}}{r_i \delta r} \right. \\ & \quad + \frac{\langle v_s I_s \rangle_{i,j+1/2} - \langle v_s I_s \rangle_{i,j-1/2}}{\delta z} \\ & \quad - (I_s)_{i,j} \left[ \frac{(ru_s)_{i+1/2,j} + (ru_s)_{i-1/2,j}}{r_i \delta r} \right. \\ & \quad \quad \left. \left. \frac{(v_s)_{i,j+1/2} - (v_s)_{i,j-1/2}}{\delta z} \right] \right\} \\ & = (R_s)_{i,j} \\ & \quad + (\theta_s \rho_s \nu)_{i,j} \left\{ \left[ \frac{(v_s)_{i-1/2,j+1/2} - (v_s)_{i-1/2,j-1/2}}{\delta r} \right. \right. \\ & \quad \quad \left. \left. + \frac{(u_s)_{i+1/2,j-1/2} - (u_s)_{i-1/2,j-1/2}}{\delta z} \right]^2 \right\} \end{aligned}$$

$$\begin{aligned}
 & + 2 \left[ \frac{(v_s)_{i,j} - (v_s)_{i,j-1}}{\delta z} \right]^2 \\
 & + 2 \left[ \frac{(u_s)_{i,j} - (u_s)_{i-1,j}}{\delta r} \right]^2 \\
 & + \left[ \frac{(u_s)_{i,j} + (u_s)_{i-1,j}}{r_{i-1/2}} \right]^2 \quad (3D-4)
 \end{aligned}$$

$$\begin{aligned}
 & \theta_g \rho_g \left\{ \frac{{}^{n+1}(I_g)_{i,j} - {}^n(I_g)_{i,j}}{\delta t} + \frac{\langle u_g r I_g \rangle_{i+1/2,j} - \langle u_g r I_g \rangle_{i-1/2,j}}{r_i \delta r} \right. \\
 & \quad + \frac{\langle v_g I_g \rangle_{i,j+1/2} - \langle v_g I_g \rangle_{i,j-1/2}}{\delta z} \\
 & \quad - (I_g)_{i,j} \left[ \frac{(ru_g)_{i+1/2,j} + (ru_g)_{i-1/2,j}}{r_i \delta r} \right. \\
 & \quad \quad \left. \left. + \frac{(v_g)_{i,j+1/2} - (v_g)_{i,j-1/2}}{\delta z} \right] \right\} \\
 & = -p_{i,j} \left[ \frac{r_{i+1/2}(\theta_g u_g + \theta_s u_s)_{i+1/2,j}}{r_i \delta r} \right. \\
 & \quad - \frac{r_{i-1/2}(\theta_g u_g + \theta_s u_s)_{i-1/2,j}}{r_i \delta r} \\
 & \quad \left. + \frac{(\theta_g v_g + \theta_s v_s)_{i,j+1/2}}{\delta z} - \frac{(\theta_g v_g + \theta_s v_s)_{i,j-1/2}}{\delta z} \right]
 \end{aligned}$$

$$\begin{aligned}
 &+ (R_g)_{i,j} \\
 &+ |(k_g)_{i,j}| \cdot \left\{ [(u_g)_{i,j} - (u_s)_{i,j}]^2 \right. \\
 &\quad \left. + [(v_g)_{i,j} - (v_s)_{i,j}]^2 \right\} \\
 &+ (\theta_g \rho_g \nu)_{i,j} \left\{ \left[ \frac{(v_g)_{i-1/2,j+1/2} - (v_g)_{i-1/2,j-1/2}}{\delta r} \right. \right. \\
 &\quad \left. \left. + \frac{(u_g)_{i+1/2,j-1/2} - (u_g)_{i-1/2,j-1/2}}{\delta z} \right]^2 \right. \\
 &\quad + 2 \left[ \frac{(v_g)_{i,j} - (v_g)_{i,j-1}}{\delta z} \right]^2 \\
 &\quad + 2 \left[ \frac{(u_g)_{i,j} - (u_g)_{i-1,j}}{\delta r} \right]^2 \\
 &\quad \left. + \left[ \frac{(u_g)_{i,j} + (u_g)_{i-1,j}}{r_{i-1/2}} \right]^2 \right\} \quad (3D-5)
 \end{aligned}$$

In these formulations variables that are indexed such that they are at positions other than their defined locations (cell centers for field variables and midpoints of cell edges for velocity components) are computed by extrapolation and averaging.

The DASH code was tested for accuracy by repeating Run 60 with three different values of cell dimension ( $\delta r$ ,  $\delta z$ ) and time step ( $\delta t$ ). Table 3D-1 presents values of  $u_g$ ,  $\theta_s$ , and  $p$  at elevations of 500 m, 1000 m, 2000 m, and 3000 m on the symmetry

axis at eruption time  $t = 10$  s. At  $t = 10$  s the calculations have gone through 500 to 2000 time cycles so that flaws in the numerical scheme should be apparent. As time progresses values of flow parameters are expected to diverge somewhat for different cell dimensions and time steps due to the nonlinear nature of the equations. For example, at a given (eruption) time a point in the computational domain will have a slightly different value if the time step has a value  $\delta t = 0.02$  s than it would if the same computation was carried out with  $\delta t = 0.01$  s. No matter how precise the numerical scheme the subsequent values of flow parameters at the point for the two time steps may or may not diverge in a predictable way due simply to the nonlinearity of the Navier-Stokes equations. This is a common feature of fluid-dynamical systems (the unpredictability of weather is a good example), and, in my opinion, indicates that comparison of numerical results at late times or large flow distances is not reliable for evaluating numerical schemes. This is the justification for only comparing numbers at early to intermediate times along the symmetry axis. A more detailed discussion of the data in Table 3D-1 follows. Suffice it to say that at late times the graphical (or qualitative) output of the runs in the table are almost identical and that all flow parameters remain within the same order of magnitude for the different  $\delta r, z$ 's and  $\delta t$ 's.

The data in Table 3D-1 show that at a given  $\delta r, z$  the calculations are relatively insensitive to  $\delta t$ . For example, in the

Table 3D-1: Values of  $u_g$ ,  $\theta_s$  and  $p$  at three elevations on the symmetry axis using different mesh size ( $\delta r, z$ ) and time step ( $\delta t$ ). All values are at  $t=10.0$  s.

	$\delta r, z$ $\delta t$	100m 0.02s	100m 0.01s	100m 0.005s	50m 0.01s	50m 0.02s
z=500m	$u_g$ (m/s)	171.3	171.4	171.4	177.7	177.6
	$\theta_s$	$3.09 \times 10^{-3}$	$3.09 \times 10^{-3}$	$3.09 \times 10^{-3}$	$3.00 \times 10^{-3}$	$3.00 \times 10^{-3}$
	$p$ (MPa)	0.096	0.096	0.096	0.097	0.097
z=1000m	$u_g$ (m/s)	138.6	138.8	138.9	145.1	144.8
	$\theta_s$	$3.25 \times 10^{-3}$	$3.24 \times 10^{-3}$	$3.24 \times 10^{-3}$	$3.03 \times 10^{-3}$	$3.03 \times 10^{-3}$
	$p$ (MPa)	0.095	0.095	0.095	0.094	0.094
z=2000m	$u_g$ (m/s)	36.7	36.9	36.9	30.0	29.4
	$\theta_s$	$6.52 \times 10^{-6}$	$7.0 \times 10^{-6}$	$7.23 \times 10^{-6}$	$1.59 \times 10^{-9}$	$1.1 \times 10^{-9}$
	$p$ (MPa)	0.090	0.090	0.090	0.089	0.89
z=3000m	$u_g$ (m/s)	7.3	7.3	7.3	8.3	8.3
	$\theta_s$	$1 \times 10^{-10}$				
	$p$ (MPa)	0.082	0.082	0.082	0.082	0.082

runs where  $\delta r, z = 100$  m the values of  $u_g$  vary only by 0.5% at  $z = 2000$  m (relative to the value when  $\delta t = 0.02$  s) and variations in  $p$  are negligible;  $\theta_s$  varies by about 11% but remains within the same order of magnitude. Similarly, for the two runs where  $\delta r, z = 50$  m the flow parameters vary only slightly between the two  $\delta t$ 's. This relative insensitivity to  $\delta t$  is expected from the Courant criterion, which states that  $\delta r/\delta t$  and  $\delta z/\delta t$  must be at least as large as the highest possible velocity in the flow field. In the case of  $\delta r, z = 100$  m and  $\delta t = 0.02$  s the calculations are stable for flow speeds up to 5000 m/s, which is much larger than any velocities in the present problem. Decreasing the time step merely increases the maximum computable flow speed with very little effect on accuracy.

The data in Table 3D-1 show some sensitivity to the choice of  $\delta r, z$ . This is mainly the result of numerical diffusion; a larger cell dimension will tend to diffuse gradients of flow variables relative to a small cell dimension (Hirt 1968). Compare the values of  $\theta_s$  at  $z = 1000$  m for runs with  $\delta r, z = 100$  m and with  $\delta r, z = 50$  m. The variation between the two cell sizes is relatively small (about 7%, but within the same order of magnitude). In contrast, the values of  $\theta_s$  at  $z = 2000$  m show a large variation between  $\delta r, z = 100$  m and  $\delta r, z = 50$  m. This is explained by the fact that the flow front is between the two elevations, but is better resolved as a sharp front in the runs with smaller cell size. The goal of the present modeling was to study large-scale processes within the flow

field, so that the slight loss in resolution from using  $\delta r, z = 100$  m instead of a smaller value was balanced by the gain in computational speed and hence the lower cost.

### APPENDIX 3E: SCALING OF VISCOUS FORCES AND HEAT CONDUCTION

#### Scaling of Viscous Effects

Viscous effects have been omitted from the discussion of dimensionless parameters and the significance of those parameters with respect to eruption dynamics. As shown here, viscous forces are negligible compared to the other forces represented in Equations 3-13,14,15.

I apply the pseudogas (or dusty-gas) approximation to the flows in order to calculate an effective kinematic viscosity (Marble 1970):

$$\nu_{dg} = \frac{\nu_g}{1 + m} \quad , \quad (3E-1)$$

where  $\nu_g$  is given in Appendix 3B, and  $m$  is the mass ratio of solids to gas. In the numerical experiments,  $\theta_s$  ranges from  $10^{-1}$  to  $10^{-3}$  at the exit plane, corresponding to  $m$  between 1500 and 10. Values of  $\nu_{dg}$  vary accordingly from about  $7 \times 10^{-8}$  to  $7 \times 10^{-6}$  m<sup>2</sup>/s. To determine the relative importance of viscosity, I form ratios with inertial, buoyancy, and thermodynamic forces.

The ratio of inertial forces to viscous forces is given by the Reynolds number (Re) in the following form,

$$Ry = \frac{u L}{\nu_{dg}} \quad , \quad (3E-2)$$

where  $u$  and  $L$  are the characteristic velocity and length, respectively. I take  $u \sim 100$  m/s and  $L \sim 100$  m. Thus for the range of  $\theta_s$  in this work, we have  $Ry \sim 10^{12}$  to  $10^{10}$ , which demonstrates that viscous forces are negligible compared to inertial forces.

The ratio of buoyancy forces to viscous forces forms the Archimedes number (Ar), given by

$$Ar = \frac{(Ds - 1)gL^3}{Ds^2 \nu_{dg}^2} \quad . \quad (3E-3)$$

For the range of conditions considered in this work, the smallest value of the Archimedes number is  $Ar \sim 10^{16}$ , showing that viscous forces are also negligible compared to buoyancy forces.

A ratio of thermodynamic (pressure) forces to viscous forces is given by

$$\frac{L^2(\Delta p)}{\rho_m \nu_{dg}^2} \sim 10^{15} \quad , \quad (3E-4)$$

where  $\Delta p$  is a characteristic pressure change, taken as  $\Delta p \sim 0.1$  MPa. Thus it is clear that the true viscosity of the flows plays a negligible role in the dynamics relative to other types of forces. This justifies the neglect of viscous forces throughout the chapter.

### Scaling of Intrapphase Heat Conduction

Intrapphase heat conduction (heat conduction within individual phases) is not computed in the numerical model used for this work. To justify this, I examine the magnitude of conductive heat transport relative to other forms of heat transport in Equation 3-3a,b. Since the solid phase is treated as dispersed particles, intraphase heat conduction is irrelevant. The gas phase, however, is continuous and requires an order of magnitude estimate of heat conduction. For this purpose we have

$$q = k_g \frac{dT}{dz} \quad , \quad (3E-5)$$

where the direction of heat transport is irrelevant. For a typical temperature gradient of 1 K/m (or 100 K per computational cell) and  $k_g$  from Appendix 3B, we get  $q \sim 0.5 \text{ W/m}^2$ . The ratio of advective heat transport to conduction is

$$\frac{u(\rho_g c_{vg} T_g)}{q} \sim 10^7 \quad , \quad (3E-6)$$

where  $u \sim 100$  m/s,  $\rho_g \sim 0.1$  kg/m<sup>3</sup>, and  $T_g \sim 100$  K. The ratio of energy transport due to pressure changes (work) to conduction is

$$\frac{pu/L}{q} \sim 10^6 \quad (3E-7)$$

for  $P \sim 0.1$  MPa. The ratio of interphase heat transfer to intraphase conduction is

$$\frac{R_s L}{q} \sim 10^{10} \quad (3E-8)$$

for velocity and temperature differences ( $\Delta u$  and  $\Delta T$ ) between particles and gas of 10 m/s and 10 K, respectively,  $\theta_s = 10^{-2}$ , and  $r = 10^{-4}$  m. Finally, the transfer of energy from interphase drag is proportioned to conductive transfer as

$$\frac{K_s (\Delta u)^2 L}{q} \sim 10^8 \quad (3E-9)$$

Thus it is shown that intraphase heat conduction in the gas is negligible compared to the other energy transport mechanisms.

REFERENCES

- Allen JRL (1970) Physical processes of sedimentation. Allen and Unwin Publ Co, London, pp 189-192
- Amsden AA, Harlow FH (1974) KACHINA: An Eulerian computer program for multifield fluid flows. Los Alamos Nat Lab Rep LA-5680
- Bacon CR (1983) Eruptive history of Mount Mazama and Crater Lake Caldera, Cascade Range, USA. J Volcanol Geotherm Res 18: 57-115
- Bagnold RA (1956) Flow of cohesionless grains in fluids. Phil Trans R Soc London Ser A 255: 235-297
- Bird RB, Stewart WE, Lightfoot EN (1960) Transport phenomena. John Wiley and Sons New York, 780 pp
- Blandford RD, Rees MF (1974) A 'twin-exhaust' model for double radio sources. Monthly Not R Astron Soc 169: 395-415
- Borisov AA, Lyubimov AV, Kogarko SM, Kozenko VP (1967) Instability of the surface of a granular medium behind a sliding shock. Comb Expl Shock Waves 3: 149-151
- Brown GL, Roshko A (1974) On density effects and large structure in turbulent mixing layers. J Fluid Mech 64: 775-816
- Buesch DC, Valentine GA (1986) Peach Springs Tuff and volcanic stratigraphy of the southern Cerbat Mountains, Kingman, Arizona. In: Nielson JE, Glazner AF (eds) Cenozoic stratigraphy, structure, and mineralization in the Mojave Desert. Geol Soc Am Guidebook and Volume, Cordilleran Section, pp. 7-14
- Campbell CS, Brennen C.E. (1985) Computer simulation of granular shear flows. J Fluid Mech 151: 167-188

- Caress ME (1985) Volcanology of the Youngest Toba Tuff, Sumatra.  
Unpub PhD dissertation, Univ Hawaii
- Carey S, Sparks RSJ (1986) Quantitative models of the fallout and dispersal of tephra from volcanic eruption columns. Bull Volcanol 48: 127-141
- Carrier GF (1958) Shock waves in a dusty gas. J Fluid Mech 4: 376-382
- Cas RAF, Wright JV (1987) Volcanic successions: Modern and ancient. Allen and Unwin Publ Co, London, 528 pp
- CRC handbook of chemistry and physics 60<sup>th</sup> edition (1979) p E-393. The Chemical Rubber Publ Co, Boca Raton (Florida)
- Criswell CW (1987) Chronology and pyroclastic stratigraphy of the May 18, 1980, eruption of Mount St. Helens, Washington. J Geophys Res 92: 10237-10266
- Crowe BM, Fisher RV (1973) Sedimentary structures in base-surge deposits with special reference to cross-bedding, Ubehebe Craters, Death Valley, California. Geol Soc Am Bull 84: 663-682
- Delvigne GAL (1986) Model for vertical diffusion in stratified flows. J Hydraulics Div: ASCE 112: 1069-1086
- Denlinger RP (1987) A model for generation of ash clouds by pyroclastic flows, with application to the 1980 eruptions at Mount St. Helens, Washington. J Geophys Res 92: 10284-10298
- Dingman SL (1984) Fluvial hydrology. WH Freeman and Co. New York, pp 105, 166-173

- Dokka RK (1983) Displacement on late Cenozoic strike slip faults in the central Mojave Desert, California. *Geology* 11: 305-308
- Dokka RK (1986) Patterns and modes of early Miocene crustal extension, central Mojave Desert, California. *Geol Soc Am Sp Pap* 208: 75-95
- Druitt TH (1985) Vent evolution and lag breccia formation during the Cape Riva eruption of Santorini, Greece. *J Geol* 93: 439-454
- Druitt TH, Bacon CR (1986) Lithic breccia and ignimbrite erupted during the collapse of Crater Lake caldera, Oregon. *J Volcanol Geotherm Res* 29: 1-32
- Druitt TH, Sparks RSJ (1982) A proximal ignimbrite breccia facies on Santorini, Greece. *J Volcanol Geotherm Res* 13: 147-171
- Druitt TH, Sparks RSJ (1984) On the formation of calderas during ignimbrite eruptions. *Nature* 310: 679-681
- Eichelberger JC, Carrigan CR, Westrich HR, Price RH (1986) Non-explosive silicic volcanism. *Nature* 323: 598-602
- Fisher RV (1979) Models for pyroclastic surges and pyroclastic flows. *J Volcanol Geotherm Res* 6: 305-318
- Fisher RV (1983) Flow transformations in sediment gravity flows. *Geology* 11: 273-274
- Fisher RV (1986) Systems of transport and deposition within pyroclastic surges: Evidence from Mount St. Helens, Washington. *EOS Trans Am Geophys Union* 67: 1246

- Fisher RV, Heiken G (1982) Mt. Pelee, Martinique: May 8 and 20, 1902 pyroclastic flows and surges. *J Volcanol Geotherm Res* 13: 339-371
- Fisher RV, Schmincke H-U (1984) *Pyroclastic rocks*. Springer-Verlag Berlin Heidelberg, 472 pp
- Fisher RV, Waters AC (1970) Base surge bed forms in maar volcanoes. *Am J Sci* 268: 157-180
- Fisher RV, Glicken HX, Hoblitt RP (1987) May 18, 1980, Mount St. Helens deposits in South Coldwater Creek, Washington. *J Geophys Res* 92: 10267-10,283
- Flaud JM, Peyret CC, Maillard JP, Guelachvili G (1977) The H<sub>2</sub>O spectrum between 4200 and 5000 cm<sup>-1</sup>. *J Mol Spectro* 65: 219-228
- Freundt A, Schmincke H-U (1985) Lithic-enriched segregation bodies in pyroclastic flow deposits of Laacher See volcano (East Eifel, Germany). *J Volcanol. Geotherm Res* 25: 193-224
- Freundt A, Schmincke H-U (1986) Emplacement of small-volume pyroclastic flows at Laacher See (East-Eifel, Germany). *Bull Volcanol* 48: 39-59
- Ghosh JK, Mazumder BS, Saha MR, Sengupta S (1986) Deposition of sand by suspension currents: Experimental and theoretical studies. *J Sed Pet* 56: 57-66
- Glazner AF, Nielson JE, Howard KA, Miller DM (1986) Correlation of the Peach Springs Tuff, a large-volume Miocene ignimbrite sheet in California and Arizona. *Geology* 14: 840-843

- Goff FE, Eddy AC, Arney BH (1983) Reconnaissance geologic strip map from Kingman to south of Bill Williams Mountain, Arizona. Los Alamos National Laboratory LA-9202-MAP
- Gusa S, Nielson JE, Howard KA (1987) Heavy-mineral suites confirm the wide extent of the Peach Springs Tuff in California and Arizona, USA. *J Volcanol Geotherm Res* 33: 343-347
- Hampton MA (1972) The role of subaqueous debris flow in generating turbidity currents. *J Sed Pet* 42: 775-793
- Harlow FH, Amsden AA (1975) Numerical calculation of multiphase fluid flow. *J Comp Phys* 17: 19-52
- Heiken G, Wohletz K (1985) *Volcanic Ash*. University of California Press Berkely Los Angeles London, pp 113-117
- Hildreth W (1987) New perspectives on the eruption of 1912 in the Valley of Ten Thousand Smokes, Katmai National Park, Alaska. *Bull Volcanol* 49: 680-693
- Hirt CW (1968) Heuristic stability theory for finite-difference equations. *J Comp Phys* 2: 339-355
- Hoblitt RP, Miller DC (1984) Comment on "Mount St. Helens 1980 and Mount Pelee 1902--Flow or surge?" *Geology* 12: 692-693
- Hoblitt RP, Miller DC, Vallance JE (1981) Origin and stratigraphy of the deposits produced by the May 18 directed blast. In: Lipman PW, Mullineaux DR eds. *The 1980 eruptions of Mount St. Helens, Washington*, USGS Prof Pap 1250: 401-419
- Horn M (1986) Physical models of pyroclastic clouds and fountains. Unpub MS thesis, Arizona State Univ

- Houghton BF, Schmincke H-U (1986) Mixed deposits of simultaneous Strombolian and phreatomagmatic volcanism: Rothenberg volcano, East Eifel volcanic field. *J Volcanol Geotherm Res* 30: 117-130
- Howard KA, John BE (1987) Crustal extension along a rooted system of imbricate low-angle faults: Colorado River extensional corridor, California and Arizona. In: Coward MP, Dewey JF, Hancock PL (eds) *Continental Extensional Tectonics*. *Geol Soc Am Sp Pub* 28: 299-311
- Hwang CC (1986) Initial stages of the interaction of a shock wave with a dust deposit. *Int J Multiphase Flow* 12: 655-666
- Incropera FP, DeWitt DP (1981) *Fundamentals of heat transfer*. John Wiley and Sons, New York, 819 pp
- Ingram RL (1954) Terminology for the thickness of stratification and parting units in sedimentary rocks. *Geol Soc Am Bull* 65: 937-938
- Ishii R, Umeda Y, Kawasaki K (1987) Nozzle flows of gas-particle mixtures. *Phys Fluids* 30: 752-760
- Jakosky BM (1986) Volcanoes, the stratosphere, and climate. *J Volcanol Geotherm Res* 28: 247-255
- Jobson HE, Sayre WW (1970) Vertical transfer in open channel flow. *J Hydraulics Div: ASCE* 96: 703-724
- Joint Army, Navy, NASA, Air Force JANNAF (1975) *Handbook of rocket exhaust plume technology*. Chem Prop Info Agency Publ 263, 237 pp.

- Jopling AV, Walker RG (1968) Morphology and origin of ripple-drift cross-lamination, with examples from the Pleistocene of Massachusetts. *J Sed Pet* 38: 971-984
- Karl HA, Cacchione DA, Carlson PR (1986) Internal-wave currents as a mechanism to account for large sand waves in Navarinsky Canyon head, Bering Sea. *J Sed Pet* 56: 706-714
- Kennedy JF (1963) The mechanics of dunes and antidunes in erodible-bed channels. *J Fluid Mech* 30: 741-773
- Kieffer SW (1981) Fluid dynamics of the May 18 blast at Mount St. Helens. In: Lipman PW, Mullineaux DR eds. *The 1980 eruptions of Mount St. Helens, Washington*, USGS Prof Pap 1250: 379-400
- Kieffer SW (1982) Dynamics and thermodynamics of volcanic eruptions: Implications for the plumes on Io. In: Morrison D (ed) *Satellites of Jupiter*, Univ Arizona Press, Tucson, pp 647-723
- Kieffer SW (1984) Factors governing the structure of volcanic jets. In *Explosive volcanism: Inception, Evolution, and Hazards*, National Academy Press, Washington, pp 143-157
- Kieffer SW, Sturtevant B (1984) Laboratory studies of volcanic jets. *J Geophys Res* 89: 8253-8268
- Kieffer SW and Sturtevant B (1986) Erosional furrows formed during the lateral blast at Mount St. Helens, May 18, 1980: Indicators of longitudinal vortices in the boundary layer. *Abstr Intl Volcanol Cong, New Zealand*: p. 53

- Kite WM (1985) Caldera-forming eruption sequences and facies variations in the Bandelier Tuff, central New Mexico. Unpubl MS thesis, Arizona State Univ
- Liepmann HW, Roshko A (1957) Elements of gas dynamics. John Wiley and Sons, Inc. New York, pp. 338-340
- Lin J-T, Pao Y-H (1979) Wakes in stratified fluids. Ann Rev Fluid Mech 11: 317-338
- Lipman PW (1976) Caldera-collapse breccias in the western San Juan Mountains, Colorado. Geol Soc Am Bull 87: 1297-1410
- Lipman PW (1986) Emplacement of large ash-flow sheets and relation to caldera collapse. Abstr Intl Volcanol Cong, New Zealand, p 58
- Lipman PW, Steven TA, Luedke RG, Burbank WS (1973) Revised volcanic history of the San Juan, Uncompahgre, Silverton, and Lake City calderas in the western San Juan Mountains, Colorado. US Geol Survey J Res 1: 627-642
- Marble FE (1970) Dynamics of dusty gases. Ann Rev Fluid Mech 2: 397-446
- McPhie J (1986) Primary and redeposited facies from a large-magnitude, rhyolitic, phreatomagmatic eruption: Cana Creek Tuff, late Carboniferous, Australia. J Volcanol Geotherm Res 28: 319-350
- Middleton GV, Southard JB (1978) Mechanics of sediment movement. Soc Econ Paleontol Mineral Short Course 3, Eastern Section: pp 6.37-41

- Moore JG (1967) Base surge in recent volcanic eruptions. Bull Volcanol 30: 337-363
- Morton BR, Taylor GI, Turner JS (1956) Turbulent gravitational convection from maintained and instantaneous sources. Philos Trans R Soc London Ser A 234: 1-23
- Norman ML, Smarr L, Winkler KHA, Smith MD (1982) Structure and dynamics of supersonic jets. Astron Astrophys 113: 285-302
- Prandtl L (1949) The essentials of fluid mechanics. Blackie and Son Ltd, London
- Reynolds WC, Perkins HC (1977) Engineering thermodynamics. McGraw Hill Book Co, New York, 690 pp
- Richards K (1982) Rivers, form and process in alluvial channels. Methuen & Co. Ltd. London, p 87
- Riehle JR (1973) Calculated compaction profiles of rhyolitic ash-flow tuffs. Geol Soc Am Bull 84: 2193-2216
- Rose WI, Chesner CA (1987) Dispersal of ash in the great Toba eruption, 75 ka. Geology 15: 913-917
- Rudinger G (1964) Some properties of shock relaxation in gas flows carrying small particles. Phys Fluids 7: 658-663
- Savage SB (1984) The mechanics of rapid granular flows. Adv Applied Mech 24: 289-366
- Schlichting H (1979) Boundary-layer theory, 7th edition. McGraw-Hill Book Co. New York, pp 512-513, 715-723

- Schmincke H-U, Fisher RV, Waters AC (1973) Antidune and chute and pool structures in the base surge deposits of the Laacher See area, Germany. *Sedimentology* 20: 553-574
- Self S (1983) Large-scale phreatomagmatic silicic volcanism: A case study from New Zealand. *J Volcanol Geotherm Res* 17: 433-469
- Self S, Sparks RSJ (1978) Characteristics of widespread pyroclastic deposits formed by the interaction of silicic magma and water. *Bull Volcanol* 41: 196-212
- Settle M (1978) Volcanic clouds and the thermal output of explosive eruptions. *J Volcanol Geotherm Res* 3: 309-324
- Sheppard PA (1956) Airflow over mountains. *Qu J R Met Soc* 82: 528-529
- Sheridan MF (1979) Emplacement of pyroclastic flows: A review. *Geol Soc Am Sp Pap* 180: 125-136
- Sigurdsson H, Carey SN, Fisher RV (1987) The 1982 eruption of El Chichon volcano, Mexico (3): Physical properties of pyroclastic surges. *Bull Volcanol* 49: 467-488
- Smith RL (1960) Zones and zonal variations in welded ash flows. *US Geol Surv Prof Pap* 354-F
- Smith RL (1979) Ash-flow magmatism. *Geol Soc Am Sp Pap* 180: 5-27
- Snyder WH, Thompson RS, Eskridge RE, Lawson RE, Castro IP, Lee JT, Hunt JCR, Ogawa Y (1985) The structure of strongly stratified flow over hills: dividing-streamline concept. *J Fluid Mech* 152: 249-288

- Sparks RSJ (1976) Grain size variations in ignimbrites and implications for the transport of pyroclastic flows. *Sedimentology* 23: 147-188
- Sparks RSJ (1978) Gas release rates from pyroclastic flows: An assessment of the role of fluidisation in their emplacement. *Bull Volcanol* 41: 1-9
- Sparks RSJ (1986) The dimensions and dynamics of volcanic eruption columns. *Bull Volcanol* 48: 3-16
- Sparks RSJ, Walker GPL (1973) The ground surge deposit--A third type of pyroclastic rock. *Nature, Phys Sci* 241: 62-64
- Sparks RSJ, Walker GPL (1977) The significance of vitric-enriched air-fall ashes associated with crystal-enriched ignimbrites. *J Volcanol Geotherm Res* 2: 329-341
- Sparks RSJ, Wilson L (1976) A model for the formation of ignimbrite by gravitational column collapse. *J Geol Soc London* 132: 441-451
- Sparks RSJ, Wilson L (1982) Explosive volcanic eruptions - V. Observations of plume dynamics during the 1979 Soufriere eruption, St. Vincent. *Geophys J R Astron Soc* 69: 551-570
- Sparks RSJ, Self S, Walker GPL (1973) Products of ignimbrite eruption. *Geology* 1: 115-118
- Sparks RSJ, Wilson L, Hulme G (1978) Theoretical modeling of the generation, movement and emplacement of pyroclastic flows by column collapse. *J Geophys Res* 83: 1727-1739
- Steven TA, Lipman PW (1976) Calderas of the San Juan volcanic field, southwestern Colorado. *US Geol Surv Prof Pap* 958

- Stewart HB, Wendroff B (1984) Two-phase flow: Models and methods.  
J Comp Phys 56: 363-409
- Taylor GA (1958) The 1951 eruption of Mount Lamington, Papua. Austr  
Bur Min Resour Geol Geophys Bull 38: 1-117
- Tennekes H, Lumley JL (1972) A first course in turbulence. MIT  
Press, Cambridge (Massachusetts), 300 pp
- Thomas DG (1964) Periodic phenomena observed with spherical  
particles in horizontal pipes. Science 144: 534-536
- Thorson JP (1971) Igneous Petrology of the Oatman District, Mojave  
County, Arizona. Unpub PhD dissertation, Univ Calif Santa  
Barbara
- Valentine GA (1987) Stratified flow in pyroclastic surges. Bull  
Volcanol 49: 616-631
- Valentine GA, Fisher RV (1986) Origin of layer 1 deposits in  
ignimbrites. Geology 14: 146-148
- Valentine GA, Wohletz KH (1987) Significance of exit pressure in  
plinian eruptions. EOS Trans Am Geophys Union 68: 1535
- Waite RB Jr. (1981) Devastating pyroclastic density flow and  
attendant air fall of May 18--Stratigraphy and sedimentology of  
the deposits. In: Lipman PW, Mullineaux DR, eds. The 1980  
eruptions of Mount St. Helens, Washington, USGS Prof Pap 1250:  
439-458
- Waite RB Jr. (1984) Comments on "Mount St. Helens 1980 and Mt. Pelee  
1902--Flow or surge?" Geology 12: 693

- Walker GPL (1983) Ignimbrite types and ignimbrite problems. J  
Volcanol Geotherm Res 17: 65-88
- Walker GPL (1984) Characteristics of dune-bedded pyroclastic surge  
bedsets. J Volcanol Geotherm Res 20: 281-296
- Walker GPL (1985) Origin of coarse lithic breccias near ignimbrite  
source vents. J Volcanol Geotherm Res 25: 157-171
- Walker GPL, McBroome LA (1983) Mount St. Helens 1980 and Mount Pelee  
1902--Flow or surge? Geology 11: 571-574
- Walker GPL, McBroome LA (1984) Reply to comments on "Mount St.  
Helens 1980 and Mount Pelee 1902--Flow or surge?" Geology 12:  
693-695
- Walker GPL, Wilson CJN (1983) Lateral variations in the Taupo  
ignimbrite. J Volcanol Geotherm Res 18: 117-133
- Walker GPL, Wilson L, Howell ELG (1971) Explosive volcanic eruptions  
- I. The rate of fall of pyroclasts. Geophys J R Astron Soc 22:  
377-383
- Walker GPL, Self S., Froggatt PC (1981a) The ground layer of the  
Taupo ignimbrite: A striking example of sedimentation from a  
pyroclastic flow. J Volcanol Geotherm Res 10: 1-11
- Walker GPL, Wilson CJN, Froggatt PC (1981b) An ignimbrite veneer  
deposit: The trail-marker of a pyroclastic flow. J Volcanol  
Geotherm Res 9: 409-421
- Waters AC, Fisher RV (1971) Base surges and their deposits:  
Capelinhos and Taal volcanoes. J Geophys Res 76: 5596-5614

- Wilson CJN (1980) The role of fluidization in the emplacement of pyroclastic flows: An experimental approach. *J Volcanol Geotherm Res* 8: 231-249
- Wilson CJN (1984) The role of fluidization in the emplacement of pyroclastic flows 2: Experimental results and their interpretation. *J Volcanol Geotherm Res* 20: 55-84
- Wilson CJN (1985) The Taupo eruption, New Zealand II: The Taupo ignimbrite. *Phil Trans R Soc London Ser A* 314: 229-310
- Wilson CJN, Walker GPL (1982) Ignimbrite depositional facies: The anatomy of a pyroclastic flow. *J Geol Soc London* 139: 581-592
- Wilson CJN, Walker GPL (1985) The Taupo eruption, New Zealand I. General aspects. *Phil Trans R Soc London Ser A* 314: 199-228
- Wilson L (1976) Explosive volcanic eruptions - III. Plinian eruption columns. *Geophys J R Astron Soc* 45: 543-556
- Wilson L, Head JW (1981) Morphology and rheology of pyroclastic flows and their deposits, and guidelines for future observations. In: Lipman PW, Mullineaux DR (eds) *The 1980 eruptions of Mount St. Helens, Washington, USGS Prof Pap* 1250: 513-524
- Wilson L, Walker GPL (1987) Explosive volcanic eruptions - VI. Ejecta dispersal in plinian eruptions: The control of eruption conditions and atmospheric properties. *Geophys J R Astron Soc* 89: 657-679
- Wilson L, Sparks RSJ, Huang TC, Watkins ND (1978) The control of volcanic column heights by eruption energetics and dynamics. *J Geophys Res* 83: 1829-1836

- Wilson L, Sparks RSJ, Walker GPL (1980) Explosive volcanic eruptions  
- IV. The control of magma properties and conduit geometry on  
eruption column behavior. *Geophys J R Astron Soc* 63: 117-148
- Wilson L, Pinkerton H, MacDonald R (1987) Physical processes in  
volcanic eruptions. *Ann Rev Earth Planet Sci* 15: 73-95
- Wohletz KH (1983) Mechanisms of hydrovolcanic pyroclast formation:  
Grain-size, scanning electron microscopy, and experimental  
studies. *J Volcanol Geotherm Res* 17: 31-63
- Wohletz KH (1986) Explosive magma-water interactions:  
Thermodynamics, explosion mechanisms, and field studies. *Bull  
Volcanol* 48: 245-264
- Wohletz KH, Sheridan MF (1979) A model of pyroclastic surge. *Geol  
Soc Am Sp Pap* 180: 177-194
- Wohletz KH, McGetchin TR, Sandford MT II, Jones EM (1984)  
Hydrodynamic aspects of caldera-forming eruptions: Numerical  
models. *J Geophys Res* 89: 8269-8286
- Wright JV (1981) The Rio Caliente ignimbrite: Analysis of a  
compound intraplinian ignimbrite from a major late Quaternary  
Mexican eruption, *Bull Volcanol* 44: 189-212
- Wright JV, Walker GPL (1977) The ignimbrite source problem:  
Significance of a co-ignimbrite lag-fall deposit. *Geology* 5:  
729-732
- Wright JV, Walker GPL (1981) Eruption, transport and deposition of  
ignimbrite: A case study from Mexico. *J Volcanol Geotherm Res*  
9: 111-131

- Wright JV, Smith AL, Self S (1980) A working terminology of pyroclastic deposits. *J Volcanol Geotherm Res* 8: 315-336
- Yih C-S (1980) Stratified flows. Academic Press New York, pp 103-141
- Young RA (1966) Cenozoic Geology Along the Edge of the Colorado Plateau in Northwestern Arizona. Unpub PhD dissertation, Washington Univ
- Young RA, Brennan WJ (1974) Peach Springs Tuff: Its bearing on structural evolution of the Colorado Plateau in northwestern Arizona. *Geol Soc Am Bull* 85: 83-90

Printed in the United States of America  
Available from  
National Technical Information Service  
US Department of Commerce  
5285 Port Royal Road  
Springfield, VA 22161

Microfiche (A01)

Page Range	NTIS Price Code						
001-025	A02	151-175	A08	301-325	A14	451-475	A20
026-050	A03	176-200	A09	326-350	A15	476-500	A21
051-075	A04	201-225	A10	351-375	A16	501-525	A22
076-100	A05	226-250	A11	376-400	A17	526-550	A23
101-125	A06	251-275	A12	401-425	A18	551-575	A24
126-150	A07	276-300	A13	426-450	A19	576-600	A25
						601-up*	A99

\*Contact NTIS for a price quote.